

**VYSOKÉ UČENÍ TECHNICKÉ V BRNĚ
FAKULTA CHEMICKÁ**

**Podklady k habilitační práci v oboru
Fyzikální chemie**

Ing. et Bc. Renata Štysová Rychtáriková, Ph.D.

Brno 2024

Obsah

1 Životopis uchazečky	1
2 Vyjádření vztahu k VUT a důvodů pro předložení návrhu ke jmenování na VUT	5
3 Doklady o dosaženém vysokoškolském vzdělání a získaných příslušných titulech	6
4 Pedagogická praxe	10
5 Odborné a vědecké stáže	14
6 Seznam publikovaných prací a realizovaných inženýrských děl	15
7 Tabulka dosažených kvantifikovaných hodnotících oborových kritérií	25
8 Vyjádření uchazečky k bodovému hodnocení	30
9 Pět nejvýznamnějších publikací ..	32
10 Anotace tří témat pro veřejnou pedagogickou přednášku	104

1 Životopis uchazečky

Jméno:	Ing. et Bc. Renata Štysová Rychtáriková, Ph.D.
Narozena:	3. března 1983 v Jihlavě
Trvalé bydliště:	Vilová čtvrť 197, 373 33 Nové Hrady
Národnost:	česká
Rodinný stav:	vdaná, jeden syn (nar. 2017)

Vzdělání a kvalifikace

- 2011 **Ph.D. (Biotechnologie)** – společná akreditace ÚCHP AV ČR a FPBT VŠCHT Praha
- 2006 **Bc. (Učitelství odborných předmětů)** – VŠCHT Praha
- 2006 **Ing. (Konzervace potravin a technologie masa)** – FPBT VŠCHT Praha
- 2001 **maturita (všeobecné sedmileté studium)** – Gymnázium Otokara Březiny v Telči

Zaměstnání

- od 1/2023 **Ministerstvo průmyslu a obchodu ČR, Praha** – externí hodnotitel projektů OP TAK a OP PIK – DPČ
- od 12/2012 **Ústav komplexních systémů FROV JU, Nové Hrady** – postupně postdoktorand, vědecký pracovník a akademický pracovník v Laboratoři experimentálních komplexních systémů
- 8/2011–1/2013 **FARMEKO, VOŠZ a SOŠ, s.r.o., Jihlava** – učitel (Klinická biochemie, Mikrobiologie, toxikologie a hygiena, Biochemie a biotechnologie, Farmakognosie)
- 7/2011 **Safibra, s.r.o., Říčany u Prahy** – výzkumný a školicí pracovník přípravy optických biosenzorů
- 9/2006–6/2011 **Ústav chemických procesů AV ČR, v. v. i., Praha** – vědecký pracovník–doktorand v Laboratoři imobilizovaných biomateriálů a optických senzorů

Cestovní granty na konference

1. Československá mikroskopická společnost – EMC 2016, Lyon, Francie (2016)
2. ESF-EMBO EMBO – ESF-EMBO Symposium, Sant Feliu de Guixols, Španělsko (2007)

■ Výzkumné projekty

■ Hlavní řešitel

1. **Návrh a ověření metody pro analýzu částic v provozních kapalinách pomocí mikroskopu s průtokovou celou**, MPO Inovační vouchery VI, 12/2022–7/2022, 587 tis. Kč, pro ASTOS Machinery a.s., Aš.
2. **Testování principů mikroskopického sledování kvality navíjení mikrospirály wolframového vlákna pro žárovky**, MPO Inovační vouchery VI, 12/2022–7/2022, 604 tis. Kč, pro dataPartner s.r.o., České Budějovice.
3. **Testování principů mikroskopického sledování kvality navíjení mikrospirály wolframového vlákna pro žárovky**, MPO Inovační vouchery, 12/2022–7/2023, 46 tis. Kč, pro dataPartner s.r.o., České Budějovice.
4. **Výzkum v oblasti buněčné imunity, otevřený účet FROV JČU financovaný ze soukromých zdrojů**, 27 tis. Kč
5. **Konsolidace software jednoduchého mikroskopu velmi vysokého rozlišení NanoTruth**, TAČR Gamma, TG03010027, 4/2018–12/2019, 218 tis. Kč.

■ Spoluřešitel-zodpovědný řešitel za FROV JU

1. **Lamelový sedimentační systém filtrace nové generace**, TAČR Trend PP1 Technologičtí lídři, 1/2024–6/2026, rozpočet FROV JU 6 328 tis. Kč (90% dotace) – spolupráce s firmami ASTOS Machinery a.s. a MACHINERY DESIGN s.r.o. (Ing. Martin Valíček).
2. **Vývoj procesu hodnocení kadaverózních rohovkových lamel pomocí inovace mikroskopických systémů pro celulární analýzu**, MPO Aplikace, 9/2021–5/2023, rozpočet FROV JU 3 218 tis. Kč (85% dotace) – spolupráce s firmami PrimeCell Bioscience a Národním centrem tkání a buněk (MUDr. Šárka Sekorová, Mgr. Martina Tlamková)

■ Člen řešitelského týmu

1. **Velká výzkumná infrastruktura CENAKVA – LM2023038**, MŠMT ČR, 1/2023–12/2026.
2. **Velká výzkumná infrastruktura CENAKVA – LM2018099**, MŠMT ČR, 1/2018–12/2022.
3. **Image HeadStart** – Interreg V-A Rakousko-ČR – ERDF ATCZ133, 1/2020–12/2022
4. **Individualizované pozorování chování pro bezpečnostní aplikace** – PoC 02-22 TAČR GAMA TG 03010027, 1/2017–12/2019.

5. **Jihočeské výzkumné centrum akvakultury a biodiverzity hydrocenóz** – LM2018099, 1/2019–12/2020.
6. **Kompetenzzentrum MechanoBiologie** – Interreg V-A Rakousko-ČR – ERDF ATCZ133, 3/2017–8/2020
7. **Postdok JU** – MŠMT ČR, 12/2012–6/2015
8. **Jihočeské výzkumné centrum akvakultury a biodiverzity hydrocenóz (CENAKVA)** – MŠMT OP VaVpI CZ.1.05/2.1.00/01.0024, 2010–2013.
9. **Jihočeské výzkumné centrum akvakultury a biodiverzity hydrocenóz – udržitelnost (CENAKVA II)** – MŠMT LO1205 pod programem NPU I.
10. **Rozvoj CENAKVA** – MŠMT CZ.1.05/2.1.00/19.0380.
11. **Distribuované uložení dat velkého objemu založené na znalostním modelu pro biomedicínu, bezpečnost potravin a další biologické aplikace** – TA ČR TA0101214, 2011–2015.
12. **Singletový kyslík produkovaný senzitivními na pevných anorganických nosičích: Fotodesinfekční materiály a sondy** – GA ČR 203/06/1244, 2006–2008.
13. **Optické chemické senzory (OPTISENS)** – mezinárodní spolupráce s Univerzitou v Mariboru, Slovinsko, MŠMT KONTAKT MEB 090817, 3/2008–2009.
14. **Interakce organicko-anorganických nosičů s imobilizovaným biologickým materiálem** – MŠMT, COST OC121, 3/2006–3/2009.
15. **Struktura a syntetické aplikace komplexů přechodných kovů** – spolupráce s ÚFCH JH AV ČR, UK a VŠCHT, MŠMT LC06070, 3/2006–2010.
16. **Monitorování a remediací znečištění životního prostředí pokročilými organicko-anorganickými materiály (MOREPIM)** – MŠMT KONTAKT ME 892, 5/2007–2011.
17. **Celobuněčný optický senzor (WOCOS)** – MŠMT KONTAKT ME 893, 5/2007–2011.

■ Další certifikáty a školení

- 9/2022 Osvědčení „Manažer kvality zkušební, kalibrační a zdravotnické laboratoře – základní znalosti a dovednosti“ v rozsahu norem ČSN EN ISO/IEC 17025:2018, ČSN EN ISO 15189:2013 a ČSN EN ISO 19011:2019 (č. 1257/2022)
- 11/2021 Osvědčení vybraného posuzovatele pro senzorickou analýzu v rozsahu požadavků normy ČSN ISO 8586:2015 (ev. č. 161121-4, platné 5 let)
- 9/2015 Biological Samples for Electron Microscopy, České Budějovice, Ing. J. Nebesářová
- 10/2013 Microscopy and Image Analysis workshop, Vodňany, prof. Ch. Rouvière a prof. C. Matthews

6/2009 COST865 2009 Summer School, Early Stage Researcher Training on
Bioencapsulation, Anzère, Švýcarsko, prof. D. Poncelet
5/2008 Immunochemistry 2008, VŠCHT Praha, prof. J. Dausant

2 Vyjádření vztahu k VUT a důvodů pro předložení návrhu ke jmenování na VUT

S děkanem FCH VUT prof. Michalem Veselým jsem spolupracovala na vydání tří jazykových mutací skript pro výuku předmětu Chemie II na FROV JU:

1. Rychtáriková R., Štys D.: Moderní laboratorní cvičení z organické fyzikální chemie a analýzy. VUT Brno (2023), 50 stran, ISBN 978-80-214-6146-8, elektronicky.
2. Rychtáriková R., Štys D.: Modern laboratory practices in physical organic chemistry and analysis. VUT Brno (2023), 50 stran, ISBN 978-80-214-6145-1, elektronicky.
3. Rychtáriková R., Štys D.: Moderne Laborübungen in organischer physikalischer Chemie und Analytik. VUT Brno (2023), 52 stran, ISBN 978-80-214-6144-4, elektronicky.

Recenzent: doc. Ing. Josef Trögl, Ph.D.

Korektor němčiny: Prof. Gottfried Köhler

Učebnice je základem inovace předmětu Chemie II a slouží pro výuku relevantních laboratorních cvičení (převážně organická chemie a spektroskopie malých organických molekul) v 1. ročníku denního a kombinovaného bakalářského studia oborů Ochrana vod a Rybářství na FROV JU. Je založena na dvou originálních komplexních laboratorních cvičeních ze spektroskopie organických látek sestavených autory. Laboratorním cvičením předchází teorie absorpčních molekulových spekter, elektrochemie, pufrů a interakce organické látky s prostředím. V laboratorních cvičeních se využívá k přípravě pufrů systém měřicích sond AquaSheriff komunikující s uživatelem přes webovou aplikaci. Měřicí systém byl vyvinut na ÚKS FROV Nové Hradky. Na vývoji systému AquaSheriff jsem se podílela zejména jako tester a sepsala jsem k němu návody. Můj autorský podíl je 75 %.

Vzhledem ke skutečnosti, že FROV JU, na které odborně a pedagogicky působím, nemá akreditaci habilitačního řízení v oboru Fyzikální chemie, do něhož předložená habilitační práce spadá, obrátila jsem se na FCH VUT.

■ **3 Doklady o dosaženém vysokoškolském vzdělání a získaných příslušných titulech**



ČESKÁ REPUBLIKA

VYSOKÁ ŠKOLA
CHEMICKO-TECHNOLOGICKÁ V PRAZE

stvrzuje, že

ING. RENATA RYCHTÁRIKOVÁ

narozena 3. března 1983 v Jihlavě

získala vysokoškolské vzdělání studiem v doktorském studijním programu P 2836

BIOCHEMIE A BIOTECHNOLOGIE

ve studijním oboru 2810V001

BIOTECHNOLOGIE

na Fakultě potravinářské a biochemické technologie a obhájila disertační práci s názvem

Antimikrobiální účinky imobilizovaných porfyrinů

Podle § 47 odst. 5 zákona č. 111/1998 Sb., o vysokých školách a o změně a doplnění dalších zákonů se jí uděluje

akademický titul DOKTOR, ve zkratce Ph. D., uváděné za jménem

ČÍSLO DIPLOMU 1151

V Praze 16. listopadu 2011

rektor

děkan fakulty

ČESKÁ REPUBLIKA

VYSOKÁ ŠKOLA CHEMICKO - TECHNOLOGICKÁ V PRAZE

Číslo diplomu HJ 0001086

Číslo protokolu 5836

DIPLOM

Renata Rychtářiková

(Jméno a příjmení)

3. března 1983, Jihlava

(Datum a místo narození)

získal/získala vysokoškolské vzdělání studiem v magisterském studijním programu
chemie a technologie potravin

ve studijním oboru **konzervace potravin a technologie masa**

na Fakultě **potravinářské a biochemické technologie**

kód M 2901

kód (KKOV) 2901T008

Podle § 46 odst. 4 zákona č. 111/1998 Sb., o vysokých školách a o změně a doplnění dalších zákonů (zákon o vysokých školách),
se mu/jí uděluje

akademický titul **inženýr** ve zkratce „**Ing.**“ uváděné před jménem.

V Praze dne 5. června 2006



Prof. Ing. Vlastimil Růžička, CSc.

rektor



Doc. Ing. Karel Melzoch, CSc.

děkan

SEVT - 92 516 5

B.N.B. 482 2005

ČESKÁ REPUBLIKA

VYSOKÁ ŠKOLA CHEMICKO - TECHNOLOGICKÁ V PRAZE

Číslo diplomu HJ 0001493

Číslo protokolu 229

DIPLOM

Renata RYCHTÁRIKOVÁ

(Jméno a příjmení)

3. března 1983, Jihlava

(Datum a místo narození)

získal/získala vysokoškolské vzdělání studiem v bakalářském studijním programu **Specializace v pedagogice** kód **B7507**
ve studijním oboru..... kódu **(KKOV)** kódu **7504R100**

Učitelství odborných předmětů

na Vysoké škole chemicko-technologické v Praze.

Podle § 45 odst. 4 zákona č. 111/1998 Sb., o vysokých školách a o změně a doplnění dalších zákonů (zákon o vysokých školách),
se mu/ji uděluje

akademický titul **bakalář** ve zkratce „**Bc.**“ uváděné před jménem.

V Praze dne 5. září 2006



Prof. Ing. Vlastimil Ružička, CSc.

rektor

4 Pedagogická praxe

Předmět VŠ (typ studia)	Rozsah	Počet semestrů	Druh	Počet studentů
Fyzikální biologie (Ph.D., denní, PřF JU)	3-týdenní kurz v aj, 1 ze 2 cvičících, LS 2013-2018	3	C, pov.	10+9+9
Chemie II (Bc., denní, FROV JU)	2 h/týden, od LS 2017	7	C, pov.	22 + 14 + 17 + 18 + 24 + 12 + 22 + 22
Chemie II (Bc., kombinované, FROV JU)	1 h/týden, od LS 2017	7	C, L, pov.	5 + 4 + 5 + 4 + 2 + 4 + 3 + 9
Bioinformatika (Ph.D., denní + kombinované, čj a aj, FROV JU)	týdenní kurz, 1 ze 4 vyučujících, od LS 2021	3	P, C, L, vol.	7 + 4 + 1 + 0
Zpracování obrazu (Ph.D., denní + kombinované, FCHI VŠCHT, LS 2019)	3-denní kurz, 1 ze 3 přednášejících	1	P, C, vol.	2
Technické normy (Bc., denní, FROV JU)	2 h/týden, jediný vyučující, garant předmětu, od ZS 2021	3	P, C, pov.	9 + 6 + 1
Technické normy (Bc., kombinované FROV JU, garant předmětu)	2 h/týden, jediný vyučující, garant předmětu, od ZS 2022	3	P, C, pov.	1 + 0
Modelování přírodních systémů (Bc., denní + kombinované FROV JU)	2 h/týden, 1 ze 2 vyučujících, od LS 2022	1	C, vol.	10 + 0 + 0

P – přednáška, C – cvičení, L – laboratoře, pov. – povinné, vol. – volitelné, LS – letní semestr, ZS – zimní semestr

V letech 2013-2014, kdy působil prof. Dalibor Štys na MŠMT, vedla výzkumný tým.

■ Školitel a školitel specialista VŠKP

■ Dizertační práce na PŘF JU

1. Ganna Platonova: Contribution to information analysis in digital light microscopy, předpokládaná obhajoba 11/2024.
 - Spoluautorka 2 publikací s IF (Lonhus a kol., Sci. Rep. 2020; Platonova a kol., Photonics 2021)
 - Nyní zaměstnána v ÚJF AV ČR Řež
2. Ali Ghaznavi: Cell segmentation from wide-field light microscopy images using CNNs, obhájeno 26. 6. 2023.
 - Spoluautor 3 publikací s IF (Ghaznavi a kol., Symmetry 2024; Ghaznavi a kol., Comp. Biol. Med. 2022; Lonhus a kol., Eur. Phys. J.-Spec. Top. 2021)
 - Nyní postdok na Bundesanstalt für Materialforschung und -prüfung, Berlín, Německo
3. Kirill Lonhus: Investigating intrinsic behavioural parameters of autonomous objects based on motion, obhájeno 2. 2. 2022.
 - Spoluautor 5 publikací s IF (Lonhus a kol., Complex Intell. Syst. 2023; Platonova a kol., Photonics 2021; Lonhus a kol., Eur. Phys. J.-Spec. Top. 2021; Lonhus a kol., Sci. Rep. 2020; Lonhus a kol., Symmetry 2019), 1 recenzované publikace (Macková a kol., Vodní hospodářství 2022) a 7 aplikovaných výstupů
 - Nyní vědecký pracovník FROV JU
4. Anna Zhyrova: State trajectory approach to the interpretation of self-organization in the Belousov-Zhabotinsky reaction, obhájeno 24. 11. 2017.
 - Spoluautorka 1 publikace s IF (Štys a kol., Eur. Phys. J.-Spec. Top. 2019), 3 příspěvků v konferenčním sborníku na WOS a 1 příspěvku v recenzovaném konferenčním sborníku
 - Nyní zaměstnána v Robert Bosch, spol. s r. o., České Budějovice
5. Tomáš Náhlík: Microscopy – Point Spread Function, Focus, Resolution, obhájeno 15. 1. 2016
 - Spoluautor 1 publikace s IF (Rychtáriková a kol., Ultramicroscopy 2017), 3 příspěvků v konferenčním sborníku na WOS, 3 příspěvků v recenzovaném konferenčním sborníku, 1 monografie a 4 softwarů
 - Nyní odborný asistent VŠTE České Budějovice

■ Bakalářské práce na Università degli Studi di Padova

1. Alisa Plaksina: Caffeine-induced changes in a shoal behaviour of Tiger Barb (*Puntigrus tetrazona*), obhájeno 13. 10. 2021.

■ Bakalářské práce na FROV JU

1. Jan Košek: Studium dynamiky živých lidských buněk v odezvě na běžné kontaminanty vod s cílem vývoje citlivého specifického analytického postupu, obhájeno 6. 6. 2023.
2. Eliška Pejcharová: Změny hejnového chování akvariálních ryb v přítomnosti kontaminantu, obhájeno 14. 6. 2022. Presentováno na 2 konferencích.
3. Barbora Macková: Změny hejnové hierarchie ryb jako citlivý indikátor bioaktivních látek, obhájeno 14. 6. 2021. Spoluautorka Macková a kol., Vodní hospodářství 2022.
4. Miroslav Slivoně: Vliv běžných pesticidů na lidské buňky, obhájeno 1. 7. 2020.

■ Mezinárodní letní školy FROV JU Nové Hrady

- 1- až 2-měsíční výzkumné projekty z optické mikroskopie a zpracování digitálního obrazu

1. Alisa Plaksina (Università degli Studi di Padova, 2021)
2. Olesya Nikitina (V. N. Karazin Kharkiv National University, Ukrajina, 2016)
3. Claudia del Carmen Diaz Armás (Tecnico de Monterrey, Mexiko, 2016)
4. Raul Suarez Rodriguez (Universidad de Las Palmas de Gran Canaria, Španělsko, 2015)
5. Kateryna Akulich (V. N. Karazin Kharkiv National University, Ukrajina, 2015)
6. Marco Gómez (Tecnico de Monterrey, Mexiko, 2014)
7. Kevin Shi (University of Princeton, USA, 2013) – spoluautor 1 publikace s IF (Rychtáriková a kol., Ultramicroscopy 2017)
8. Adam Charvát (Gymnázium J. V. Jirsíka, České Budějovice, 2014)
9. Lucie Draslarová (Česko-anglické gymnázium, České Budějovice, 2014)
10. Markéta Novotná (Česko-anglické gymnázium, České Budějovice, 2014) – spoluautorka 1 recenzované publikace (Rychtáriková a kol., PURPLSOC 2014)
11. Magdalena Koutová (Gymnázium Česká a Olympijských nadějí, České Budějovice, 2013)
12. Marie Hyblová (Gymnázium Česká a Olympijských nadějí, České Budějovice, 2013)

■ Kurzy a školení

- Superresolution microscopy from brightfield images, Letní školy FROV JU Nové Hrady – 45-min přednáška (aj), 13. 7. 2016
- Konfokální a superrozlišovací mikroskopie, Jihočeský vědecko-technický park, České Budějovice – 40-min přednáška, 23. 2. 2016

- COST Microscopy and Image Analysis Training Course, FROV JU Vodňany – 120-min přednáška (aj), 16.–20. 3. 2015

■ Výuka na VOŠ

8/2011–1/2014 – **FARMEKO, VOŠZ a SOŠ, Jihlava**

- Farmakognozie (0/2/0) – přednášky pro denní i kombinované studium
Diplomovaný farmaceutický asistent

■ Výuka na SŠ

8/2011–1/2014 – **FARMEKO, VOŠZ a SOŠ, Jihlava**

- Klinická biochemie (0/1/3/4), Cvičení z klinické biochemie (0/0/3/4) – teoretická a praktická výuka pro obor Laboratorní asistent
- Mikrobiologie, hygiena a toxikologie (0/2/0/0)
- Biochemie a biotechnologie (0/0/3/0) – teoretická výuka pro obor Ekologie a životní prostředí
- vedení školního kola Chemické olympiády
- příprava elektronických studijních materiálů

1–2/2006 – **Střední průmyslová škola masné technologie, Navrátilova 15, Praha** – pedagogická praxe

- Obecná a anorganické chemie – teoretická výuka pro obor Přírodovědné lyceum
- Mikrobiologie a Technologie masa – teoretická výuka pro obor Technologie zpracování masa a masných výrobků

5 Odborné a vědecké stáže

- 9/2019 **Ankara University, Faculty of Veterinary Medicine, Department of Toxicology and Pharmacology, Ankara, Turecko** (doc. Begum Yurdakok Dikmen)
Téma: Teaching Activities Focused on the Veterinary Pharmacology and Toxicology Field (týdenní stáž Erasmus+)
- 10–11/2016 **Donau University of Krems, Faculty of Health and Medicine, Krems an der Donau, Rakousko** (prof. M. B. Fischer)
Téma: 3D Live Cell Imaging - a Technical Solution (měsíční stáž Aktion AT-CZ + týdenní stáž Erasmus+)
- 3–6, 9–12/2014 **European Molecular Biology Laboratory, Advanced Light Microscopy Facility, Heidelberg, Německo** (Dr. Rainer Pepperkok a Dr. Yury Belyaev)
Téma: 3D Modelling of diffracting organelles inside the living cells (6-měsíční stáž Postdok JU)
- 7–8/2012 **Univerzita Karlova v Praze, Matematicko-fyzikální fakulta, Česká republika** (RNDr. P. Gabriel)
Téma: Vývoj optického senzoru pro měření pH v kvasném průmyslu (2-měsíční stáž)
- 11–12/2008, 8/2009 **University of Maribor, Faculty of Mechanical Engineering, Center of Sensor Technology, Maribor, Slovinsko** (prof. A. Lobnik)
Téma: Optické chemické senzory – OPTISENS – Příprava senzorů pro měření pH, paraoxonu a biogenních aminů v potravinách a životním prostředí (MŠMT KONTAKT)
- 10/2008 **Swedish University of Agriculture Sciences, Department of Chemistry, Uppsala, Švédsko** (prof. V. Kessler)
Téma: „Biokompatibilní titaničité hydrosoly a hydrogely s navázanými porfyriny“ – Příprava materiálů pro dezinfekci ran a léčbu rakoviny (2-týdenní COST865 STSM)
- 7/2005 **Coca-Cola HBC Česká republika, Praha** – Asistent kontroly kvality – Kontrola kvality obalových materiálů (3-týdenní stáž)

6 Seznam publikovaných prací a realizovaných inženýrských děl

Článek v časopise WoS a Scopus

H-index 6, IF/SJR udáváno pro rok publikace, * korespondující autor

1. Ghaznavi A., **Rychtáriková R.**, Císař P., Ziaei M.M., Štys D.: Symmetry Breaking in the U-Net: Hybrid Deep-Learning Multi-Class Segmentation of HeLa Cells in Reflected Light Microscopy Images. *Symmetry* 16, 227 (2024). Q2; IF 2,7, cit. 1
 1. Ning W et al: Constr Build Mater 434:136770 (2024).
2. Lonhus K., Štys D., **Rychtáriková R.***: Quantification of Collective Behaviour via Causality Analysis. *Complex Intell. Syst.* 9, 5807–5816 (2023). Q1; IF 5
3. Ghaznavi A., **Rychtáriková R.***, Saberioon M., Štys D.: Cell Segmentation from Telecentric Bright-field Transmitted Light Microscopy Images Using a Residual Attention U-Net: A Case Study on HeLa Line. *Comp. Biol. Med.* 147, 105805 (2022). Q1; IF 6,7, cit. 14
 1. Carrafini F et al: Lect Notes Comp Sci 14976:104-117 (2024).
 2. Hattori S et al: Appl Sci 14(17):7958 (2024).
 3. Wang Q et al: Electronics 13(17):3430 (2024).
 4. Wu H et al: Opt Laser Technol 179:111311 (2024).
 5. Asha SB et al: Expert Syst Appl 253:124309 (2024).
 6. Gabdullin MT et al: Biotechnol Bioprocess Eng doi:10.1007/s12257-024-00130-5 (2024).
 7. Dugue-Vazquez et al: Heliyon 10(5):26520 (2024).
 8. Ghaznavi A et al: Appl Comput Geosci 100150 (2024).
 9. Wu H et al: Int J Mol Sci 24(22):16028 (2023).
 10. Yidong W et al: Laser Optoelectron Prog 60(14): 1410015 (2023).
 11. Khani M et al: Phys Commun 61(5):102188 (2023).
 12. Zang L et al: Sci Rep 12779 (2023).
 13. Alabdaly AA et al: J Intell Fuzzy Syst 44(3):4759-4777 (2023).
 14. Mohammed AA et al: Proceedings of the 14th Conference on ACM Multimedia Systems, 451-457 (2023).
4. Platonova G., Štys D., Souček P., Lonhus K., Valenta J., **Rychtáriková R.***: Spectroscopic Approach to Correction and Visualization of Bright-Field Light Transmission Microscopy Biological Data. *Photonics* 8(8), 333 (2021). Q2; IF 2,5, cit. 2
 1. Bian Y et al: Cells 11:3670 (2022).
 2. Moskovsky MN et al: Photochem. Photobiol. 99(1):29-34 (2022).
5. Lonhus K., **Rychtáriková R.**, Ghaznavi A., Štys D.: Estimation of Rheological Parameters for Unstained Living Cells. *Eur. Phys. J.-Spec. Top.* 230(4), 1105–1112 (2021). Q2; IF 2,9; **zvaný**

6. Lonhus K., **Rychtáriková R.**, Platonova G., Štys D.: Quasi-Spectral Characterization of Intracellular Regions in Bright-Field Light Microscopy Images. *Sci. Rep.* 10, 18346 (2020). Q1; IF 4,4.
Obsahem tiskové zprávy z 18. 11. 2020 s cca 30 mediálními výstupy včetně ČT.

7. Urban J., **Rychtáriková R.**, Macháček P., Štys D., Urbanová P., Císař P.: Optimization of Computational Burden of the Point Information Gain. *Acta Polytech.* 59(6), 593–600 (2019). Q3; SJR 0,213

8. Lonhus K., Štys D., Saberioon M., **Rychtáriková R.**: Segmentation of Laterally Symmetric Objects: Application to Images of Collective Animal Behavior. *Symmetry* 11(7), 866 (2019). Q2; IF 2,6; cit. 1

1. Zhang J, Liu C: *Automatika* 61(1):150-157 (2020).

Speciální propagace časopisem Symmetry.

9. Štys D., **Rychtáriková R.***, Zhyrova A., Štys K.M., Jizba P.: Noisy Hodgepodge Machine and the Observed Mesoscopic Behaviour in the Non-Stirred Belousov-Zhabotinsky Reaction: Optimal Noise and Hidden Noise in the Hodgepodge Machine. *Eur. Phys. J.-Spec. Top.* 227, 2361–2374 (2019). Q2; IF 1,7; **zvaný**

10. **Rychtáriková R.***, Urban J., Štys D.: Žampa's Systems Theory: a Comprehensive Theory of Measurement in Dynamic Systems. *Acta Polytech.* 58(2), 128–143 (2018). Q3; SJR 0,2; cit. 1

1. Khouzani MHR, Malacaria P: *Entropy* 20(9):675 (2018).

11. **Rychtáriková R.***, Korbelt J., Macháček P., Štys D.: Point Divergence Gain and Multidimensional Data Sequence Analysis. *Entropy* 20(2), 106 (2018). Q2; IF 2,4; cit. 3

1. Lo W-C et al: *Appl Sci* 12:6602 (2022).
2. Dong C et al: *J Phys Conf Ser* 2010(1):012067 (2021).
3. Zhuo R, Bai Z: *Lect Notes Electr Eng* 675:657 (2020).

12. **Rychtáriková R.***, Štys D.: Observation of Dynamics Inside an Unlabeled Live Cell Using a Bright-Field Photon Microscopy: Evaluation of Organelles' Trajectories. IWBBIO 2017, Proceedings, Part II, *LNBI* 10209, Ortuno and Rojas (eds.), Springer, Switzerland, 2017, pp. 700–711. Q2; SJR 0,3; cit. 1

1. Suzuki G et al: *npj Syst. Biol. Appl.* 7:31 (2021).

13. **Rychtáriková R.***, Steiner G., Fischer M. B., Štys D.: Information Limits of Optical Microscopy: Application to Fluorescently Labelled Tissue Section. IWBBIO 2017, Proceedings, Part I, *LNBI* 10208, Ortuno and Rojas (eds.), Springer, Switzerland, 2017, pp. 485–496. Q2; SJR 0,3

14. Zhyrova A., **Rychtáriková R.**, Štys D.: Recognition of Stages in the Belousov-Zhabotinsky Reaction Using Information Entropy. IWBBIO 2017, Proceedings, Part I, *LNBI* 10208, Ortuno and Rojas (eds.), Springer, Switzerland, 2017, pp. 335–346. Q2; SJR 0,3
15. **Rychtáriková R.***, Náhlík T., Shi K., Malakhova D., Macháček P., Smaha R., Urban J., Štys D.: Super-Resolved 3-D Imaging of Live Cells' Organelles from Bright-Field Photon Transmission Micrographs. *Ultramicroscopy* 179, 1–14 (2017). Q1; IF 2,9; cit. 1
1. Urbanova P, et al: Lect Notes Bioinf. 11465:142-153 (2019).
- Rank 1 v oboru Mikroskopie, vybráno vydavatelstvem Elsevier mezi cca 30 fyzikálních článků roku 2017 určených k další propagaci. Obsahem tiskové zprávy z 24. září 2017 s cca 15 mediálními výstupy včetně ČT.**
16. **Rychtáriková R.***, Korbel J., Macháček P., Císař P., Urban J., Štys D.: Point Information Gain and Multidimensional Data Analysis. *Entropy* 18(10), 372 (2016). Q2; IF 1,8; cit. 8
1. Ragragui H et al: Groundw Sustain Dev 26:101281 (2024).
 2. Grandhi A, Singh SK: 2023 7th Int Conf Trends Electron Inform (ICOEI) 1046-1054 (2023)
 3. Mohapatra S, Neha C: Eng Sci 21, 787 (2023).
 4. Xin G et al: Entropy 25(1):48 (2023).
 5. Zhang W et al: Proc Int Joint Conf AAMAS, 1629-1637 (2020).
 6. Cui L, Lin Ch: Entropy 22(7):778 (2020).
 7. Fang Y et al: Appl Intel 50(12):4281-4295 (2020).
 8. Wang C et al: Entropy 19(2):65 (2017).
17. Štys D., Náhlík T., Macháček P., **Rychtáriková R.**, Saberioon M.: Least Information Loss (LIL) conversion of digital images and lessons learned for scientific image inspection. IWBBIO 2016, *LNBI* 9656, Ortuno and Rojas (eds.), Springer, Switzerland, 2016, pp. 527–536. Q2; SJR 0,252
18. Císař P., Náhlík T., **Rychtáriková R.**, Macháček P.: Visual Exploration of Principles of Microscopic Image Intensities Formation using Image Explorer Software. IWBBIO 2016, *LNBI* 9656, Ortuno and Rojas (eds.), Springer, Switzerland, 2016, pp. 537–544. Q2; SJR 0,3; cit. 1
1. Náhlík T: APLIMAT 2020 Proceedings 824-833 (2020).
19. **Rychtáriková R.***: Clustering of Multi-Image Sets Using Rényi Information Entropy. IWBBIO 2016, *LNBI* 9656, Ortuno and Rojas (eds.), Springer, Switzerland, 2016, pp. 517–526. Q2; SJR 0,3
20. Štys D., Náhlík T., Zhyrova A., **Rychtáriková R.**, Papáček Š., Císař P.: Model of the Belousov-Zhabotinsky Reaction. HPCSE 2015, *LNCS* 9611, Kozubek, Blaheta, Šístek, Rozložník, Čermák (Eds.), Springer, Switzerland, 2016, pp. 171–185. Q2; SJR 0,3; cit. 2
1. Tsompanas M-A et al: Biosystems 206:104447 (2021).

2. Tsompanas M-A et al: *Nonlin Dyn* 104:4103 (2021).
21. Štys D., Urban J., **Rychtáriková R.**, Zhyrova A., Císař P.: Measurement in Biological Systems from the Self-Organisation Point of View. IWBBIO 2015, Part II, *LNCS* 9044, Ortuno and Rojas (eds.), Springer, Switzerland, 2015, pp. 431–443. Q2; SJR 0,4
22. Bárta A., Císař P., Soloviov D., Souček P., Štys D., Papáček Š., Pautsina A., **Rychtáriková R.**, Urban J.: BioWes – from Design of Experiment, through Protocol to Repository, Control, Standardization and Back-Tracking. IWBBIO 2015, Part II, *LNCS* 9044, Ortuno and Rojas (eds.), Springer, Switzerland, 2015, pp. 426–430. Q2; SJR 0,4
23. Malakhova D., Stys D., **Rychtarikova R.**: Adjustment of Dynamic High Resolution Images of Living Cells by Combination of an Optical Microscopy in Transmitting Light, Atomic Force Microscopy and Image Information Analysis. *Chem. Listy* 107(SI), Suppl. 3, S402–S404 (2013). Q4; IF 0,2
24. **Rychtarikova R.***, Seisenbaeva G. A., Kuncova G., Kessler V. G.: Biocompatible Titania Hydrogels with Chemically Triggered Release of a Photosensitive Dye. *J. Sol-Gel Sci. Technol.* 62(3), 370–377 (2012). Q1; IF 1,7
25. **Rychtarikova R.***, Sabata S., Hetflejš J., Kuncova G.: Photodynamic Efficiency of Porphyrins Encapsulated into Polysilsesquioxanes. *Chem. Pap.* 66(4), 269–277 (2012). Q3; IF 0,9; cit. 7
1. Elian C et al: *Adv Funct Mater* doi:10.1002/adfm.202407228 (2024).
 2. Lesar A et al: *Int J Mol Sci* 21(15):5367 (2020).
 3. Zhang W-Y et al: *Chinese J Inorg Chem* 34(12):2161-2171 (2018).
 4. Ion RM et al: *React Kinet Mech Cat* 118(1):337-348 (2016).
 5. Alves E et al: *J Photochem Photobiol C-Photochem Rev* 22:34-57 (2015).
 6. Smolinska G et al: *Int J Environ Sci Technol* 12(1):61-72 (2015).
 7. Deda DK et al: *J Biomed Nanotechnol* 9(8):1307-1317 (2013).
26. **Rychtarikova R.***, Sabata S., Hetflejš J., Kuncova G.: Composites with Photosensitive 5,10,15,20-Tetrakis(*N*-methylpyridinium-4-yl)porphyrin Entrapped into Silica Gels. *J. Sol-Gel Sci. Technol.* 61(1), 119–125 (2012). Q1; IF 1,7; cit. 11
1. Elian C et al: *Adv Funct Mater* doi:10.1002/adfm.202407228 (2024).
 2. Rozga-Wijas K et al: *Cellulose* 30(1):1-20 (2023).
 3. Mesquita MQ et al: *Handbook of Porphyrin Science* 46:201-277 (2022).
 4. Zhao L et al: *Chemosphere* 230:124552 (2020).
 5. Li S et al: *Gaofenzi Cailiao Kexue Yu Gongcheng/Polymer Mater Sci Eng* 33(11):145-151 (2017).
 6. Gonzales-Delgado JA et al: *Int J Pharm* 510(1):221-231 (2016).
 7. Gonzales-Delgado JA et al: *J Med Chem* 59(10):4428-4442 (2016).
 8. Spagnol C et al: *J Photochem Photobiol B-Biol* 150 SI:11-30 (2015).
 9. Alves E et al: *J Photochem Photobiol C-Photochem Rev* 22:34-57 (2015).
 10. Zhao L et al: *J Hazard Mater* 301:223-241 (2016).
 11. Zucca P et al: *J Mol Catal A-Chem* 338 SI:2-34 (2014).

27. **Rychtarikova R.***, Kuncová G.: Metoda vyhodnocování antimikrobiální aktivity počítačovým prahováním barev. *Chem. Listy* 105(6), 493–498 (2011). Q4; IF 0,5; cit. 1
 1. Zigo F et al: Agriculture 10(6):245 (2020).
28. **Rychtarikova R.***, Kuncová G.: Imobilizované fotosenzitizátory singletového kyslíku a jejich účinek na mikroorganismy. *Chem. Listy* 103(10), 800–813 (2009). Q3; IF 0,7; cit. 4
 1. Rana P et al: Coord Chem Rev 470(1):214698 (2022)
 2. Sankhagowit S et al: Biochim Biophys Acta-Biomem 1838(10):2615-2624 (2014).
 3. Pessoni L et al: Langmuir 29(32): 10264-10271 (2013).
 4. Lacombe S, Pigot T: Photochemistry 38:307-329 (2011).
29. Šabata S., Hetflejš J., **Rychtáriková R.**, Kuncová G., Lang K., Kubát P.: Immobilization of Porphyrins in Poly(hydroxymethyl-siloxane). *Chem. Pap.* 63(4), 438–444 (2009). Q3; IF 0,8; cit. 1
 1. Piwovar K et al: Photosensitizers: Types, Uses and Selected Research 149-198 (2016).

■ Příspěvek ve sborníku mezinárodní vědecké konference

1. Štys D., Lonhus K., Karpov M., **Rychtáriková R.**: Visible Truth – digitální světelné mikroskopy (nejen) pro kontrolu kvality. CAE Forum 2023, Praha, Česká republika, 14.–15. září 2023.
2. **Rychtáriková R.***, Malečková D., Urban J., Bárta A., Novotná M., Zhyrova A., Náhlík T., Štys D.: Study of Human Perception with the Usage of Information Entropy Analysis of Patterns, in PURPLSOC: Pursuit of Pattern Language for Societal Challenges/PURPLSOC The Workshop 2014 1), Baumgartner and Sickinger (eds.), pp. 366–384, ISBN 978-3-7375-5458-9, epubli GmbH (Verlag), 2015, Austria.
3. Zhyrova A., **Rychtáriková R.**, Náhlík T., Štys D.: The Path of Aging: Self-Organization in Nature and 15 Properties, in PURPLSOC: Pursuit of Pattern Language for Societal Challenges/PURPLSOC The Workshop 2014 1), Baumgartner and Sickinger (Eds.), pp. 385–410, ISBN 978-3-7375-5458-9, epubli GmbH (Verlag), 2015, Austria.
4. **Rychtáriková R.***, Náhlík T., Smaha R., Urban J., Štys D. Jr., Císař P., Štys D.: Multifractality in Imaging: Application of Information Entropy for Observation of Inner Dynamics Inside of an Unlabeled Living Cell in Bright-Field Microscopy. In ISCS14, Sanayei et al. (eds.), Springer, Switzerland, 2015, pp. 261–267.

■ Monografie

1. **Rychtáriková R.**, Náhlík T.: System information approach to digital light microscopy. FROV JU České Budějovice (2023), ISBN 978-80-7514-185-9.

■ Článek v časopise uvedeném v národním seznamu recenzovaných časopisů

1. Malečková D., **Rychtáriková R.**, Urban J.: Obraz, informace, entropie (Czech) Image, Information, Entropy: Image Analysis Using Rényi Entropy. ProInflow: časopis pro informační vědy 11(2), 30–39 (2019).
2. Macková B., Lonhus K., **Rychtáriková R.***: Využití změn hejnové hierarchie ryb pro citlivou indikaci bioaktivních látek ve vodním prostředí. Vodní hospodářství 2, 21–26, 2022.

■ Významné inženýrské dílo většího rozsahu

■ Prototyp

1. Lonhus K., Karpov M., Larin I., **Rychtáriková R.**, Štys D., 2024: PADES. Uplatněno v *ASTOS Machinery a.s., Aš*.
2. **Rychtáriková R.**, Štys D., Sekorová Š., Špirka D., Tlamková M., Kopečková K., 2023: Mikroskop Visible Truth UltraEasy.
3. **Rychtáriková R.**, Štys D., Sekorová Š., Špirka D., Tlamková M., Kopečková K., 2023: Upravený Zeiss Stemi 508.

■ Funkční vzorek

1. Lonhus K., Karpov M., Larin I., **Rychtáriková R.**, Štys D., 2024: Filia 1.1. Uplatněno v *OSRAM Česká republika, s.r.o., Bruntál*.
2. Lonhus K., Karpov M., Larin I., **Rychtáriková R.**, Štys D., 2024: Filia 0.1. Uplatněno v *OSRAM Česká republika, s.r.o., Bruntál*.
3. Lonhus K., **Rychtáriková R.**, Štys D., 2021. Kapesní VIS (potenciálně near UV–VIS–near IR) spektrofotometr.
4. Štys D., **Rychtáriková R.**, 2021. Mikroskop Futurescope.
5. **Rychtáriková R.**, Štys D., 2020. Mikroskop NanoTruth.

■ Ověřená technologie

1. Tlamková M., Kopečková K., Sekorová Š., Špirka D., **Rychtáriková R.**, Štys D., 2023: Postup hodnocení a přípravy transplantátu z oční rohovky.

■ Ostatní výsledky, které nelze zařadit do žádného z definovaných druhů výsledků

1. Lonhus K., **Rychtáriková R.**, Štys D., 2019. Metodika sběru dat pro detekci osob.

■ Software

1. **Rychtáriková R.**, Štys D., 2020. CAMEX, <http://auc.cz/software/2020.php#CAMEX>.
2. Lonhus K., **Rychtáriková R.**, Štys D., 2020. QSP, <http://auc.cz/software/2020.php#QSP>.
3. Lonhus K., **Rychtáriková R.**, Štys D., 2020. FlowRec, <http://auc.cz/software/2020.php#FlowRec>.
4. **Rychtáriková R.**, Štys D., 2019. Control Software of the NanoTruth microscope, <http://auc.cz/software/2019.php#NanoTruth>.
5. Císař P., Urban J., Náhlík T., **Rychtáriková R.**, Štys D., 2015. Image Info Extractor Professional b9. <http://www.auc.cz/software/2015.php>. *Uplatněno v Elya Solutions s.r.o.*
6. Náhlík T., **Rychtáriková R.**, Štys D., 2015. LIL Convertor, <http://www.auc.cz/software/2015.php>. *Uplatněno v Elya Solutions s.r.o.*
7. **Rychtáriková R.**, Náhlík T., Štys D., 2015. Cell Segmentator, <http://www.auc.cz/software/2015.php>. *Uplatněno v Elya Solutions s.r.o.*
8. **Rychtáriková R.**, Náhlík T., Štys D., 2015. Organelle Extractor, <http://www.auc.cz/software/2015.php>. *Uplatněno v Elya Solutions s.r.o.*

■ Odborné knihy a učebnice

1. **Rychtáriková R.**, Štys D.: Moderní laboratorní cvičení z organické fyzikální chemie a analýzy. VUT Brno (2023), ISBN 978-80-214-6146-8.
2. **Rychtáriková R.**, Štys D.: Modern laboratory practices in physical organic chemistry and analysis. VUT Brno (2023), ISBN 978-80-214-6145-1.
3. **Rychtáriková R.**, Štys D.: Moderne Laborübungen in organischer physikalischer Chemie und Analytik. VUT Brno (2023), ISBN 978-80-214-6144-4.
4. **Rychtáriková R.**, Náhlík T.: Systémově informační přístup k digitální světelné mikroskopii. FROV JU České Budějovice (2023), ISBN 978-80-7514-193-4.

■ Přednášky

■ Zvané přednášky

1. Štys D., Lonhus K., Karpov M., **Rychtáriková R.**: Visible Truth – digitální světelné mikroskopy (nejen) pro kontrolu kvality. CAE Forum 2023, Praha, Česká republika, 14.–15. září 2023.
2. **Rychtáriková R.**: Use of Intracellular Dynamics in Sensitive Detection of Xenobiotics in Water. 1. Mezinárodní 6. Národní veterinární farmakologický a toxikologický kongres, Kayseri, Turecko, 4.–7. září 2019.
3. **Rychtáriková R.**: Superresolution Using Ordinary Microscopes, Life Science Meeting, Krems an der Donau, Rakousko, 18.–19. dubna 2018.
4. Štys D., **Rychtáriková R.**: Information Limits of Optical Microscopy, Optics, Algos & Ice, Obergurgl, Rakousko, 17.–20. listopadu 2016.
5. **Rychtáriková R.**, Štys D.: Low Discriminability Limits in Brightfield Microscopy and Liquid Chromatography: Data Handling Aspects and Imaging Examples, IBM Research Zürich, Rüschlikon, Švýcarsko, 15. září 2015.
6. Štys D., **Rychtáriková R.**: Chemical Self-Organisation modelling, Cellular Automata and Low Noise Limits for Natural Processes, IBM Research Zürich, Rüschlikon, Švýcarsko, 14. září 2015.
7. Štys D., **Rychtáriková R.**: Measures in Information Space: Point Information Gain Entropy Density and Rényi entropy in Image analysis, Experiments with Fish Behavior, Swarm Intelligence, IBM Research Zürich, Rüschlikon, Švýcarsko, 14. září 2015.
8. **Rychtáriková R.**: 3D Reconstruction of Diffracting Organelles inside Living Cells, ALMF EMBL, Heidelberg, Německo, 16. května 2014.

■ Mezinárodní konference

1. Štys D., **Rychtáriková R.**, Lonhus K.: Primary Sin of Multicolour Digital Imaging and Its Partial Absolution via Proper Image Capture and Calculation of Local Spectra in Visible Range. Sborník abstraktů, příspěvek OI-O-2351, Konference Mikroskopie 2021, České Budějovice, Česká republika, 13.–15. září 2021.
2. **Rychtáriková R.**, Georg Steiner, Gero Kramer, Michael Fischer, Dalibor Štys: Application of Rényi entropy-based 3D electromagnetic centroids to segmentation of fluorescing objects in tissue sections. Entropy 2021: The Scientific Tool of the 21st Century, 5.–7. května 2021, Online.

3. **Rychtáriková R.**, Štys D.: An information-entropic approach to the detection of observed object's volume response in fluorescence microscopy. Mikroskopie 2019, Lednice, Česká republika, 13.–15. května 2019.
4. Štys D., Macháček P., **Rychtáriková R.**: Tools for correct visual inspection of logical series of scientific images: LIL compression, Image Explorer and VerCa calibration. Mikroskopie 2019, Lednice, Česká republika, 13.–15. května 2019.
5. Štys D., Štys K. M., Zhyrova A., **Rychtáriková R.**: Optimal Noise in the Hodgepodge Machine Simulation of the Belousov-Zhabotinsky reaction, Automata 2016, Curych, Švýcarsko, 15.–17. června 2016.
6. Zhyrova A., **Rychtáriková R.**, Náhlík T.: Effect of Spatial Constrain on the Self-Organizing Behavior of the Belousov-Zhabotinsky Reaction, IWBBIO 2016, Granada, Španělsko, 20.–22. dubna 2016.
7. **Rychtáriková R.**, Štys D.: Correlative Light-Transmission Microscopy in Bright-Field and Transmission Electron Microscopy – Preliminary Results, Sborník abstraktů konference ČSMS (Book of Abstracts, CSMS Conference, Lednice, Česká republika, 3.–4. května 2016.
8. Štys D., Zhyrova A., Náhlík T., **Rychtáriková R.**: Reaction-Diffusion Processes, Cellular Automata, Interpretation of Chemical Self-Organisation, High Performance Computing in Science and Engineering, Hotel Soláň, Bzové-Karolinka, Česká republika, 25.–28. května 2015.
9. **Rychtáriková R.**: High-Resolution 3D Reconstruction of Organelles from Bright-Field Transmission Microscopic Images, IWBBIO, 15.–17. dubna 2015, Granada, Španělsko.
10. **Rychtáriková R.**, Náhlík T., Štys D.: Analysis of Living Cell 3D Inner Structures from High-Resolution Bright-Field Microscopy, XIII Discussion in Structural Molecular Biology, 19.–21. března 2015, Nové Hrady, Česká republika, abstract in Materials Structure, 22(1), 23 (2015).
11. Náhlík T., **Rychtáriková R.**, Štys D.: Description of Algorithm for Analysis and 3D Reconstruction of Living Cell Inner Structures from High-Resolution Bright-Field Microscopy Images, XIII Discussion in Structural Molecular Biology, Nové Hrady, Česká republika, abstrakt v Materials Structure, 22(1), 23 (2015).
12. Štys D., Urban J., **Rychtáriková R.**, Zhyrova A., Císař P.: Measurement in Biological Systems from the Self-Organisation Point of View, XIII Discussion in Structural Molecular Biology, Nové Hrady, Česká republika, abstrakt v Materials Structure, 22(1), 23 (2015).
13. **Rychtáriková R.**: 3D Reconstruction of Light-Diffracting Organelles of an Unlabelled Live Cell from Bright-Field Photon Transmission Microscopy

– Peeling PSFs, Microscopy New Zealand Conference 2015, Dunedin, Nový Zéland, 2.–4. února 2015.

14. **Rychtáriková R.:** Multifractality in Imaging: Application of Information Entropy for Observation of Inner Dynamics Inside of an Unlabeled Living Cell in Bright-Field Microscopy, Interdisciplinary Symposium on Complex Systems, Florencie, Itálie, 15.–18. září 2014.

■ České konference

1. **Rychtáriková R.,** Pejcharová E., Lonhus K.: Změny hejnového chování akvariálních ryb v přítomnosti kontaminantu. XX. Toxikologická konference: Toxicita a biodegradabilita odpadů a látek významných ve vodním prostředí. Vodňany, Česká republika, 24.–25. srpna 2022.
2. Štys D., Lonhus K., Karpov M., Larin I., **Rychtáriková R.:** Kapesní spektrofotometr UU´Spe. XX. Toxikologická konference: Toxicita a biodegradabilita odpadů a látek významných ve vodním prostředí. Vodňany, Česká republika, 24.–25. 8. 2022.
3. Pejcharová E., Lonhus K., **Rychtáriková R.,** Štys D.: Vysoce citlivá a specifická biodetekce polutantů. Elektronický sborník prezentací z konference Pitná voda 2020–2021, ISBN 978-80-905238-4-5. Ed. Petr Dolejš (WET Team).
4. **Rychtáriková R.,** Lonhus K., Slivoně M., Štys D.: Citlivá detekce nových (i starých) polutantů založená na změnách intracelulární pohyblivosti živočišných buněk. Elektronický sborník prezentací z konference Pitná voda 2020–2021, ISBN 978-80-905238-4-5. Ed. Petr Dolejš (WET Team).

■ 43 plakátových sdělení na mezinárodních a národních konferencích

■ 7 Tabulka dosažených kvantifikovaných hodnotících oborových kritérií

A) ODBORNÁ OBLAST

pol. * korespondující autor

bod.

1	Recenzovaný odborný článek (výsledek Jimp), Q1**)	
	Lonhus K., Štys D., Rychtáriková R.* : Quantification of Collective Behaviour via Causality Analysis. Complex Intell. Syst. 9, 5807–5816 (2023).	40
	Ghaznavi A., Rychtáriková R.* , Saberioon M., Štys D.: Cell Segmentation from Telecentric Bright-field Transmitted Light Microscopy Images Using a Residual Attention U-Net: A Case Study on HeLa Line. Comp. Biol. Med. 147, 105805 (2022).	40
	Lonhus K., Rychtáriková R. , Platonova G., Štys D.: Quasi-Spectral Characterization of Intracellular Regions in Bright-Field Light Microscopy Images. Sci. Rep. 10, 18346 (2020).	40
	Rychtáriková R.* , Náhlík T., Shi K., Malakhova D., Macháček P., Smaha R., Urban J., Štys D.: Super-Resolved 3-D Imaging of Live Cells' Organelles from Bright-Field Photon Transmission Micrographs, Ultramicroscopy 179, 1–14 (2017).	40
	Rychtáriková R.* , Seisenbaeva G. A., Kuncova G., Kessler V. G.: Biocompatible Titania Hydrogels with Chemically Triggered Release of a Photosensitive Dye. J. Sol-Gel Sci. Technol. 62(3), 370–377 (2012).	40
	Rychtáriková R.* , Sabata S., Hetflejš J., Kuncova G.: Composites with Photosensitive 5,10,15,20-Tetrakis(<i>N</i> -methylpyridinium-4-yl)porphyrin Entrapped into Silica Gels. J. Sol-Gel Sci. Technol. 61(1), 119–125 (2012).	40
2	Recenzovaný odborný článek (výsledek Jimp), Q2**)	
	Ghaznavi A., Rychtáriková R. , Císař P., Ziaei M.M., Štys D.: Symmetry Breaking in the U-Net: Hybrid Deep-Learning Multi-Class Segmentation of HeLa Cells in Reflected Light Microscopy Images. Symmetry 16, 227 (2024).	20
	Platonova G., Štys D., Souček P., Lonhus K., Valenta J., Rychtáriková R.* : Spectroscopic Approach to Correction and Visualization of Bright-Field Light Transmission Microscopy Biological Data. Photonics 8(8), 333 (2021).	20
	Lonhus K., Rychtáriková R. , Ghaznavi A., Štys D.: Estimation of Rheological Parameters for Unstained Living Cells. Eur. Phys. J.-Spec. Top. 230(4), 1105–1112 (2021).	20
	Lonhus K., Štys D., Saberioon M., Rychtáriková R. : Segmentation of Laterally Symmetric Objects: Application to Images of Collective Animal Behavior. Symmetry 11(7), 866 (2019).	20
	Štys D., Rychtáriková R.* , Zhyrova A., Štys K.M., Jizba P.: Noisy Hodgepodge Machine and the Observed Mesoscopic Behaviour in the Non-Stirred Belousov-Zhabotinsky Reaction: Optimal Noise and Hidden Noise in the Hodgepodge Machine, Eur. Phys. J.-Spec. Top. 227, 2361–2374 (2019).	20
	Rychtáriková R.* , Korbek J., Macháček P., Štys D.: Point Divergence Gain and Multidimensional Data Sequence Analysis. Entropy 20(2), 106 (2018).	20
	Rychtáriková R.* , Korbek J., Macháček P., Císař P., Urban J., Štys D.: Point Information Gain and Multidimensional Data Analysis, Entropy 18(10), 372 (2016).	20
3	Recenzovaný odborný článek (výsledek Jimp), Q3**)	
	Rychtáriková R.* , Sabata S., Hetflejš J., Kuncova G.: Photodynamic Efficiency of Porphyrins Encapsulated into Polysilsesquioxanes. <i>Chem. Pap.</i> , 66(4), 269–277 (2012).	10
	Rychtáriková R.* , Kuncová G.: Imobilizované fotosenzitizátory singletového kyslíku a jejich účinek na mikroorganismy. Chem. Listy 103(10), 800–813 (2009).	10
	Šabata S., Hetflejš J., Rychtáriková R. , Kuncová G., Lang K., Kubát P.: Immobilization of Porphyrins in Poly(hydroxymethyl-siloxane). Chem. Pap. 63(4), 438–444 (2009).	10
4	Recenzovaný odborný článek (výsledek Jimp), Q4 **)	
	Malakhova D., Štys D., Rychtáriková R. : Adjustment of Dynamic High Resolution Images of Living Cells by Combination of an Optical Microscopy in Transmitting Light, Atomic Force Microscopy and Image Information Analysis, Chem. Listy 107(SI), Suppl. 3, S402–S404 (2013).	5
	Rychtáriková R.* , Kuncová G.: Metoda vyhodnocování antimikrobiální aktivity počítačovým prahováním barev. Chem. Listy , 105(6), 493–498 (2011).	5

5	Recenzovaný odborný článek (výsledek Jsc) **)	
	Urban J., Rychtáriková R. , Macháček P., Štys D., Urbanová P., Císař P.: Optimization of Computational Burden of the Point Information Gain. Acta Polytech. 59(6) , 593–600 (2019).	2.5
	Rychtáriková R.* , Urban J., Štys D.: Žampa's Systems Theory: a Comprehensive Theory of Measurement in Dynamic Systems, Acta Polytech. 58(2) , 128–143 (2018).	2.5
	Rychtáriková R.* , Štys D.: Observation of Dynamics Inside an Unlabeled Live Cell Using a Bright-Field Photon Microscopy: Evaluation of Organelles' Trajectories. IWBBIO 2017, Proceedings, Part II, LNBI 10209 , Ortuno and Rojas (eds.), Springer, Switzerland, 2017, pp. 700–711.	2.5
	Rychtáriková R.* , Steiner G., Fischer M. B., Štys D.: Information Limits of Optical Microscopy: Application to Fluorescently Labelled Tissue Section. IWBBIO 2017, Proceedings, Part I, LNBI 10208 , Ortuno and Rojas (eds.), Springer, Switzerland, 2017, pp. 485–496.	2.5
	Zhyrova A., Rychtáriková R. , Štys D.: Recognition of Stages in the Belousov-Zhabotinsky Reaction Using Information Entropy. IWBBIO 2017, Proceedings, Part I, LNBI 10208 , Ortuno and Rojas (eds.), Springer, Switzerland, 2017, pp. 335–346.	2.5
	Štys D., Náhlík T., Macháček P., Rychtáriková R. , Saberioon M.: Least Information Loss (LIL) conversion of digital images and lessons learned for scientific image inspection. IWBBIO 2016, LNBI 9656 , Ortuno and Rojas (eds.), Springer, Switzerland, 2016, pp. 527–536.	2.5
	Císař P., Náhlík T., Rychtáriková R. , Macháček P.: Visual Exploration of Principles of Microscopic Image Intensities Formation using Image Explorer Software. IWBBIO 2016, LNBI 9656 , Ortuno and Rojas (eds.), Springer, Switzerland, 2016, pp. 537–544.	2.5
	Rychtáriková R.* : Clustering of Multi-Image Sets Using Rényi Information Entropy. IWBBIO 2016, LNBI 9656 , Ortuno and Rojas (eds.), Springer, Switzerland, 2016, pp. 517–526.	5
	Štys D., Náhlík T., Zhyrova A., Rychtáriková R. , Papáček Š., Císař P.: Model of the Belousov-Zhabotinsky Reaction. HPCSE 2015, LNCS 9611 , Kozubek, Blaheta, Šístek, Rozložník, Čermák (Eds.), Springer, Switzerland, 2016, pp. 171–185.	2.5
	Štys D., Urban J., Rychtáriková R. , Zhyrova A., Císař P.: Measurement in Biological Systems from the Self-Organisation Point of View. IWBBIO 2015, Part II, LNCS 9044 , Ortuno and Rojas (eds.), Springer, Switzerland, 2015, pp. 431–443.	2.5
Bárta A., Císař P., Soloviov D., Souček P., Štys D., Papáček Š., Pautsina A., Rychtáriková R. , Urban J.: BioWes – from Design of Experiment, through Protocol to Repository, Control, Standardization and Back Tracking. IWBBIO 2015, Part II, LNCS 9044 , Ortuno and Rojas (eds.), Springer, Switzerland, 2015, pp. 426–430.	2.5	
6	Recenzovaný odborný článek (výsledek Jost) **)	
	Malečková D., Rychtáriková R. , Urban J.: Obraz, informace, entropie (Czech) Image, Information, Entropy: Image Analysis Using Rényi Entropy. ProInflow: časopis pro informační vědy 11(2), 30–39 (2019).	2.5
	Macková B., Lonhus K., Rychtáriková R.* : Využití změn hejnové hierarchie ryb pro citlivou indikaci bioaktivních látek ve vodním prostředí. Vodní hospodářství 2, 21–26, 2022.	2.5
7	Odborná kniha (výsledek B, za 1 stranu) **)	
	Rychtáriková R. , Náhlík T.: System information approach to digital light microscopy. FROV JU České Budějovice (2023), ISBN 978-80-7514-185-9, 124 str.	49.6
9	Stať ve sborníku (výsledek D) **)	
	Štys D., Lonhus K., Karpov M., Rychtáriková R. : Visible Truth – digitální světelné mikroskopy (nejen) pro kontrolu kvality. CAE Forum 2023, Praha, Česká republika, 14.–15. září 2023.	1
	Rychtáriková R.* , Malečková D., Urban J., Bárta A., Novotná M., Zhyrova A., Náhlík T., Štys D.: Study of Human Perception with the Usage of Information Entropy Analysis of Patterns, in PURPLSOC: Pursuit of Pattern Language for Societal Challenges/PURPLSOC The Workshop 2014 1), Baumgartner and Sickinger (eds.), pp. 366–384, ISBN 978-3-7375-5458-9, epubli GmbH (Verlag), 2015, Austria.	1

	Zhyrova A., Rychtáriková R. , Náhlík T., Štys D.: The Path of Aging: Self-Organization in Nature and 15 Properties, in PURPLSOC: Pursuit of Pattern Language for Societal Challenges/PURPLSOC The Workshop 2014 1), Baumgartner and Sickinger (Eds.), pp. 385–410, ISBN 978-3-7375-5458-9, epubli GmbH (Verlag), 2015, Austria.		1
	Rychtáriková R.* , Náhlík T., Smaha R., Urban J., Štys D. Jr., Císař P., Štys D.: Multifractality in Imaging: Application of Information Entropy for Observation of Inner Dynamics Inside of an Unlabeled Living Cell in Bright-Field Microscopy. In ISCS14, Sanayei et al. (eds.), Springer, Switzerland, 2015, pp. 261–267.		1
10	Citace jiným autorem podle WoS		
		59	118
14	Ověřená technologie (výsledek Z)		
	Tlamková M., Kopečková K., Sekorová Š., Špirka D., Rychtáriková R. , Štys D., 2023: Postup hodnocení a přípravy transplantátu z oční rohovky.		5
17	Prototyp (výsledek G)		
	Lonhus K., Karpov M., Larin I., Rychtáriková R. , Štys D., 2024: PADES. <i>Uplatněno v ASTOS Machinery a.s., Aš.</i>		5
	Rychtáriková R. , Štys D., Sekorová Š., Špirka D., Tlamková M., Kopečková K., 2023: Mikroskop Visible Truth UltraEasy.		5
	Rychtáriková R. , Štys D., Sekorová Š., Špirka D., Tlamková M., Kopečková K., 2023: Upravený Zeiss Stemi 508.		5
18	Funkční vzorek (výsledek G)		
	Lonhus K., Karpov M., Larin I., Rychtáriková R. , Štys D., 2024: Filiqa 1.1. <i>Uplatněno v OSRAM Česká republika, s.r.o., Bruntál.</i>		5
	Lonhus K., Karpov M., Larin I., Rychtáriková R. , Štys D., 2024: Filiqa 0.1. <i>Uplatněno v OSRAM Česká republika, s.r.o., Bruntál.</i>		5
	Lonhus K., Rychtáriková R. , Štys D., 2021. Kapesní VIS (potenciálně near UV–VIS–near IR) spektrofotometr.		5
	Štys D., Rychtáriková R. , 2021. Mikroskop Futurescope.		5
	Rychtáriková R. , Štys D., 2020. Mikroskop NanoTruth.		5
25	Získání externího grantu (řešitel, spoluřešitel)		
	Lamelový sedimentační systém filtrace nové generace , TAČR Trend PPI Technologičtí lídři, 1/2024–6/2026, rozpočet FROV JU 6 328 tis. Kč (90% dotace) – spolupráce s firmami ASTOS Machinery a.s. a MACHINERY DESIGN s.r.o. (Ing. Martin Valíček).		40
	Vývoj procesu hodnocení kadaverózních rohovkových lamel pomocí inovace mikroskopických systémů pro celulární analýzu , MPO Aplikace, 9/2021–5/2023, rozpočet FROV JU 3 218 tis. Kč (85% dotace) – spolupráce s firmami PrimeCell Bioscience a Národním centrem tkání a buněk (MUDr. Šárka Sekorová, Mgr. Martina Tlamková)		40
	Návrh a ověření metody pro analýzu částic v provozních kapalinách pomocí mikroskopu s průtokovou celou , MPO Inovační vouchery VI, 12/2022–7/2022, 587 tis. Kč, pro ASTOS Machinery a.s., Aš.		40
	Testování principů mikroskopického sledování kvality navíjení mikrospirály wolframového vlákna pro žárovky , MPO Inovační vouchery VI, 12/2022–7/2022, 604 tis. Kč, pro dataPartner s.r.o., České Budějovice.		40
	Konsolidace software jednoduchého mikroskopu velmi vysokého rozlišení NanoTruth , TAČR Gamma, TG03010027, 4/2018–12/2019, 218 tis. Kč.		40
	SOUČET		871.6
	MINIMUM		600

B) PEDAGOGICKÁ OBLAST

pol.		bod.
1	Za každý rok pedagogického působení na vysoké škole na plný úvazek (částečné úvazky se sčítají)	
		12 300
5	Garantování předmětů (za každý rok)	
	od 9/2021 – <i>Technické normy</i> – semestrální Bc. kurz pro obor Ochrana vod	15
6	Zavedení nového předmětu nebo zásadní inovace předmětu	
	<i>Chemie 2</i> – semestrální Bc. kurz pro obory Ochrana vod a Rybářství, celková inovace předmětu, zodpovědná za inovaci laboratorních cvičení	10
	<i>Bioinformatika/Bioinformatics</i> – semestrální Bc. kurz pro obory Ochrana vodních ekosystémů, zavádění nového předmětu v rámci nového studijního oboru, zodpovědná za inovaci oblasti světelné mikroskopie	10
8	Vedení úspěšně obhájené bakalářské práce	
	Alisa Plaksina: Caffeine-induced changes in a shoal behaviour of Tiger Barb (<i>Puntigrus tetrazona</i>), obhájeno 13. 10. 2021.	3
	Jan Košek: Studium dynamiky živých lidských buněk v odezvě na běžné kontaminanty vod s cílem vývoje citlivého specifického analytického postupu, obhájeno 6. 6. 2023.	3
	Eliška Pejcharová: Změny hejnového chování akvariálních ryb v přítomnosti kontaminantu, obhájeno 14. 6. 2022.	3
	Barbora Macková: Změny hejnové hierarchie ryb jako citlivý indikátor bioaktivních látek, obhájeno 14. 6. 2021.	3
	Miroslav Slivoně: Vliv běžných pesticidů na lidské buňky, obhájeno 1. 7. 2020.	3
12	Školitel specialista studenta, který získal Ph.D.	
	Ali Ghaznavi: Cell segmentation from wide-field light microscopy images using CNNs, obhájeno 26. 6. 2023.	10
	Kirill Lonhus: Investigating intrinsic behavioural parameters of autonomous objects based on motion, obhájeno 2. 2. 2022.	10
	Anna Zhyrova: State trajectory approach to the interpretation of self-organization in the Belousov-Zhabotinsky reaction, obhájeno 24. 11. 2017.	10
	Tomáš Náhlík: Microscopy – Point Spread Function, Focus, Resolution, obhájeno 15. 1. 2016	10
13	Učebnice s ISBN (za 1 stranu)	
	Rychtáriková R., Náhlík T.: Systémově informační přístup k digitální světelné mikroskopii. FROV JU České Budějovice (2023), ISBN 978-80-7514-193-4, 124 str.	49.6
14	Skripta s ISBN (za 1 stranu)	
	Rychtáriková R., Štys D.: Moderní laboratorní cvičení z organické fyzikální chemie a analýzy. VUT Brno (2023), ISBN 978-80-214-6146-8, 50 str.	20
	Rychtáriková R., Štys D.: Modern laboratory practices in physical organic chemistry and analysis. VUT Brno (2023), ISBN 978-80-214-6145-1, 50 str.	20
	Rychtáriková R., Štys D.: Moderne Laborübungen in organischer physikalischer Chemie und Analytik. VUT Brno (2023), ISBN 978-80-214-6144-4, 52 str.	20.8
SOUČET		500.4
MINIMUM		200

8 Vyjádření uchazečky k bodovému hodnocení

Odborná oblast

V **odborné oblasti (část A)** dosahuje uchazečka dle tabulky kvantifikovaných hodnotících oborových kritérií FCH VUT **871.6 b.** z povinných 600 b.

Silnými stránkami této oblasti je

- relativně vysoký počet udělených externích grantů jako PI nebo co-PI (srovnáno dle výše finanční podpory) 1× TAČR Trend 10, 1× MPO Aplikace, 2× MPO Inovační vouchery, 1× TAČR Gama, a z toho vyplývající
- vysoký počet aplikovaných výsledků (1× ověřená technologie, 3× prototyp a 4× funkční vzorek). Kromě těchto kvantifikovaných aplikovaných výstupů žadatelka vykázala ještě 8× software (kap. 6).
- vysoký podíl práce uchazečky na publikacích. Včetně monografie, studijních opor a recenzovaných článků bez IF je uváděna 19× jako první, 5× jako poslední, 18× jako korespondující, případně 9× jako druhá autorka.

Slabšími stránkami této oblasti je

- hraniční počet publikací s IF (18 vs. 15 povinných). Jedním z důvodů je relativně vysoký počet článků publikovaných v recenzovaných technických sbornících vydavatelství Springer (9× Q2 dle SJR, citováno na WoS bez IF). Dalším důvodem je nízký počet spoluautorů na publikacích, kdy na práci spolupracoval s uchazečkou většinou pouze její nadřízený, případně další 1–2 studenti.
- hraniční počet citací (59 dle Scopus vs. 50 povinných). Důvodem je obecně nižší citovanost matematicko-fyzikálních článků.

Pedagogická oblast

V **pedagogické oblasti (část B)** dosahuje uchazečka dle tabulky kvantifikovaných hodnotících oborových kritérií FCH VUT **500.4 b.** z povinných 200 b.

Silnou stránkou této oblasti je

- relativně vysoký počet studijních opor (1× učebnice ve dvou jazykových mutacích, viz monografie; 1× skriptá ve třech jazykových mutacích). Tyto studijní opory byly základem inovace a zavádění nových studijních předmětů na FROV JU a ZTF JU (viz položka 6B).

Slabou stránkou této oblasti je

- nedostatečný počet povinně vykazovaných ukončených bakalářských či diplomových prací (5 vs. 6 povinných). Nicméně uchazečka vykazuje 4 ukončené doktorské práce jako školitel-specialista, další doktorská práce

bude pravděpodobně obhájena do konce 11/2024 (kap. 3). Hlavním důvodem je nízký počet (v jednotkách) studentů ukončujících každoročně na FROV JU bakalářské či magisterské studium a vysoký počet školitelů. Naopak FROV JU se prezentuje jako fakulta výzkumná a vykazuje tedy vysoký počet studentů doktorského studia.

■ 9 Pět nejvýznamnějších publikací

■ Noisy hodgepodge machine and the observed mesoscopic behavior in the non-stirred Belousov-Zhabotinsky reaction

D. Štys, **R. Rychtáriková**, A. Zhyrova, K. M. Štys a P. Jizba, *Noisy hodgepodge machine and the observed mesoscopic behavior in the non-stirred Belousov-Zhabotinsky reaction*, The European Physical Journal – Special Topics **227** (2019), 2361–2374.

Jedná se o základní fyzikálně-chemický výzkum principů samoorganizace na příkladu Bělousovy-Zhabotinského reakce, jejího experimentálního měření a matematického modelování. Tato práce navazuje na předchozí publikace

- D. Štys, T. Náhlík, A. Zhyrova, **R. Rychtáriková**, Š. Papáček a P. Císař, *Model of the Belousov-Zhabotinsky reaction*, In: Kozubek, Blaheta, Šístek, Rozložník a Čermák (Ed.) High Performance Computing in Science and Engineering (HPCSE) 2015, Lecture Notes in Computer Science **9611**, Springer, Switzerland (2016), pp. 171–185.
- A. Zhyrova, **R. Rychtáriková** a D. Štys, *Recognition of stages in the Belousov-Zhabotinsky reaction using information entropy: Implications to cell biology*, In: Ortuño a Rojas (Ed.) International Conference on Bioinformatics and Biomedical Engineering (IWBBIO) 2017, Part I, Lecture Notes in Computer Science **10208**, Springer, Switzerland (2017), pp. 335–346.

Do všech předchozích modelů vnesli autoři náhodnou složku (šum) nevědomky, případně zaváděli pouze jeden druh šumu, a to gaussovský. My jsme šum cíleně modelovali pro jednotlivé procesy, čímž jsme dosáhli velmi dobré shody modelu s experimentem.

Noisy hodgepodge machine and the observed mesoscopic behavior in the non-stirred Belousov–Zhabotinsky reaction^{*}

Optimal noise and hidden noise in the hodgepodge machine

Dalibor Štys¹, Renata Rychtáriková^{1,a}, Anna Zhyrova¹, Kryštof M. Štys¹, and Petr Jizba²

¹ University of South Bohemia in České Budějovice, Faculty of Fisheries and Protection of Waters, South Bohemian Research Center of Aquaculture and Biodiversity of Hydrocenoses, Kompetenzzentrum MechanoBiologie in Regenerativer Medizin, Institute of Complex Systems, Zámek 136, 373 33 Nové Hradky, Czech Republic

² Faculty of Nuclear Sciences and Physical Engineering, Czech Technical University in Prague, Prague 1, Czech Republic

Received 10 April 2018 / Received in final form 28 July 2018
Published online 31 January 2019

Abstract. In this paper, we have modified one of the simplest multi-level cellular automata – a hodgepodge machine, so as to represent the best match for the chemical trajectory observed in the Belousov–Zhabotinsky reaction (BZR) in a thin layered planar setting. By introducing a noise term into the model, we were able to transform the central regular structure into the circular target pattern. We further analyze influences of the neighborhood (diffusion process) and internal excitation type of noise. We find that the configurations of ignition points, which give the target patterns, occur only in the interval of the neighborhood excitation noise from 30% to 34% and at the internal excitation noise of 12%. We argue that the BZR occurs on a semi-regular grid – a chemical analogy to a Bénard cell in the viscous fluid, and we discuss the size of the relevant elementary cell. In this way, the BZR is a quintessential example of mesoscopic process, in particular, it does follow neither the deterministic rules of the microscopic system nor the tenet of Boltzmannian statistic physics that only the most frequent events are observed.

1 Introduction

Properties of multi-level cellular automata [1,2] have been examined so far only sporadically. What is known, however, is that their state trajectory critically depends on the number of available levels [3] and that they can be divided into a few-level

^{*} Supplementary material in the form of one zip file available from the Journal web page at <https://doi.org/10.1140/epjst/e2018-800045-4>

^a e-mail: rrychtarikova@frov.jcu.cz

automata and true multilevel automata [4]. The border between a few and true multilevel automata was examined only for the so-called square Moore neighborhood and was found to be around 24 levels [3]. Such automata have apparently a sufficient number of levels which allows the system to behave only according to the internal evolution rule (e.g., ratio of constants) independently of the number of levels itself [4].

The *hodgepodge machine* [5] is a type of multi-level cellular automaton which mimics well the final phase of the Belousov–Zhabotinsky reaction (BZR). The *hodgepodge machine* is the simplest of the models which intends to mimic qualitatively the features observed when the BZR is performed in a thin layer. In the context of this paper it is important to mention the simulation of Garcia-Ojarvo and Schimansky-Geier [6] who used the FitzHugh–Nagumo model [7,8] for description of the rise and decay of the excitation. The simulation was performed on a square lattice and may be thus directly compared to the hodgepodge machine. When an adequate level of the Gaussian noise was added, the coexistence of spirals and waves, similar to that in the hodgepodge machine, was observed. The FitzHugh–Nagumo model was originally developed for description of the electrical pulse in the neural system but may be also interpreted in terms of a chemical simplified reaction-diffusion system of chemical transformations.

In our simulations, we modified the model so that it was possible to start from a few ignition points – situation observed in realistic experiments [4]. This enabled us to examine influences of the ignition points as well as the early phases of the trajectory. Eventually, we achieved such a behavior of the hodgepodge machine which is qualitatively compatible with the BZR and consists from an early phase of large center structures – octagons filled by complicated cross-like structures – and ends with a mixture of spirals and waves [4]. The latter suggests that it could be some conceptual overlap between our model and the discrete dynamic networks paradigm proposed in [9].

Our aim here is to promote the idea that the BZR as a typical demonstration of mesoscopic dynamics, i.e., it is neither microscopic, i.e. fully deterministic, nor macroscopic, i.e. represented only by the most probable microstate. The paper is structured as follows: In Section 2, we examine influences of noise on the outputs from the noise-enriched hodgepodge machine (NHM) and discuss the relevance it bears on the BZR. In Section 3, we present results of our simulations and show that the conventional, i.e., “noise-free” hodgepodge machine is in fact a hidden-noise cellular automaton. We also show that many details of the NHM find their direct analogues in the BZR. We further explain the lag phase in the beginning of the BZR using a chemical mechanism analogous to the formation of a regular grid by a Bénard–Rayleigh convection process [10]. Various remarks and generalizations are addressed in Section 4.

2 Materials and methods

2.1 Performance of the chemical reaction

The experiments were performed using the BZR recipe [11]. The reaction mixture included 0.34-M sodium bromate, 0.2-M sulphuric acid, 0.057-M sodium bromide (all from Penta), 0.11-M malonic acid (Sigma-Aldrich) as substrates and a redox indicator and 0.12-M 1,10-phenanthroline ferrous complex (Penta) as a catalyst. All reagents were mixed by hand directly in a 200-mm Petri dish in the sequence mentioned above for 1 min. A special thermostat, which was constructed from a Plexiglas aquarium and a low-temperature circulating water bath-chiller, fixed a reaction temperature at 26 °C.

The chemical waves were recorded by a Nikon D90 camera in the regime of Time lapse (10 s/snapshot) with exposure compensation +2/3 EV, ISO 320, aperture $f/18$, and shutter speed 1/10 s. The original 12-bit NEF raw image format was losslessly transformed to the 12-bit PNG format. The complete courses of the experiment are provided in Videos S1 and S2.

The experiment on a re-started BZR was performed by a manual re-shaking of the reaction vessel after reaching the state of dense waves. The photos of course of the experiment were taken in the time interval of 2 s and consists of 9 cycles of the lengths of 48, 25, 44, 24, 25, 18, 11, 15, and 32 images, respectively.

2.2 Noisy hodgepodge machine model

The NHM of the BZR is essentially the same as in [4] but with the addition of a noise term. We adjusted Wilensky’s NetLogo model [12]: The model was run on a square 1-Mpx grid. Ignition centers in $state(t = 0) \in [0, maxstate]$ were randomly set on the grid as

$$state(t = 0) = \text{random-exponential}[meanPosition(maxstate + 1)], \quad (1)$$

where $maxstate$ is the maximally achievable number of levels of the cell state. Multiplication of each cell state by the $meanPosition$ of the exponential distribution ensured that the simulation started with a small number of the ignition points. Each time step t proceeded in four possible ways:

- When a cell was at the $state(t) = 0$, so-called *quiescent*, it was “infected” by surrounding cells according to the equation

$$state(t + 1) = (1 + PTN) \left[\text{prec} \left(\frac{a}{k_1} \right) + \text{prec} \left(\frac{b}{k_2} \right) \right], \quad (2)$$

where a and b is a number of cells at the $state \in (0, maxstate)$ and $state = maxstate$, respectively, k_1 and k_2 are characteristic constants of the process.

- When a cell was at the $state(t) \in (0, maxstate)$, its new state was calculated as

$$state(t + 1) = \text{prec} \left[\frac{state(t) + \sum_{n=1}^8 state_n(t)}{a + b + 1} (1 + IEN) + g(1 + EEN) \right], \quad (3)$$

where $state_n(t)$ is a state of the n th cell in the Moore neighborhood, which directly surrounds the examined cell, and $g = 28$ is another arbitrary constant.

- When a cell was at the $state(t) > maxstate$, then

$$state(t + 1) = maxstate. \quad (4)$$

- When a cell achieved the $state(t) = maxstate$, then

$$state(t + 1) = 0. \quad (5)$$

In equations (1) and (2), the numerical precision (prec) of 10 decimal points allowed us to realize up to 9×10^{12} states. The individual white noises in equations (1) and (2) were named

- the phase transition noise (*PTN*): it affects the transition from the state 0 to the first non-zero state,
- the internal excitation noise (*IEN*): it affects the change of the state due to processes inside the cell, i.e., it influences the constant g [4], and
- the neighborhood (external) excitation noise (*EEN*): it affects processes related to the values of neighboring cells.

The influences of these kinds of noise were tested by systematic changes of their values. Examples of qualitatively different cases are described in some detail in the following section and shown in Videos S3–S8. The full model is provided in Material S1.

3 Results

3.1 Modeling the Belousov–Zhabotinsky reaction in excitable media and the constructive role of noise

The BZR behavior is not easily comprehensible in terms of the standard Law of Mass Action (which represents the “canonical method” for interpretation of the chemical reactivity) due to the fact that the reaction space is separated into regularly evolving/traveling structures and, thus, one has to consider a large number of interlocked chemical processes. In this work, we report a new stochastic model of the BZR based on the cellular automaton. The model retains some of the key features of the multi-level hodgepodge machine but outperforms this hodgepodge machine in the ability to faithfully mimic the onset stage of the BZR and in the potential to correctly describe the morphology of the evolving wave-spiral patterns.

Figure 1a compares a late (ergodic) stage of the BZR (full data are accessible via S1 Video) at our least spatially constrained (a 200-mm Petri dish) and roil (gentle mixing at 1400 rpm using an orbital mixer) conditions with one of our Wilensky-like model. The structures of the model, which are astonishingly similar to the experiment, arise only at the particular ratio of the model constants independently of the height of the noise. (The most regular spirals and waves, best comparable to the model, are expected to arise in a very gently pre-mixed, homogenous solution of a thin layer in a vessel of the unlimited size which does not spatially constrain evolving waves.) In order to achieve this morphological similarity between the BZR and our simulation, we implemented the following changes into the Wilensky model:

- the enlargement of the cellular grid to 1000×1000 ,
- start from a very few points which enabled to analyze the behavior of individual centers of emanation,
- a sequence of switching the values of cell states from natural to decimal numbers which extended the span of each cellular state,
- the addition of a uniform white noise to each automaton step which compensated for our limited knowledge of precise underlying mechanism, and
- the extension of the number of achievable states *maxstate* and rate of the internal cell excitation g up to 2000 and 280, respectively, to smooth the model waves.

The first modification – usage of the larger grid – suppressed to some extent the influence of the non-idealities of the periodic boundaries on the evolution of the model system.

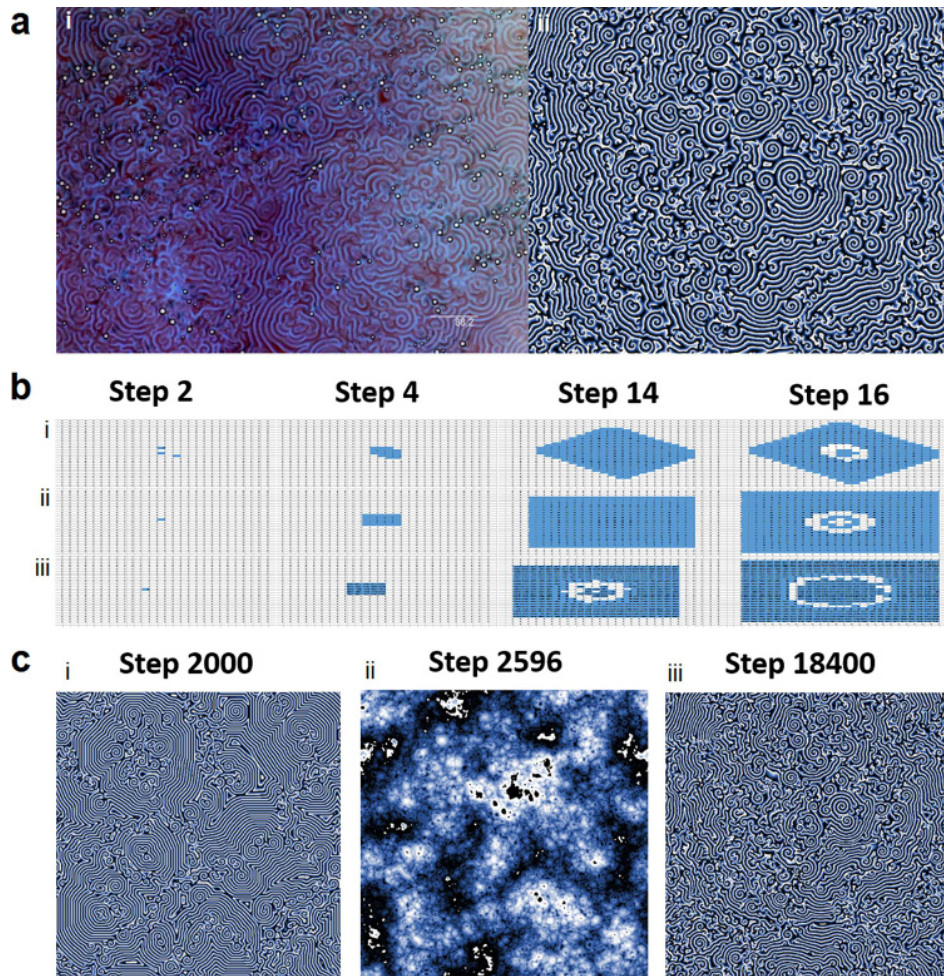


Fig. 1. Illustration of the key aspects of the B-Z model. (a) Comparison of the BZR (i) with the simulation with the levels of noise 9%, 14% and 30% for process 1, 2a, and 2b, respectively, and $k_1 = 3$ and $k_2 = 3$ (ii). Images were expanded so as to have comparable widths of traveling waves. (b) Starting points of the simulations (steps 2, 4, 14, 16). The noise-free simulation with natural number states, $k_1 = 3$ and $k_2 = 3$ in step 2000 (i), the noise-free simulation with natural number states, $k_1 = 2$ and $k_2 = 2$ in step 2596 (ii) and the process described under a in step 18400 (iii). (c) Final states (limit sets) of processes defined in b. For all processes, $g = 28$ and $maxstate = 200$. In the simulation, the black and white corresponds to 0 and $maxstate$, respectively. Original datasets are supplied in S1 File. The unquestionably inspection of the data has to be done using the original data matrices as demonstrated in Figure 1.

The second intervention into the Wilensky model was performed through a random-exponential function for generation of the starting (ignition) points. This modification, which was originally implemented to start the process from these few centers (ignition points), quite surprisingly increased the morphological similarity between the BZRs and the simulation. The results are depicted in Figures 1b and 1c. In Figure 1b, we present early simulation steps 2, 4, 14, and 16 in process 1 after the ignition. For $k_1 = 3$ and $k_2 = 3$, at least two non-zero points in a proper configuration

a , b were required for the evolution of the waves in the simulation, since at least one addend in process 1 has to be equal to 1. In this case, the early evolution yielded octagons (Fig. 1b, i), while the final state was populated by spirals (Fig. 1c, i). In contrast, if $k_1 = 2$ and $k_2 = 2$, then, e.g. $state(t+1) = \text{round}(\frac{1}{2}) + \text{round}(\frac{0}{2}) = 1$ and the non-zero cell was surrounded by evolving wave of 8 cells in $state(t+1) = 1$. This early evolution resulted in squares with central circular objects (Fig. 1b, ii) which further led to the filamentous structures (Fig. 1c, ii).

The next step softened the definition of the state by allowing 1 decimal place in equations (1) and (2). This modification, however, neglected the condition of the asymmetry for the ignition process and, as a consequence, the development of trajectories could start from any non-zero. Thus, as such, this modification leads only to fuzzy distribution of points. Indeed, increase of the number of decimal places did not have any further effect.

In other words, the implementation of white noise compensated for the need of multiple neighboring points for the realization of the waves' ignition. The different options for setting the ignition points occur randomly and are thus the noise themselves. By the term noise we understand a process with its own internal mechanism which occurs at a rate faster than the rate of the main process (i.e., waves' formation) which it affects. Thus, the original hodgepodge machine was an unrecognized noisy cellular automaton.

The only effect of higher number of decimal points were smoother edges in the spiral shape.

The detailed comparison of the models and experiment is given in Figure 2a. The sequence of simulated structures is the following:

- The simulation grid is filled with systems of square dense waves. This has not been observed in the experiment and we interpret it as a *lag phase*, which precedes the observed formation of circular waves.
- Circular structures emanate from the center of square waves.
- At the certain state, the simulation grid is nearly covered by large circular structures. A few spirals occur at places where the regular wavefront was distorted and break into a first generation of spirals.
- The final state is similar to that in the simulation where the states are natural numbers, $k_1 = 3$, and $k_2 = 3$, however, the waves are about 2 grid elements thicker.

Let us mention further key similarities between our simulation and actual experiments (Figs. 2b and 2c):

- The chemical waves do not interfere like material waves but merge.
- The chemical waves do not maintain the shape (as, e.g., solitons [13]).
- The morphology of interacting patterns (merger of patterns) in simulations has comparable traits as in real experiments.
- Quantitative features of the limit sets, i.e., the last evolutionary stage of the wave-spiral patterns can be set as close as possible to actual experimental data by an appropriate choice of the parameter range.

3.2 Influence of the noise

In Figure 3, we show a sketch of the research on the increase of neighborhood and internal kinds of excitation noise. Most cases gave a typical trajectory as shown in

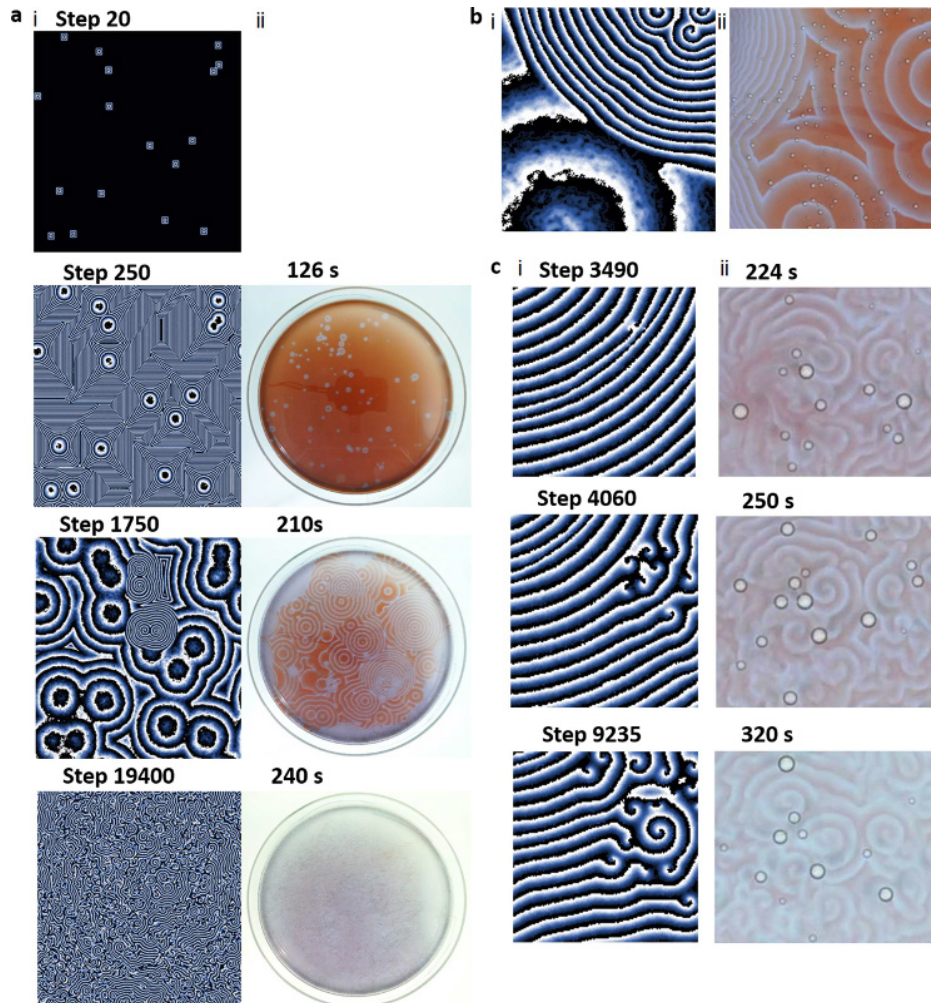


Fig. 2. Similarities between the trajectories of the simulation and of the BZR. (a) Selected states of the simulation (i) and corresponding images from the course of the experiment (ii). The early stage of the experiment corresponds to the lag phase of the experiment when no waves evolve. For the later stages of the simulation, corresponding structures were found in the experiment. (b) Sections of images which show wave merging. Similar behavior has not been found for material waves and another wavelike structures and indicates that threshold-range cellular automata (i) are proper models for phenomena observed in the BZR (ii). (c) States in formation of spirals. In the simulation (i), the distortion of the dense waves leads to their merging which is the source of formation of spirals. In the experiment (ii), the source of the distortion is often a bubble of carbon dioxide. Otherwise, the formation of spirals is similar to the experiment. For all processes, $g = 28$, $maxstate = 200$, $k_1 = 3$ and $k_2 = 3$. In the simulation, the black and white corresponds to 0 and $maxstate$, respectively.

Figure 1. Images in Figure 3 show sections of the 1600th step of the simulation, where the spiral-based structures prevail over the central circular target pattern. We observed some remnants of the circular structures followed by spirals and waves evolving around them. However, both central circular structures and systems of spirals and waves slightly differ. The exception occurred at neighborhood and internal excitation

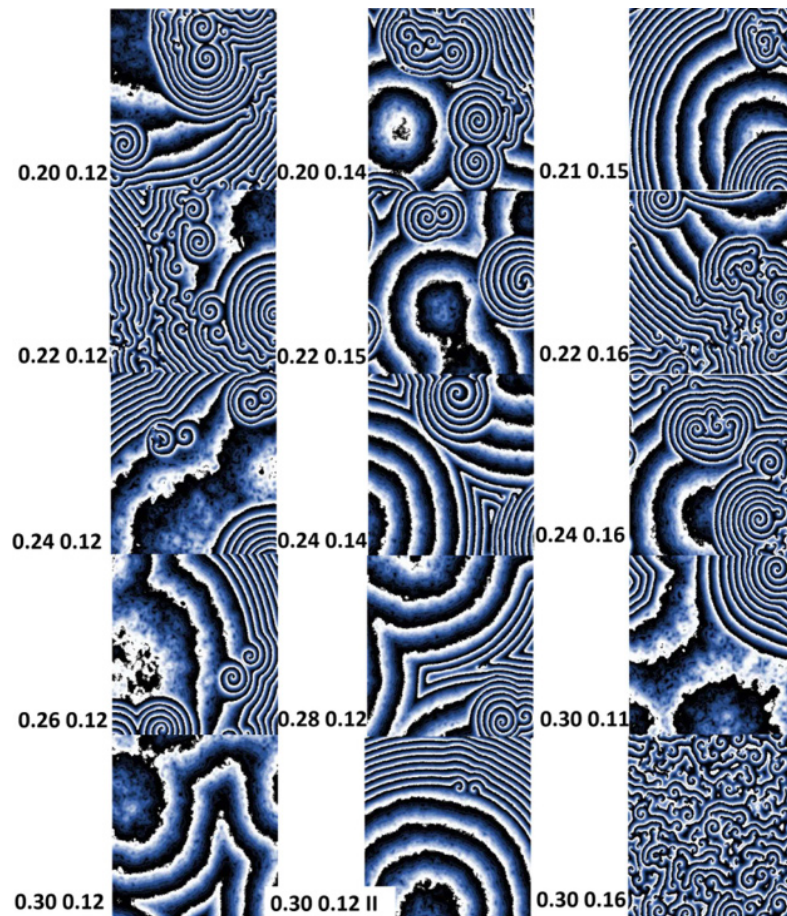


Fig. 3. Sections of steps 1600 of the simulations at different levels of external (the first number) and internal (the second number) excitation noise. The Roman numeral II (*bottom middle*) denotes the second experiment. Only at the internal and external (neighborhood) excitation noise of 30% and 12% (*bottom left*), respectively, mutual geometries of initial ignition points for which no spirals were formed were found. At any higher density of ignition points and different geometries, spirals were formed even at these combinations of noises.

noise of 30% and 12%, respectively (*bottom left* and *bottom middle*), where, in some cases, we did not observe any spirals. In contrast, the combination of neighborhood and internal excitation noise of 30% and 16% (*bottom right*) resulted in the fast evolution of spirals and waves which prevented the formation of circular waves.

3.3 Re-shaking experiment

Figure 4 shows the course of the experiment on the re-started BZR. The process (*cycle 1*) started by the evolution of circular waves. Each sub-experiment was stopped after reaching a phase of dense waves and the reaction vessel was re-shaken. This process was repeated 9 times. Upon re-shaking, the waves gradually lost regularity and became thicker, the diameters of target patterns increased (*cycle 3*) and the waves evolved mainly at the vessel's border (*cycle 4*). Similar phenomena were observed in a

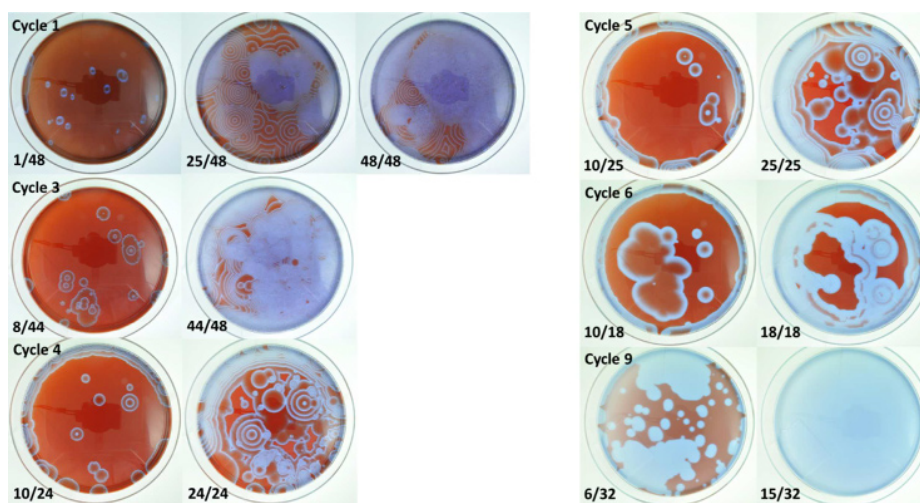


Fig. 4. Re-start of the B-Z reaction (9 cycles). The number ratio X/Y means the X th image from a Y -image series.

Petri dish of a smaller diameter. Further thickening of waves (*cycle 5*) led eventually to merging of circular waves (*cycle 6*) up to a complete filling of circular waves' centres (*cycle 9*). The next mixing did not lead to re-formation of the red-colored state.

In the early phase and, namely, upon gentle mixing (as shown in Fig. 1) the circular waves are highly regular. At later stages, upon re-shaking, the wavefronts became undulated and more similar to those observed in the NHM simulation. Finally, the waves thickened to the extent that the formation of structures was no more possible.

This experiment demonstrates that the depletion of reactants does not change the shape of observed waves and their course (order) but causes thickening of the traveling waves and shortens time to reaching the ergodic state. The ergodic state, both in the experiment and in the model, is characterized by a coexistence of spirals and waves.

3.4 Mesoscopicity and the size of the elementary spatial unit

When noise matters, an observed process is typically mesoscopic. It does follow neither the deterministic rules of the microscopic (or purely mechanical) system nor the statistical-physics tenet of Boltzmannian statistical physics that only the most frequent events are observed. The success of the simulation described in this article is based on the existence of the minimal spatial element to which all processes are referred. Indeed the simplest explanation is that the space is segregated into elementary units similar to those observed in viscous fluids at temperature gradients, i.e., to the Bénard cells [10]. With this hypothesis, we have examined the size of the elementary unit.

Figure 5 shows the analysis of wave profiles in the hodgepodge model. Figure 5a shows the influence of the $g/\text{maxstate}$ ratio on the final phase of the model in the noise-free and discrete system when no decimal numbers are allowed. The $g/\text{maxstate}$ ratio corresponds to the number of timesteps of the simulation at which the maximal excitation was achieved. The timestep may be also understood as a measure of the ratio between a "diffusive" process (the first term in Eq. (3)) and a zero-order chemical reaction (the second term in Eq. (3)) when the first term is always realized in one timestep. A low $g/\text{maxstate}$ ratio, i.e., a fast reaction process in comparison to the

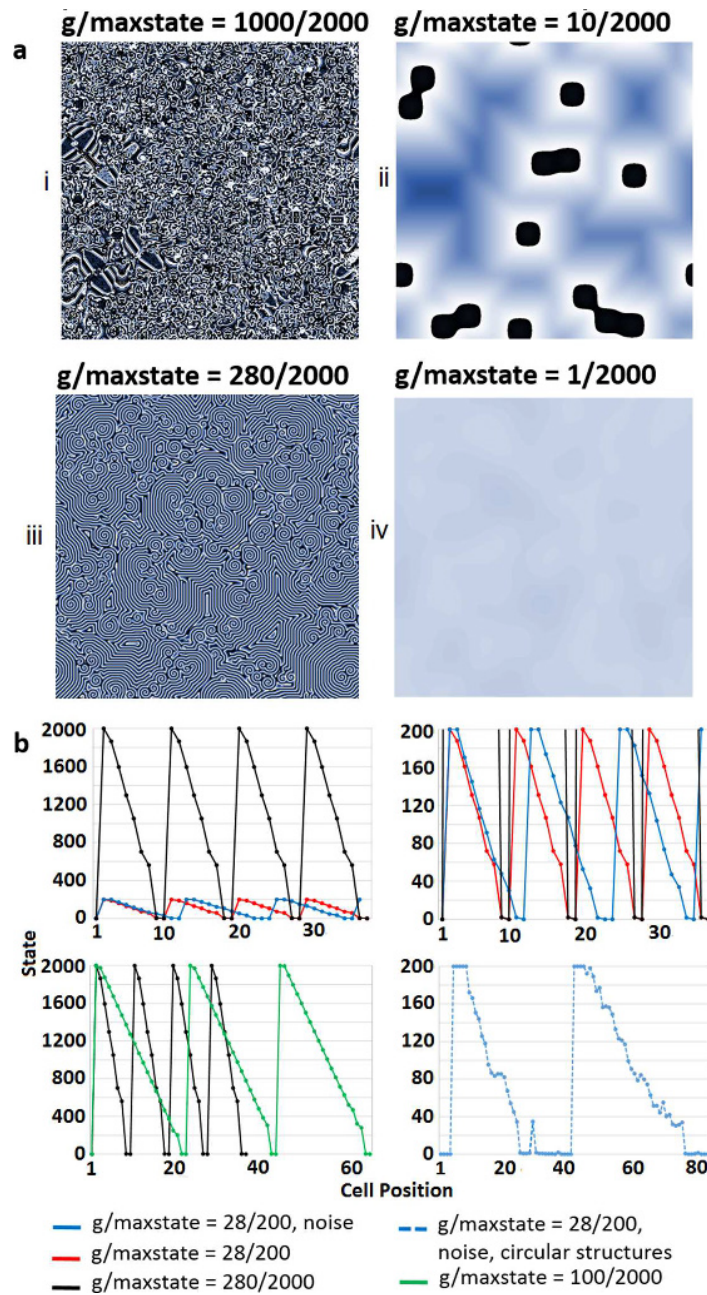


Fig. 5. Ratio of processes 2a and 2b determines the size of elementary unit and the type of state trajectory. (a) Images of later states of simulation at different $g/\text{maxstate}$ ratios, $k_1 = 3$, $k_2 = 3$ and $\text{noise} = 0$. At $g/\text{maxstate} = 1000/2000$ (i), spirals evolve into forms of ram's horns. To the opposite, $g/\text{maxstate} = 10/2000$ (ii) does not form spirals. At $g/\text{maxstate} = 1/2000$ (iv), the process is fully diffusive. At $g/\text{maxstate} = 280/2000$ (iii), the trajectory is almost identical to the experimental trajectory. (b) The intensity profiles of waves at different $g/\text{maxstate}$ ratios. Decrease of the $g/\text{maxstate}$ ratio leads to the broadening of waves. The intensity profile of the circular structure is very noisy. In the simulation, the black and white corresponds to 0 and maxstate , respectively.

diffusive one, leads to narrow waves and short spirals (e.g., Fig. 5a-iii). At a very low $g/maxstate$ ratio, waves do not fully develop and spirals do not arise (e.g., Fig. 5a-iv).

Figure 5b depicts several profiles of waves taken in the direction orthogonal to the wave development. As shown, the formation of wave in the system with and without the introduced noise, respectively, takes different times. In the noise-free processes (e.g., at the $g/maxstate$ of 28/200 and 280/2000, *upper*), the wave is fully formed in 10 steps, while, in the simulation when noise is induced (see $g/maxstate = 28/200$), the formation of the wave takes 13 steps. At $g/maxstate = 100/2000$ (*lower left*), the waves are as broad so that they do not fully separate. For comparison, Figure 5b includes the profile of the early circular wave (*lower right*).

The striking similarity of the simulation to real experiment intensity profiles of dense waves (Figs. 1, 5 and 6) motivated us to guess the number of molecules per an elementary spatial unit (i.e., the pixel of experimental wave). The number of elementary units per the width of the wave was in the range of 10–20. Since the average width of the wave was 1.5 mm, the elementary unit had 0.07–0.15 mm. The solution above the elementary unit had thickness and volume of 0.5 mm and 10^{-2} mm³, respectively. Then, the solution contained ca. 3×10^{13} and 10^{10} molecules of water and reactants per elementary unit, respectively. This number lies within the thermodynamic limit. The source of the mesoscopicity has to be sought in the physico-chemical dynamics. It means that only a few energetic/re-organizational events occur within a given time. Since an elementary spatial unit contains roughly 10^{10} molecules of reactants, it is likely that we are dealing with a phase separation which gives rise to structures of an analogous type as, e.g., in liquid crystals [13].

4 Conclusions

In the BZR, the target circular waves are always overcome by dense waves and spirals. Dense waves are typically evolving at the border of a Petri dish due to the non-idealities of the spatial geometry, while spirals evolve from the origin located at the center from micro-bubbles (again from a spatial inhomogeneities).

The re-shaken experiment excludes any simple chemical interpretation of the decay of observed structures. It is not the depletion of chemicals which leads to the transformation of circular waves – target patterns – to dense waves and, finally, to the mixture of spirals and dense waves. In the wide range of concentrations, when the thickness of waves is not broader than the diameter of the Petri dish, the general behavior of the BZR is qualitatively identical. The self-organization in the BZR is a process which is separated from a concrete chemical reaction. This fact justifies the search for a model of self-organization which would describe the reaction and ignore the actual chemical process.

In the numerical simulations presented in this article, it has been found that, at certain configurations of ignition points, there is a lower and upper limit of the noise at which the whole simulation grid is filled with circular structures – target patterns – and the spirals-waves phase never occurs. This happens when combination of neighborhood (external) excitation noise (*EEN*) is from 30% to 34% with the internal excitation noise (*IEN*) of 12%. The spatial inhomogeneity which lead to the evolution of spirals and waves at unfavorable conditions is not properly described by this model. However, at certain combinations of the geometry of ignition points, spirals are formed even in this case.

The spirals are formed also in the original hodgepodge machine. This can be observed in cases when the ignition constants k_1 and k_2 are bigger than 2. Our interpretation of this fact is that the multitude of possible realizations of the ignition points serves as a kind of noise. Thus, for the formation of spirals and waves, the noise is a necessary condition. This noise is in fact the phase transition noise (*PTN*)

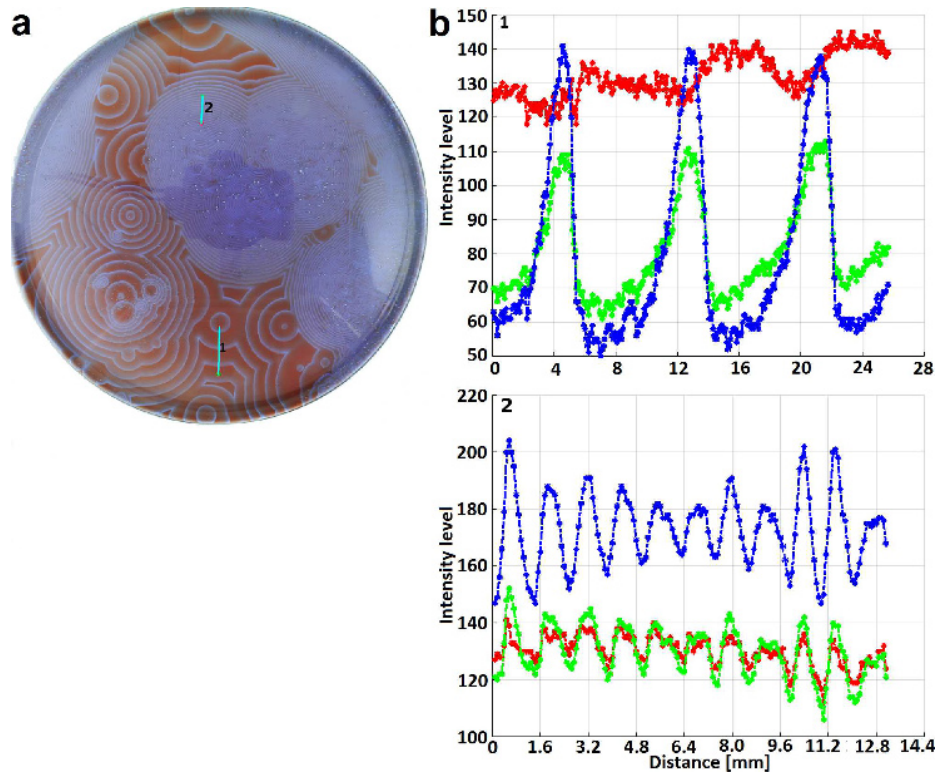


Fig. 6. Analysis of traveling waves in the Belousov–Zhabotinsky experiment. (a) Figure with identified wave profiles. (b) Intensity profile of the early circular wave (1) and later dense wave (2). Three colors represent camera channels.

but of a very specific spatial distribution. In our numerical simulations this *PTN* was mimicked by a combination of the proper *IEN* and *EEN*.

Differences in structures and dynamics shown in the re-shaking experiment (Fig. 4) – the undulation of circular waves, thickening, doubling of wavefront, etc. – indicate that there exist numerous individual processes which play a rôle in the formation of the patterns in the BZR. All these processes have rates comparable to the bottleneck process which determines the characteristic reaction time. Unfortunately, at present it does not exist experimental procedure for identification of these processes. We know a lot of chemicals but we do not know which breakage of individual chemical bond or diffusion constant corresponds to the bottleneck process. As described in [4], this is analogous to the thickening of the wave observed in the “noise-free” hodgepodge machine due to the decrease of the g/\maxstate ratio. Thus, the model has a potential to explain this aspect of the experiment as well.

We conclude that the noisy hodgepodge machine – NHM – is one of the simplest (if not the simplest) approximations to all natural processes occurring in a plane and leading to formation of coexistence of spirals and waves as well as to diffusive structures. It provides all basic stages observed in the experiment and indicates (and restricts) possible geometrical and kinetic rules. The ratio of two slowest processes close to 7:2 and the g/\maxstate value 1:7 lead to the best approximation of observed reality [4]. In the experiment, we observe the dominant “hodgepodge” process combined with a number of individual processes. The competing processes, occurring at

a slower but comparable rate, have the character of noise which may be even spatially non-isotropic. They are only roughly simulated by the white noise used in the NHM. Using the different kinds of noise, the circular waves are stabilized and several frequencies are observed.

In any case, the dynamical co-existence of spirals and dense waves is the ergodic state in all observed cases. It is clear that the ergodic state is not a state of chemical equilibrium. Even the homogeneously blue color observed at the end of the re-shaking experiment is not the chemical equilibrium state. It is still a dynamic state where the blue waves cannot be observed. The true chemical equilibrium occurs only when all Fe^{2+} ions are oxidized and precipitated in the form of iron(III) oxide.

In summary, this article supports the hypothesis that the BZR consists of an initial (lag) phase in which a regular grid of spatial cells is formed. Within this grid, the process of chemical “communication” occurs due to diffusion between these cells. Inside each of the cell develops a process whose chemical character may be, perhaps, described by one of the schemes developed for oscillating process in the mixed vessel.

The earlier observation of Garcia-Ojarvo and Schimansky-Geier [6] who showed that noise induces the formation of spirals in the FitzHugh-Nagumo model on a regular grid was at least qualitatively identical to our observation of spirals and waves at the late ergodic stage of the BZR. Possibly, the same mechanism of generation of spirals and waves may be applied to the whole class of similar real excitable media operating in “two-dimensional” conditions, e.g., in a sufficiently thin layer or in a living cell monolayer. The ergodic pattern in the final phase of the systems of the excitable media can be thus achieved either as a result of “noise” generated due to two or more non-zero cells in the vicinity of the ignition point, or by introduction of two different levels of flat (white) noise into “reaction” and “diffusion” element of the excitable medium, respectively, or by the application of the Gaussian noise to the resulted value. This fact that the same final ergodic state is achieved by three different way demonstrates that the coexistence of spiral and waves is a final state for a wide spectrum of noisy excitable media.

The stringent correspondence of the simulation on a discrete grid to the chemical experiment strongly supports the hypothesis on the formation of a grid of cells analogous to the Bénard cells in viscous liquid [10] or to elementary cells in liquid crystals [13]. This observation opens numerous new questions, namely, to which extent the continuous differential equations are appropriate tools for description of natural processes, at least those which lead to spirals or turbulences.

This work was supported by the Ministry of Education, Youth and Sports of the Czech Republic – projects CENAKVA (No. CZ.1.05/2.1.00/01.0024), CENAKVA II (No. LO1205 under the NPU I program), the CENAKVA Centre Development (No. CZ.1.05/2.1.00/19.0380) – and from the European Regional Development Fund in frame of the project Kompetenzzentrum MechanoBiologie (ATCZ133) in the Interreg V-A Austria – Czech Republic programme and by project GAJU 017/2016/Z. P.J. was supported by the GAČR Grant 17-33812. Authors thank to the anonymous reviewer for the comments which helped them to improve the interpretation of the results presented in the paper.

Author contribution statement

D.Š. designed the noisy hodgepodge machine model, performed the noisy hodgepodge machine simulations, analyzed their results and prepared the first draft of the paper. A.Z. performed and analyzed the chemical experiments on the Belousov-Zhabotinsky reaction. K.-M.Š. performed the hodgepodge machine simulations and classified the simulation results. R.R. developed the algorithms for analysis of experimental datasets, contributed to the theoretical discussions, coordinated manuscript

preparation, and edited its final version. P.J. masterminded the theoretical discussion and editing of the manuscript.

References

1. V.K. Vanag, *Physics–Uspekhi* **42**, 413 (1999)
2. M. Gerhardt, H. Schuster, J.J. Tyson, *Science* **30**, 1563 (1990)
3. S. Hiltmann, Multi-coloured cellular automata, Bachelor thesis, Erasmus Universiteit, Rotterdam, The Netherlands, 2008
4. D. Štys, T. Náhlík, A. Zhyrova, R. Rychtáriková, Š. Papáček, P. Císař, in *HPCSE 2015*, *Lect. Notes Comp. Sci.* **9611**, 171 (2016)
5. A.K. Dewdney, *Sci. Am.* **225**, 104 (1988)
6. J. García-Ojalvo, L. Schimansky-Geier, *Europhys. Lett.* **47**, 298 (1999)
7. R. FitzHugh, *Bull. Math. Biophys.* **17**, 257 (1955)
8. J. Nagumo, S. Arimoto, S. Yoshizawa, *Proc. IRE* **50**, 2061 (1962)
9. A. Wuensche, *Exploring discrete dynamics* (Luniver Press, 2011)
10. A.V. Getling, *Rayleigh–Bénard convection: structures and dynamics* (World Scientific, 1998)
11. J. Cohen, <http://drjackcohen.com/BZ01.html>
12. U. Wilensky, NetLogo B-Z Reaction model (Center for Connected Learning and Computer-Based Modeling, Northwestern University, Evanston, IL, 2003), <http://ccl.northwestern.edu/netlogo/models/B-ZReaction>
13. M. Blasone, P. Jizba, G. Vitiello, *Quantum field theory and its macroscopic manifestations. Boson condensation, ordered patterns and topological defects* (Imperial College Press, Cambridge, UK, 2011)

■ Point Divergence Gain and multidimensional data sequences analysis

R. Rychtáriková, J. Korbek, P. Macháček a D. Štys, *Point Divergence Gain and multidimensional data sequences analysis*, Entropy **20** (2018), 106.

V práci je odvozena nová statistická veličina *divergentní příspěvek bodu* (PDG, z angl. Point Divergence Gain) z Rényiho entropie, která byla původně zavedena v oblasti teorie informace jako parametrická relaxace Shannonovy (ve fyzikální chemii analogicky Boltzmannovy–Gibbovy) entropie. Metodu výpočtu PDG a návazně její entropie a hustoty entropie lze použít k citlivé analýze časoprostorových datových řad, například obrazových sérií. Tato práce navazuje na předchozí publikace popisující vlastnosti veličiny *informační příspěvek bodu* (PIG, z angl. Point Information Gain)

- **R. Rychtáriková**, J. Korbek, P. Macháček, P. Císař, J. Urban a D. Štys, *Point Information Gain and multidimensional data analysis*, Entropy **18** (2016), 372.
- **R. Rychtáriková**, *Clustering of multi-image sets using Rényi information entropy*, In: Ortuño a Rojas (Ed.) International Conference on Bioinformatics and Biomedical Engineering (IWBBIO) 2016, Part I, Lecture Notes in Computer Science **9656**, Springer, Switzerland (2016), pp. 517–526.

Article

Point Divergence Gain and Multidimensional Data Sequences Analysis

Renata Rychtáriková ^{1,*}, Jan Korbel ^{2,3,4}, Petr Macháček ¹ and Dalibor Štys ¹

¹ Institute of Complex Systems, South Bohemian Research Center of Aquaculture and Biodiversity of Hydrocenoses, Kompetenzzentrum MechanoBiologie in Regenerativer Medizin, Faculty of Fisheries and Protection of Waters, University of South Bohemia in České Budějovice, Zámek 136, 373 33 Nové Hradky, Czech Republic; info@imagecode.eu (P.M.); stys@frov.jcu.cz (D.Š.)

² Section for Science of Complex Systems, CeMSIS, Medical University of Vienna, Spitalgasse 23, 1090 Vienna, Austria; korbeja2@fjfi.cvut.cz

³ Complexity Science Hub Vienna, Josefstädter Strasse 39, 1080 Vienna, Austria

⁴ Faculty of Nuclear Sciences and Physical Engineering, Czech Technical University in Prague, Břehová 7, 115 19 Prague, Czech Republic

* Correspondence: rrychtarikova@frov.jcu.cz; Tel.: +420-387-773-833

Received: 27 December 2017; Accepted: 30 January 2018; Published: 3 February 2018

Abstract: We introduce novel information-entropic variables—a Point Divergence Gain ($\Omega_\alpha^{(l \rightarrow m)}$), a Point Divergence Gain Entropy (I_α), and a Point Divergence Gain Entropy Density (P_α)—which are derived from the Rényi entropy and describe spatio-temporal changes between two consecutive discrete multidimensional distributions. The behavior of $\Omega_\alpha^{(l \rightarrow m)}$ is simulated for typical distributions and, together with I_α and P_α , applied in analysis and characterization of series of multidimensional datasets of computer-based and real images.

Keywords: point divergence gain (PDG); Rényi entropy; data processing

1. Introduction

Extracting the information from raw data obtained from, e.g., a set of experiments, is a challenging task. Quantifying the information gained by a single point of a time series, a pixel in an image, or a single measurement is important in understanding which points bring the most information about the underlying system. This task is especially delicate in case of time-series and image processing because the information is not only stored in the elements, but also in the interactions between successive points in a time series. Similar, when extracting information from an image, not all pixels have the same information content. This type of information is sometimes called local information because the information depends not only on the frequency of the phenomenon but also on the position of the element in the structure. The most important task is to identify the sources of information and to quantify them. Naturally, it is possible to use standard data-processing techniques based on quantities from information theory like, e.g., Kullback–Leibler divergence. On the other hand, the mathematical rigorousness is typically compensated by an increased computational complexity. For this end, a simple quantity called Point Information Gain and its relative macroscopic variables—a Point Information Gain Entropy and a Point Information Gain Entropy Density—were introduced in [1]. In [2], mathematical properties of the Point Information Gain were extensively discussed and applications to real-image data processing were pointed out. From the mathematical point of view, the Point Information Gain represents a change of information after removing an element of a particular phenomena from a distribution. The method is based on the Rényi entropy, which has been already extensively used in multifractal analysis and data processing (see e.g., Refs. [2–5] and references therein).

In this article, we introduce an analogous variable to the Point Information Gain. This new variable locally determines an information change after an exchange of a given element in a discrete set. We use a simple concept of entropy difference between the original set and the set with the exchanged element. The resulting value is called Point Divergence Gain $\Omega_\alpha^{(l \rightarrow m)}$ [6,7]. The main idea is to describe the importance of changes in the series of images (typically representing a video record from an experiment) and extract the most important information from it. Similar to the Point Information Gain Entropy and the Point Information Gain Entropy Density, the macroscopic variables called a Point Divergence Gain Entropy I_α and a Point Divergence Gain Entropy Density P_α are defined to characterize subsequent changes in a multidimensional discrete distribution by one number. The goal of this article is to examine and demonstrate some properties of these variables and use them for examination of time-spatial changes of information in sets of discrete multidimensional data, namely series of images in image processing and analysis, after the exchange of a pixel of a particular intensity for a pixel at the same position in the consecutive image. The main reason for choosing the Point Divergence Gain as the relevant quantity for the analysis of spatio-temporal changes is the fact that it represents an information gain of each pixel change. One can also consider model-based approaches based on the theory of random-fields, which can be more predictive in some cases. On the other hand, the model-free approach based on entropy gives us typically more relevant information for real data, where it is typically difficult to find an appropriate model. For the overview of model-based approaches in the random field theory, one can consult, e.g., Refs. [8–10].

The paper is organized as follows: in Section 2, we define the main quantity of the paper, i.e., the Point Divergence Gain and the related quantities and discuss its theoretical properties. In Section 3, we show applications of the Point Divergence Gain to image processing for both computer-based and real sequences of images. We show that the Point Divergence Gain can be used as a measure of difference for clustering methods and detects the most prominent behaviour of a system. In Section 4, we explain the presented methods and finer technical details necessary for the analysis including algorithms. Section 5 is dedicated to conclusions. All image data, scripts for histogram processing, and Image Info Extractor Professional software for image processing are available via [sftp://160.217.215.193:13332/pdg](https://160.217.215.193:13332/pdg) (user: anonymous; password: anonymous.).

2. Basic Properties of Point Divergence Gain and Derived Quantities

2.1. Point Divergence Gain

Recently, a quantity called Point Information Gain (PIG, $\Gamma_\alpha^{(i)}$) [6,7] and its generalization based on the Rényi entropy [2] have been introduced. We show how to apply the concept of PIG to sequence of multidimensional data frames.

Let us assume a set of variables with k possible outcomes (e.g., possible colours of each pixel). The $\Gamma_\alpha^{(i)}$ is a simple variable based on entropy difference and enables us to quantify an information gain of each phenomenon. It is simply defined as a difference between entropy of an original discrete distribution

$$P = \{p_j\}_{j=1}^k = \left\{ \frac{n_1}{n}, \dots, \frac{n_k}{n} \right\}, \quad (1)$$

which typically describes a frequency histogram of possible outcomes. Let us also define a distribution, where one occurrence of the i -th phenomenon is omitted, i.e.,

$$P^{(i)} = \left\{ p_j^{(i)} \right\}_{j=1}^k = \left\{ \frac{n_1}{n-1}, \dots, \frac{n_i-1}{n-1}, \dots, \frac{n_k}{n-1} \right\}. \quad (2)$$

Thus, the Point Information Gain is defined as

$$\Gamma_\alpha^{(i)} \equiv \Gamma_\alpha^{(i)}(P) = \mathcal{H}_\alpha(P^{(i)}) - \mathcal{H}_\alpha(P), \quad (3)$$

where \mathcal{H}_α is the Rényi entropy (Despite all computer implementations being calculated as \log_2 , the following derivations are written in natural logarithm, i.e., \ln .)

$$\mathcal{H}_\alpha(P) = \frac{1}{\alpha - 1} \ln \sum_i p_i^\alpha. \tag{4}$$

The Rényi entropy represents a one-parametric class of information quantities tightly related to multifractal dynamics and enables us to focus on certain parts of the distribution [11]. Unlike the typically used Rényi’s relative entropy [3,4,11–17], the Point Information Gain $\Gamma_\alpha^{(i)}$ is a simple, computationally tractable quantity. Its mathematical properties have been extensively discussed in [2]. On the same basis, we can define a Point Divergence Gain (PDG, $\Omega_\alpha^{(l \rightarrow m)}$), where a discrete distribution $P^{(i)}$ is replaced by a distribution

$$P^{(l \rightarrow m)} = \left\{ p_j^{(l \rightarrow m)} \right\}_{j=1}^k = \left\{ \frac{n_1}{n}, \dots, \frac{n_l - 1}{n}, \dots, \frac{n_m + 1}{n}, \dots, \frac{n_k}{n} \right\}, \tag{5}$$

which can be obtained from the original distribution P , where the occurrence of the examined l -th phenomenon ($n_l \in \mathbb{N}^+$) is removed and supplied by a point of the occurrence of the m -th phenomenon ($n_m \in \mathbb{N}_0$). The main idea behind the definition is to quantify the information change in the subsequent image, if only one point is changed. Analogous to the Point Information Gain $\Gamma_\alpha^{(i)}$, the Point Divergence Gain can be defined as

$$\Omega_\alpha^{(l \rightarrow m)} \equiv \Omega_\alpha^{(l \rightarrow m)}(P) = \mathcal{H}_\alpha(P^{(l \rightarrow m)}) - \mathcal{H}_\alpha(P). \tag{6}$$

Let us first show its connection to the Point Information Gain $\Gamma_\alpha^{(i)}$. Since $P^{(l)} = P^{(l \rightarrow m, m)}$, it is possible to express the Point Divergence Gain as

$$\Omega_\alpha^{(l \rightarrow m)}(P) = \mathcal{H}_\alpha(P^{(l \rightarrow m)}) - \mathcal{H}_\alpha(P^{(l \rightarrow m, m)}) + \mathcal{H}_\alpha(P^{(l)}) - \mathcal{H}_\alpha(P) = \Gamma_\alpha^{(l)}(P) - \Gamma_\alpha^{(m)}(P^{(l \rightarrow m)}). \tag{7}$$

Let us investigate mathematical properties of the PDG. The $\Omega_\alpha^{(l \rightarrow m)}$ can be rewritten as

$$\begin{aligned} \Omega_\alpha^{(l \rightarrow m)} &= \mathcal{H}_\alpha(P^{(l \rightarrow m)}) - \mathcal{H}_\alpha(P) \\ &= \frac{1}{1 - \alpha} \ln \left(\sum_{j=1}^k (p_j^{(l \rightarrow m)})^\alpha \right) - \frac{1}{1 - \alpha} \ln \left(\sum_{j=1}^k p_j^\alpha \right) = \frac{1}{1 - \alpha} \ln \left(\frac{\sum_{j=1}^k (p_j^{(l \rightarrow m)})^\alpha}{\sum_{j=1}^k p_j^\alpha} \right). \end{aligned} \tag{8}$$

By plugging the relative frequencies from Equations (1) and (5) into Equation (8), we obtain

$$\begin{aligned} \Omega_\alpha^{(l \rightarrow m)} &= \frac{1}{1 - \alpha} \ln \left[\frac{(n_l - 1)^\alpha + (n_m + 1)^\alpha + \sum_{j=1, j \neq l, m}^k n_j^\alpha}{\sum_{j=1}^k n_j^\alpha} \right] \\ &= \frac{1}{1 - \alpha} \ln \left[\frac{(n_l - 1)^\alpha + (n_m + 1)^\alpha + \sum_{j=1}^k n_j^\alpha - n_l^\alpha - n_m^\alpha}{\sum_{j=1}^k n_j^\alpha} \right] \\ &= \frac{1}{1 - \alpha} \ln \left[\frac{(n_l - 1)^\alpha - n_l^\alpha + (n_m + 1)^\alpha - n_m^\alpha}{\sum_{j=1}^k n_j^\alpha} + 1 \right]. \end{aligned} \tag{9}$$

As seen in Equation (9), the variable $\Omega_\alpha^{(l \rightarrow m)}$ does not depend (contrary to the $\Gamma_\alpha^{(i)}$) on n but depends only on the number of elements of each phenomenon j . In Equation (9), let us design the nominator $\sum_{j=1}^k n_j^\alpha$, which is constant and related to the original distribution (histogram) of elements and to the parameter α , as \mathcal{C}_α . It gives us the final form

$$\Omega_{\alpha}^{(l \rightarrow m)} = \frac{1}{1 - \alpha} \ln \left[\frac{(n_l - 1)^{\alpha} - n_l^{\alpha} + (n_m + 1)^{\alpha} - n_m^{\alpha}}{C_{\alpha}} + 1 \right]. \quad (10)$$

Equation (10) demonstrates that, for a particular distribution, $\Omega_{\alpha}^{(l \rightarrow m)}$ is a function only of the parameter α and frequencies of occurrences of the phenomena n_l and n_m in the original distribution, between which the exchange of the element occurs. Equation (10) further shows that if the exchange of the element occurs between phenomena l and m of the same (similar) frequencies of occurrence (i.e., $n_l \approx n_m$), the value of $\Omega_{\alpha}^{(l \rightarrow m)}$ equals 0. If we remove a rare point and supply it by a high-frequency point (i.e., $n_l \ll n_m$), the value of $\Omega_{\alpha}^{(l \rightarrow m)}$ is negative, and *vice versa*. Low values of parameter α separate low-frequency events as $\Omega_{\alpha}^{(l \rightarrow m)} = 0$, whereas high α emphasize high-frequency events as $\Omega_{\alpha}^{(l \rightarrow m)} \gg 0$ or $\Omega_{\alpha}^{(l \rightarrow m)} \ll 0$ and merge rare events into $\Omega_{\alpha}^{(l \rightarrow m)} = 0$. With respect to the previous discussion and practical utilization of this notion, we emphasize that, for real systems with large n , the $\Omega_{\alpha}^{(l \rightarrow m)}$ are rather small numbers.

In the 3D plots of Figure 1, we demonstrate $\Omega_{\alpha}^{(l \rightarrow m)}$ -transformations of four thoroughly studied distributions—the Cauchy, Gauss (symmetrical), Lévy, and Rayleigh distribution (asymmetric; all specified in Section 4.1)—for $\alpha = \{0.5; 1.0; 2.0; 4.0\}$, where each point presents the exchange of the element between bins l and m (Algorithm 1). In this case, the (a)symmetry of the distribution is always maintained.

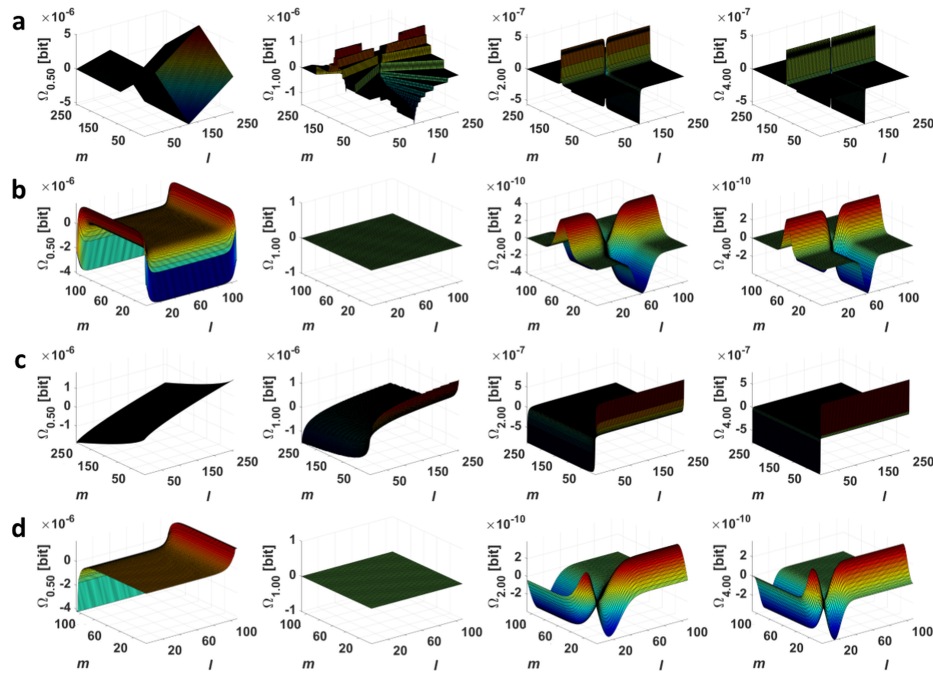


Figure 1. The Ω_{α} -transformations of the discrete (a) Cauchy; (b) Gauss; (c) Lévy; and (d) Rayleigh distribution for $\alpha = \{0.5; 1.0; 2.0; 4.0\}$ (Section 4.1).

Algorithm 1: Calculation of a point divergence gain matrix (Ω_α) for typical histograms.

```

Input:  $n$ -bin histogram  $\mathbf{h}$ ;  $\alpha$ , where  $\alpha \geq 0 \wedge \alpha \neq 1$ 
Output:  $\Omega_\alpha$ 

1  $\Omega_\alpha = \text{zeros}(n, n);$  % create a zero square matrix  $\Omega_\alpha$  of the size of  $n \times n$ 
2  $C_\alpha = \text{sum}(\mathbf{h}^\alpha);$  % calculate the constant  $C_\alpha$  for the given distribution and  $\alpha$ 

3 for  $l = 1$  to  $n$  do
4     if  $\mathbf{h}(l) \neq 0$  then
5         for  $l = 1$  to  $n$  do
6              $\Omega_\alpha(l, m) =$ 
7                  $\log_2(((\mathbf{h}(l) - 1)^\alpha - \mathbf{h}(l)^\alpha + (\mathbf{h}(m) + 1)^\alpha - \mathbf{h}(m)^\alpha) / C_\alpha + 1) / (1 - \alpha));$ 
8             end
9         else
10             $\Omega_\alpha(l, :) = \text{NaN};$ 
11        end
12    end
    % if the bin  $l$  of the histogram  $\mathbf{h}$  is occupied, calculate  $\Omega_\alpha$  at each position  $(l, m)$  according to
    Equation (10), else set the not-a-number into the row  $l$  of the  $\Omega_\alpha$  matrix

```

Now we will consider the specific case $\alpha = 2$ (collision entropy) for which Equation (10) can be simplified to

$$\Omega_2^{(l \rightarrow m)} = -\ln \left[\frac{2}{C_2} (n_m - n_l + 1) + 1 \right] = -\ln \left[\frac{2}{C_2} (\Delta n^{(l \rightarrow m)} + 1) + 1 \right]. \tag{11}$$

For a specific difference $\Delta n^{(x \rightarrow y)} = D$, Equation (11) can be approximated by the 1st-order Taylor sequence

$$\begin{aligned} \Omega_2^{(l \rightarrow m)} &\approx -\ln \left[\frac{2}{C_2} (D + 1) + 1 \right] - \frac{2}{2(D + 1) + C_2} (\Delta n^{(l \rightarrow m)} - D) \\ &= -\frac{2}{2D + 2 + C_2} \Delta n^{(l \rightarrow m)} + \frac{2D}{2D + 2 + C_2} - \ln \left[\frac{2D}{C_2} + C_2 + 1 \right]. \end{aligned} \tag{12}$$

Equations (11) and (12) show that, for each unique $\Delta n^{(x \rightarrow y)}$, the $\Omega_2^{(l \rightarrow m)}$ depends only on the difference between the bins l and m , which the exchange of the element occurs between, and this dependence is almost linear. In other words, this explains why, for all distributions in Figure 2, the dependencies $\Omega_2^{(l \rightarrow m)} = f(n_m, n_m - n_l)$ are planes.

For $\alpha \rightarrow 1$, the Rényi entropy becomes the ordinary Shannon entropy [18] and we obtain (cf. Equation (4))

$$\mathcal{H}_1(P) = -\sum_{j=1}^k p_j \ln p_j = -\sum_{j=1}^k \frac{n_j}{n} \ln \frac{n_j}{n} = -\sum_{j=1, j \neq l, m}^k \frac{n_j}{n} \ln \frac{n_j}{n} - \frac{n_m}{n} \ln \frac{n_m}{n} - \frac{n_l}{n} \ln \frac{n_l}{n} \tag{13}$$

and

$$\mathcal{H}_1(P^{(l \rightarrow m)}) = -\frac{n_m + 1}{n} \ln \frac{n_m + 1}{n} - \frac{n_l - 1}{n} \ln \frac{n_l - 1}{n} - \sum_{j=1, j \neq l, m}^k \frac{n_j}{n} \ln \frac{n_j}{n}. \tag{14}$$

The difference of these entropies (cf. Equation (9)) is gradually giving

$$\begin{aligned}
 \Omega_1^{(l \rightarrow m)} &= -\frac{n_m+1}{n} \ln \frac{n_m+1}{n} - \frac{n_l-1}{n} \ln \frac{n_l-1}{n} + \frac{n_m}{n} \ln \frac{n_m}{n} + \frac{n_l}{n} \ln \frac{n_l}{n} \\
 &= -\frac{n_m+1}{n} \ln(n_m+1) + \frac{n_m+1}{n} \ln n - \frac{n_l-1}{n} \ln(n_l-1) + \frac{n_l-1}{n} \ln n + \frac{n_m}{n} \ln n_m \\
 &\quad - \frac{n_m}{n} \ln n + \frac{n_l}{n} \ln n_l - \frac{n_l}{n} \ln n \\
 &= \underbrace{\left(\frac{n_m+1}{n} + \frac{n_l-1}{n} - \frac{n_m}{n} - \frac{n_l}{n} \right)}_{=0} \ln n - \frac{n_m}{n} \ln(n_m+1) - \frac{1}{n} \ln(n_m+1) - \frac{n_l}{n} \ln(n_l-1) \\
 &\quad + \frac{1}{n} \ln(n_l-1) + \frac{n_m}{n} \ln n_m + \frac{n_l}{n} \ln n_l \\
 &= \frac{1}{n} \left(n_m \ln \frac{n_m}{n_m+1} + n_l \ln \frac{n_l}{n_l-1} + n \ln \frac{n_l-1}{n_m+1} \right). \tag{15}
 \end{aligned}$$

One can see that relation (15) is defined for $n_l \in \mathbb{N} \setminus \{0, 1\}$ and $n_m \in \mathbb{N}^+$ and is approximately equal to 0 for $n_l, n_m \gg 0$ (the Cauchy and Rayleigh distribution for $\alpha = 1$ in Figure 3).

For $n_l \in \mathbb{N}^+$ and $n_m \in \mathbb{N}_0$, from Equation (10), further implies:

1. If $\alpha = 0$, then $\Omega_0^{(l \rightarrow m)} = 0$.
2. If $\alpha \rightarrow \infty$, then $\Omega_\infty^{(l \rightarrow m)} \rightarrow 0$.

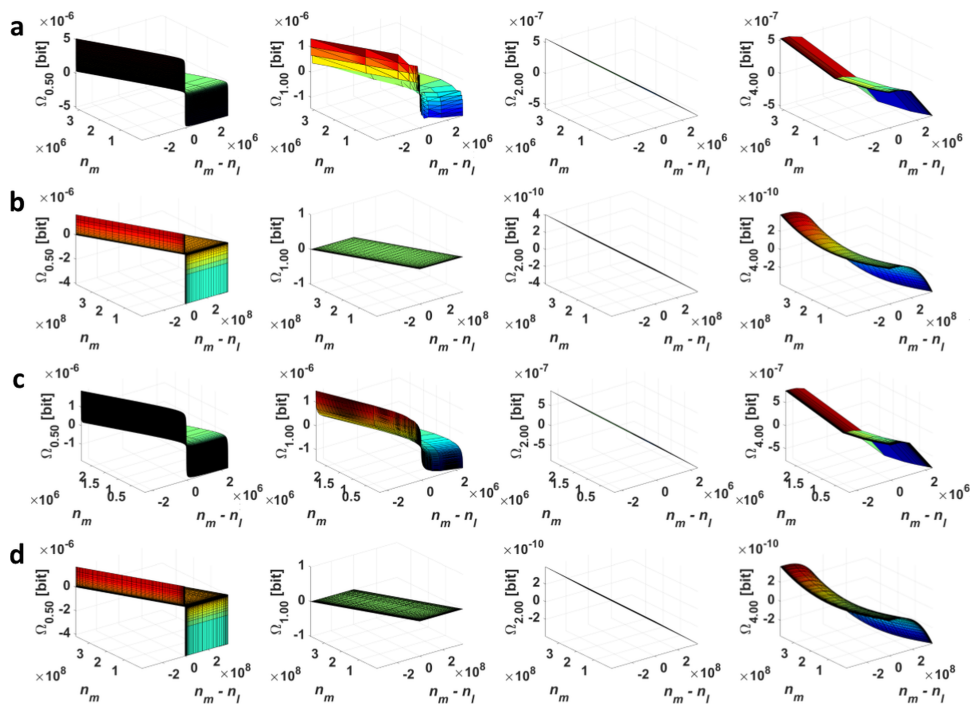


Figure 2. The dependencies $\Omega_\alpha = f(n_m, n_m - n_l)$ for the discrete (a) Cauchy; (b) Gauss; (c) Lévy; and (d) Rayleigh distribution at $\alpha = \{0.5; 1.0; 2.0; 4.0\}$ (Section 4.1).

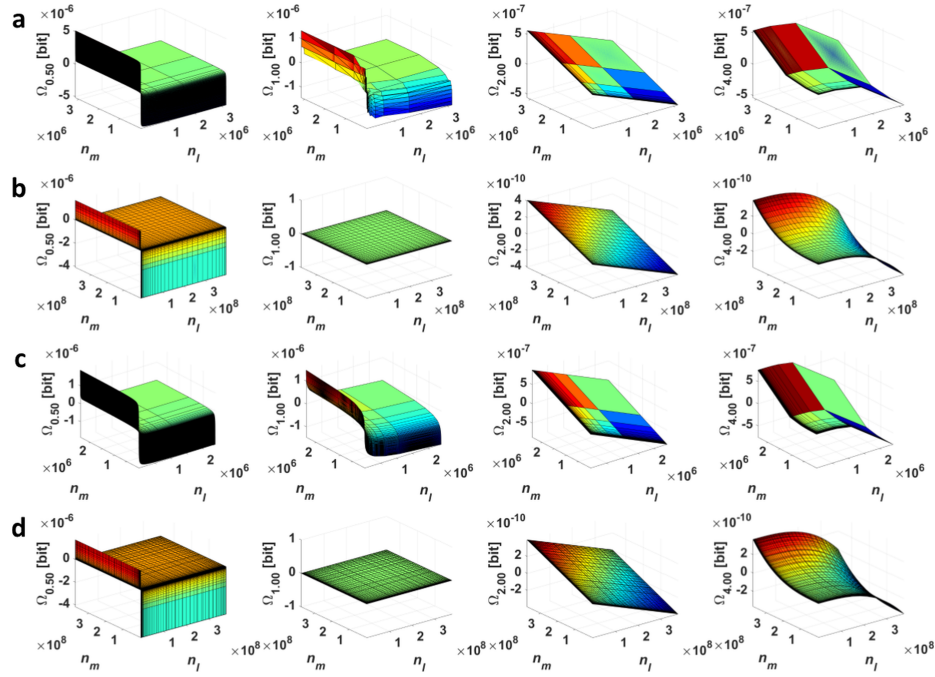


Figure 3. The dependencies $\Omega_\alpha = f(n_l, n_m)$ for the discrete (a) Cauchy; (b) Gauss; (c) Lévy; and (d) Rayleigh distribution at $\alpha = \{0.5; 1.0; 2.0; 4.0\}$ (Section 4.1).

2.2. Point Divergence Gain Entropy and Point Divergence Gain Entropy Density

In this section, we introduce two new variables that help us to investigate changes between two (typically consecutive) points of time series. A typical example can be provided by video processing, where each element of a time or spatial series is represented by a frame. Let us have two data frames $\mathcal{I}_a = \{a_1, \dots, a_n\}$ and $\mathcal{I}_b = \{b_1, \dots, b_n\}$ (For simplicity, we use only one index which corresponds to a one-dimensional frame. In case of images, we have typically two-dimensional frames and the elements are described by two indexes, e.g., x and y positions.). At each position $i \in \{1, \dots, n\}$, it is possible to replace the value a_i by the value of the following frame, i.e., b_i . The resulting $\Omega_\alpha^{(a_i \rightarrow b_i)}$ then quantifies how much information is gained/lost, when, at the i -th position, we replace the value a_i for the value b_i . A Point Divergence Gain Entropy (PDGE, I_α) is defined as a sum of absolute values of all PDGs for all pixels, i.e.,

$$I_\alpha(\mathcal{I}_a; \mathcal{I}_b) = \sum_{i=1}^n |\Omega_\alpha^{(a_i \rightarrow b_i)}| = \sum_{l=1}^k \sum_{m=1}^k n_{lm} |\Omega_\alpha^{(l \rightarrow m)}|, \tag{16}$$

where n_{lm} denotes the number of present substitutions $l \rightarrow m$, when we transform $\mathcal{I}_a \rightarrow \mathcal{I}_b$. The absolute value ensures that the contribution of the transformation of a rare point to a frequent point (negative Ω_α) and a frequent point to a rare point (positive Ω_α) do not cancel each other and both contribute to the resulting PDGE. Typically, appearance or disappearance of a rare point (and replacement by a frequent value—typically background colour) carries important information about the experiment. The PDGE can be understood as an absolute information change.

Moreover, it is possible to introduce other macroscopic quantity—a Point Divergence Gain Entropy Density (PDGED, P_α), where we do not sum over all pixels, but only over all realized transitions $l \rightarrow m$. Thus, the PDGED can be defined as

$$P_\alpha(\mathcal{I}_a; \mathcal{I}_b) = \sum_{l=1}^k \sum_{m=1}^k \chi_{lm} |\Omega_\alpha^{(l \rightarrow m)}|, \quad (17)$$

where

$$\chi_{lm} = \begin{cases} 1, & n_{lm} \geq 1, \\ 0, & n_{lm} = 0. \end{cases} \quad (18)$$

Let us emphasize that two transitions $a_1 \rightarrow b_1$ and $a_2 \rightarrow b_2$, where the frequencies of the occurrences of the phenomena a_1 and a_2 are equal and of the phenomena b_1 and b_2 are equal as well, give two unique values of the $\Omega_\alpha^{(a_i \rightarrow b_i)}$. In the computation of the PDGED, this is arranged by a hash function (Algorithm 2). We can understand the quantity PDGED as an absolute information change of all realized transitions of phenomena $m \rightarrow l$.

Algorithm 2: Calculation of a point information gain matrix (Ω_α) and values P_α and I_α for two consecutive images of a time-spatial series.

Input: 2 consecutive images \mathbf{I}_1 and \mathbf{I}_2 of the size $m \times n$; α , where $\alpha \geq 0 \wedge \alpha \neq 1$

Output: Ω_α

```

1 h = hist( $\mathbf{I}_1$ );      % create an intensity histogram h of the image  $\mathbf{I}_1$ 
2  $C_\alpha$  = sum(h. $^{\wedge}\alpha$ ); % calculate the constant  $C_\alpha$  for the given distribution and  $\alpha$ 
3  $\Omega_\alpha$  =  $\mathbf{I}_1$ . * 0; % create a zero matrix  $\Omega_\alpha$  of the size of the  $\mathbf{I}_1$ 
4 hashMap = containers.Map; % declare an empty hash-map (the key-value array)

5 for  $i = 1$  to ( $m \times n$ ) do
6    $\Omega_\alpha(i) = \log_2(((\mathbf{h}(\mathbf{I}_1(i+1)) - 1)^{\wedge}\alpha - \mathbf{h}(\mathbf{I}_1(i+1))^{\wedge}\alpha + (\mathbf{h}(\mathbf{I}_2(i+1)))^{\wedge}\alpha -$ 
7      $\mathbf{h}(\mathbf{I}_2(i+1))^{\wedge}\alpha) / C_\alpha + 1) / (1 - \alpha);$ 
8     % for each element  $i$  of the image  $\mathbf{I}_1$ , calculate a value  $\Omega_\alpha$  after replacement of the intensity
9     at the position  $i$  in the histogram of image  $\mathbf{I}_1$  by the intensity at the same position in the
10    image  $\mathbf{I}_2$  (Equation (10))
11
12     $v = \mathbf{I}(i);$  % read a value of the element (intensity) at the position  $i$ 
13     $checksum = \text{calcChecksum}(\mathbf{h}, v);$ 
14    % calculate checksum using a hash-function effective enough (e.g., MD4, MD5, SHA1)
15
16    if not hashMap.isKey(checksum) then
17      hashMap(checksum) =  $\Omega_\alpha(i);$ 
18      % if the hash-map does not contain the key, insert a new element with the key
19      checksum, where the inserted value is the  $\Omega_\alpha$  at the position  $i$ 
20    end
21  end
22
23  $I_\alpha = \text{sum}(\text{sum}(\text{abs}(\Omega_\alpha)));$ 
24 % calculate  $I_\alpha$  as a sum of all elements in the matrix  $\Omega_\alpha$  (Equation (16))
25  $P_\alpha = \text{sum}(\text{abs}(\text{values}(\mathbf{hashMap})));$ 
26 % calculate  $P_\alpha$  as a sum of all elements in the matrix hashMap (Equation (17))

```

If the aim is to assess the influence of elements of a high occurrence on the time-spatial changes in the image series, it is recommended to use PDGE where each element is weighted by its number of occurrences. If the aim is to suppress the influence of these extreme values, it is better to compute PDGED.

Let us consider a time-series \mathcal{V} , where each time step contains one frame, so $\mathcal{V} = \{\mathcal{I}_1, \mathcal{I}_2, \dots\}$. The series \mathcal{V} can be, e.g., a sequence of images (a video) obtained from some experiment, etc. For each time step, it is possible to calculate $I_\alpha(t) = I_\alpha(\mathcal{I}_t; \mathcal{I}_{t+s})$, resp. $P_\alpha(t) = P_\alpha(\mathcal{I}_t; \mathcal{I}_{t+s})$, where s is the time lag. Typically, we assume $s = 1$, i.e., consecutive frames with a constant time step.

3. Application of Point Divergence Gain and Its Entropies in Image Processing

The generalized Point Divergence Gain $\Omega_\alpha^{(l \rightarrow m)}$ in Equation (10) was originally used for characterization of dynamic changes in image series, namely in z-stacks of raw RGB data of unmodified live cells obtained via scanning along the z-axis using video-enhanced digital bright-field transmission microscopy [6,7]. In these two references, this new mathematical approach utilizes 8- and 12-bit intensity histograms of two consecutive images for pixel-by-pixel intensity weighted (parameterized) subtraction of these images to suppress the camera-based noise and to enhance the image contrast (In case of calibrated digital camera-based images, where the value of each point of the image reflects a number of incident photons, or, in case of computer-based images, it can be sufficient to use a simple subtraction for evaluation of time-spatial changes in the image series.).

For this paper, we chose other (grayscale) digital image series (Table 1) in order to demonstrate other applications of the PDG mathematical approach in image processing and analysis. Moreover, we newly introduce applications of the additive macroscopic variables Point Divergence Gain Entropy I_α and Point Divergence Gain Entropy Density P_α .

Table 1. Specifications of image series.

Series	Source	Bit-Depth	Number of Img.	Resolution	Origin
Toy Vehicle	[19]	8-bit	10	512 × 512	camera
Walter Cronkite	[19]	8-bit	16	256 × 256	camera
Simulated BZ	[20–22]	8-bit	10,521	1001 × 1001	computer-based ^a
Ring-fluorescence		12-bit	1058	548 × 720	experimental ^b
Ring-diffraction		8-bit ^c	1242	252 × 280	experimental ^b

^a A set of a noisy hotch-potch machine simulation of the Belousov–Zhabotinsky reaction [20–22] at 200 achievable states with the internal excitation of 10, and phase transition, internal excitation, and external neighbourhood kind of noise of 0, 0.25, and 0.15, respectively. ^b The microscopic series of a 6- μm standard microring (FocalCheck™, cat. No. F36909, Life Technologies™ (Eugene, OR, USA)) were acquired using the CellObserver microscope (Zeiss, Oberkochen, Germany) at the EMBL (Heidelberg, Germany). For both light processes, the green region of the visible spectrum was selected using an emission and transmission optical filter, respectively. In case of the diffraction, the point spread function was separated and the background intensities was disposed using Algorithm 1 in [7]. ^c The 12-bit depth was reduced using a Least Information Lost algorithm [23], which, by shifting the intensity bins, filled all empty bins in the histogram obtained from the whole data series up and rescaled these intensities between their minimal and maximal value.

3.1. Image Origin and Specification

Owing to the relation of the $\Omega_\alpha^{(l \rightarrow m)}$ to the Rényi entropy, the I_α and P_α as macroscopic variables can determine a fractal origin of images by plotting $I_\alpha = f_I(\alpha)$ and $P_\alpha = f_P(\alpha)$ spectra. If we deal with an image multifractality, the dependency $I_\alpha = f_I(\alpha)$ or the dependency $P_\alpha = f_P(\alpha)$ shows a peak. In case of a unifractality, these dependences are monotonous. It is demonstrated in Figures 4 and 5. There can be no doubts that the origin of the simulated Belousov–Zhabotinsky reaction (Figure 4) is multifractal. This statement is further strengthened by the courses of the dependencies $I_\alpha = f_I(\alpha)$ and $P_\alpha = f_P(\alpha)$, where we can see peaks with maxima at $\alpha \in (1, 2)$. On the contrary, a pair of images in Figure 5 (moving toys of cars) is a mixture of different fractal origin. In this case, whereas the course of $f_I(\alpha)$ is monotonous and thus shows a unifractal characteristics, the dependence

$f_P(\alpha)$ has a maximum at $\alpha = 0.6$ and thus demonstrates some multifractal features in the image. This is due to the fact that, since each information contribution is counted only once, the P_α is more sensitive to the phenomena, which occur less frequently in the image. The monotonic course of the P_α would be achieved only when a sequence of time-evolved Euclidian objects was transformed into the values $\Omega_\alpha^{(l \rightarrow m)}$.

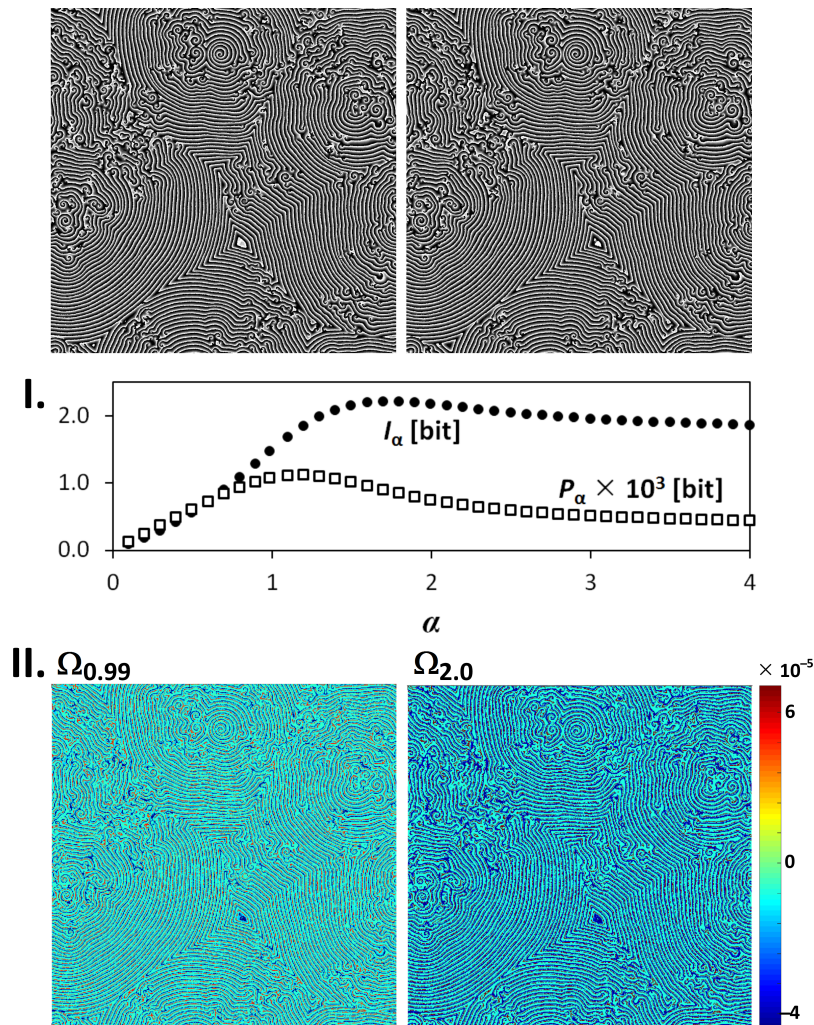


Figure 4. The I_α , P_α , and Ω_α for a pair of multifractal grayscale images. I. The I_α and P_α spectra, II. 8-bit visualization of Ω_α -values for $\alpha = \{0.99; 2.0\}$.

As mentioned in Section 2.2, the variables I_α and P_α measure absolute information change between a pair of images and characterize a similarity between these images. Therefore, these variables can find a practical utilization in auto-focusing in both light and electron digital microscopy. The in-focus object can be defined as an image with the global extreme of I_α or P_α . In other characteristics, this image fulfils the Nijboer–Zernike definition [24]: it is the smallest and darkest image in light or electron diffraction or the smallest and brightest image in light fluorescence (Section 3.3).

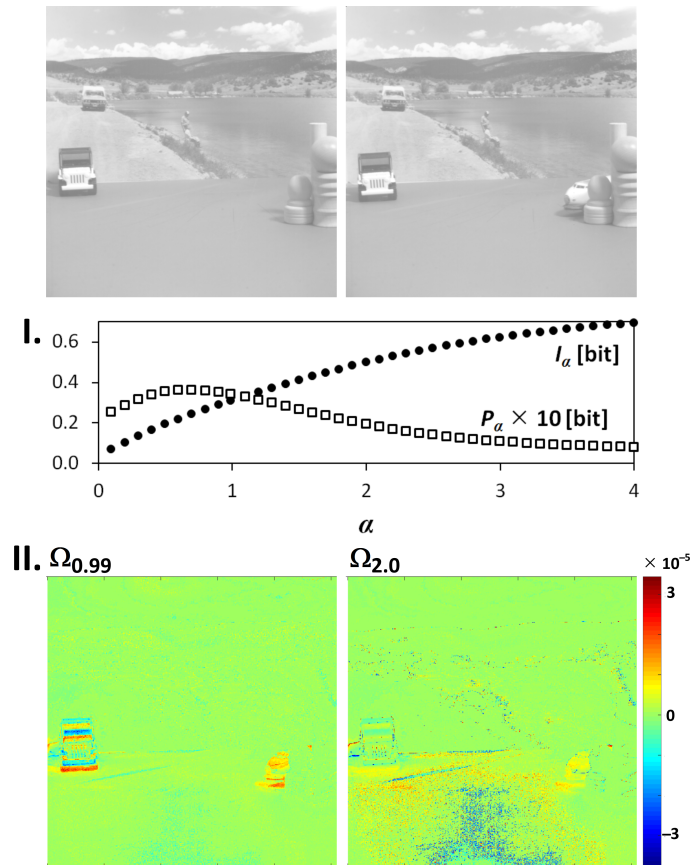


Figure 5. The I_α , P_α , and Ω_α for a pair of real-life grayscale images. I. the I_α and P_α spectra; II. 8-bit visualization of Ω_α -values for $\alpha = \{0.99; 2.0\}$.

3.2. Image Filtering and Segmentation

Segmentation is a type of filtering of specific features in an image. The parameter α and the related value of $\Omega_\alpha^{(l \rightarrow m)}$ enable us to filter the parts of two consecutive images, which are either stable or differently variable in time. This can be employed in a 3D image reconstruction by thresholding and joining $\Omega_\alpha^{(l \rightarrow m)} = 0$ from two consecutive images or in image tracking via thresholding of the highest and lowest $\Omega_\alpha^{(l \rightarrow m)}$ in a first image and the following image, respectively.

This is illustrated using simple examples in Figures 4 and 5 where the highest (red-coded) and lowest (blue-coded) values of the $\Omega_\alpha^{(l \rightarrow m)}$ show the position of the object in the second and the first image of the image sequence, respectively. Compared with the $\Omega_{0.99}^{(l \rightarrow m)}$, the variance between the extremes of the $\Omega_{2.00}^{(l \rightarrow m)}$ is wider and the number of points $\Omega_{2.00}^{(l \rightarrow m)} = 0$ is lower.

In digital light transmission microscopy, this mathematical method enabled us to find time stable intracellular objects inside live mammalian cells from consecutive pixels that fulfilled the equality $\Omega_\alpha^{(l \rightarrow m)} = 0$ for $\alpha = 4.00$ [6] or $\alpha = 5.00$ [7]. In these cases, the high value of α ensured merging rare points in the image, suppressing the camera noise that was reflected in the images and, thus, modelling the shape of organelles. The rest of image escaped the observation. In the next paper [25], this method was extended to widefield fluorescent data.

As in the case of the Point Information Gain [2], the process of image segmentation of objects of a certain shape can be further improved by usage of the surroundings of this shape from which the intensity histogram is created for each pixel in the image.

3.3. Clustering of Image Sets

Finally, we used the Point Divergence Gain to detect the most relevant information contained in a sequence of images, capturing, e.g., an experiment. For this end, we used I_α or P_α as quantities of information change in the consecutive images and applied the clustering methods on them. The values of I_α or P_α are small numbers (Section 2.1). Due to the computation rounding of small numbers of the I_α and the P_α and for a better characterization of the image multifractality, in clustering, we use α -dependent spectra of these variables than a sole number at one α .

The dependence of the label of the cluster on the order of the image in the series is the smoothest for joint vectors $[I_\alpha, P_\alpha]$. The similarity of these vectors (and thus images as well) is described in a space of principal components, e.g., [26], and classified by standard clustering algorithms such as k-means++ algorithm [27]. In comparison to the entropies and entropy densities related to the $\Gamma_\alpha^{(i)}$, the clustering using the I_α and the P_α is more sensitive to changes in the patterns (intensities) and does not require other specification of images by local entropies computed from a specific type of surroundings around each pixel.

The described clustering method was examined on z-stacks obtained using light microscopy. The z-stacks were classified into 2–6 clusters (groups) when patterns of each image was described by 26 numbers, i.e., by vectors $[I_\alpha, P_\alpha]$ at 13 α (Figures 6a and 7a). These clusters were evaluated on the basis of the sizes of intensity changes between images. These five classification graphs of the gradually splitting clusters (Figures 6a and 7a, middle) further demonstrate the mutual similarity among the micrographs in each data series. The typical (middle) image of each cluster is shown in Figures 6b and 7b.

Firstly, we shall deal with a z-stack with 1057 images of a microring obtained using a widefield fluorescent microscope. The results of clustering illustrate a canonically repetitive properties of the so-called point spread function as the image of the observed object goes to and from its focus. In this case, the image group containing the real focus of the maximal I_α and P_α at low α (Section 3.1) is successfully determined by clustering into two clusters (Figure 6a). However, we will aim for a description of the results for five clusters. The central Cluster 5 (94 images) can be called an object's focal region with image levels where parts of the object have their own focus. The in-focus cluster is asymmetrically surrounded by Cluster 4 (131 and 53 images below and above Cluster 5, respectively), which was set on the basis of the occurrence of the lower peaks of I_α and P_α at low α . Cluster 3 (190 and 150 images below and above the focus, respectively) is typical of constant I_α and P_α for all α . Cluster 2 contains img. 176–214 and the last 126 images. These images are characteristic of constant I_α and decreasing/increasing P_α at $\alpha \geq 2$. Cluster 1 (the first 175 images) is prevalently dominated by increasing I_α and decreasing P_α at high α .

Before the calculation of the I_α and P_α , the undesirable background intensities were removed from the images obtained using optical transmission microscopy. The rest of each image was rescaled into 8 bits (Section 4.2). The results of clustering of these images (Figure 7a) are similar to fluorescent data (Figure 6a). The light transmission point spread function is symmetrical around its focus as well but the pixels at the same x, y -positions below and above the focus have opposite, dark vs. bright, intensities. Furthermore, the transitional regions between the clusters are longer than for the fluorescent data. The central, in-focus, part of the z-stack (img. 427–561 in Cluster 4) with the highest peaks of I_α and P_α is unambiguously separated using four clusters. The focus itself lies at the 505th image. This central part of the z-stack is surrounded by eight groups of images which were, due to their similarity, objectively classified into three clusters. Cluster 1 was formed by images 1–78, 376–426, and 562–661. These images show peaks of middle values of the I_α and P_α . Images 79–153, 292–375, and 662–703 were classified into Cluster 2 (dominated by the local minimum of the I_α at $\alpha < 1$). Cluster 3

is related to the images with the lowest values of the I_α together with the lowest values and local peaks of the P_α for $\alpha < 1$ and for $\alpha > 1$, respectively. This cluster contains images 154–291 and the last 537 images of the series.

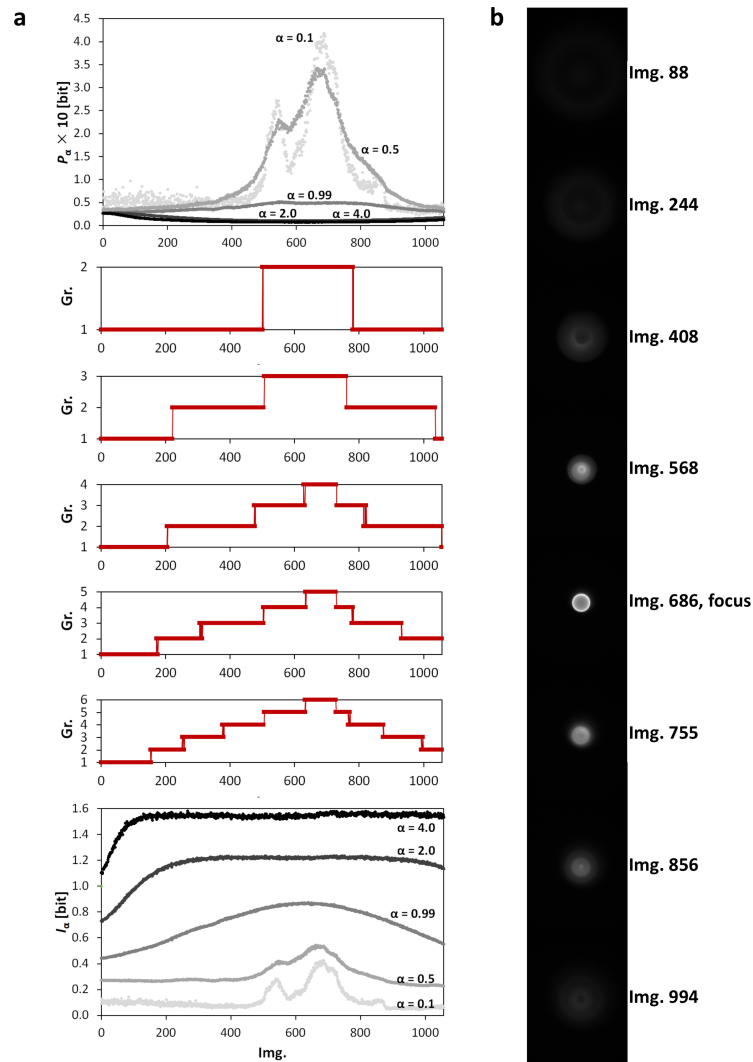


Figure 6. The results of clustering of a z-stack of grayscale microscopic images of a microring obtained using a fluorescence mode. (a) the dependencies of (upper) the P_α and (lower) the I_α vs. order of the image in the z-stack for $\alpha = \{0.5; 0.99; 2.0; 4.0\}$ and (middle) clustering (k-means, squared Euclidian distance, 2–6 groups) of the z-stack using connected spectra [I_α, P_α] for $\alpha = \{0.1; 0.3; 0.5; 0.7; 0.99; 1.3; 1.5; 1.7; 2.0; 2.5; 3.0; 3.5; 4.0\}$; (b) the typical (middle) group’s images for clustering into five groups (in (a), middle). The original 12-bit images are visualized in 8 bits using the Least Information Loss conversion [23].

Let us mention that, in the clustering process, the I_α and P_α can recognize outliers such as incorrectly saved images or images with illumination artifacts.

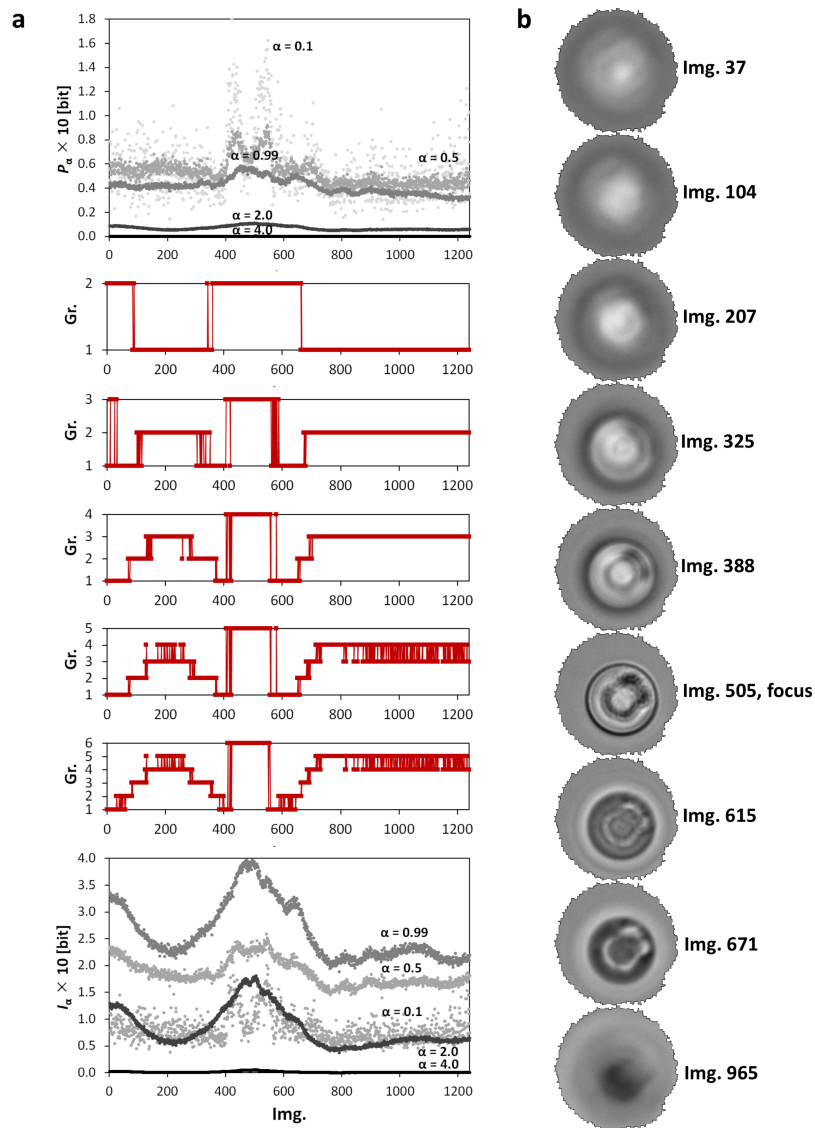


Figure 7. The results of clustering of a z-stack of grayscale microscopic images of a microring obtained using a diffraction mode. (a) the dependencies of (upper) the P_α and (lower) the I_α vs. order of the image in the z-stack for $\alpha = \{0.5;0.99;2.0;4.0\}$ and (middle) clustering (k-means, squared Euclidian distance, 2–6 groups) of the z-stack using connected spectra $[I_\alpha, P_\alpha]$ for $\alpha = \{0.1;0.3;0.5;0.7;0.99;1.3;1.5;1.7;2.0;2.5;3.0;3.5;4.0\}$; (b) the typical (middle) group’s images for clustering into 5 groups (in (a), middle). The original 12-bit images are visualized in 8 bits using the Least Information Loss conversion [23].

4. Materials and Methods

4.1. Processing of Typical Histograms

For the Cauchy, Lévy, Gauss, and Rayleigh distributions, dependences of the $\Omega_\alpha^{(l \rightarrow m)}$ on the number of elements in bins l and m were calculated for $\alpha = \{0.1, 0.3, 0.5, 0.7, 0.99, 1.3, 1.5, 1.7, 2.0, 2.5, 3.0, 3.5, 4.0\}$ using a `pdg_histograms.m` Matlab® 2014 script (Mathworks, Natick, MA, USA). The following probability density functions $f(x)$ were studied:

1. Lévy distribution:

$$f(x) = \text{round} \left[10^c \frac{\exp\left(-\frac{1}{2x}\right)}{\sqrt{2\pi x^3}} \right], \quad x \in \mathbb{N}, \quad \begin{cases} x \in [1, 256], & c \in \{5, 7\}, \\ x \in [1, 85], & c = 3, \end{cases} \quad (19)$$

2. Cauchy distribution:

$$f(x) = \text{round} \left[10^c \frac{1}{\pi(1+x^2)} \right], \quad x \in \mathbb{Z}, \quad \begin{cases} x \in [-127, 127], & c = 7, \\ x \in [-44, 44], & c = 3.5, \end{cases} \quad (20)$$

3. Gauss distribution:

$$f(x) = \text{round} \left[10^c \frac{\exp\left(-\frac{x^2}{2\sigma^2}\right)}{\sigma\sqrt{2\pi}} \right], \quad x \in \mathbb{Z}, \quad \begin{cases} x \in [-4, 4], & c = 4, \quad \sigma = 1, \\ x \in [-29, 29], & c = 3, \quad \sigma = 10, \\ x \in [-36, 36], & c = 4, \quad \sigma = 10, \\ x \in [-64, 64], & c = 10, \quad \sigma = 10, \end{cases} \quad (21)$$

4. Rayleigh distribution:

$$f(x) = \text{round} \left[10^c \frac{x}{b^2} \exp\left(-\frac{x^2}{2b^2}\right) \right], \quad x \in \mathbb{N}, \quad x \in [1, 108], \quad c = 10, \quad b = 16. \quad (22)$$

In Figure 1, the Cauchy and Lévy distributions at $c = 7$ and the Gauss distribution at parameters $c = 10$ and $\sigma = 10$ are depicted.

4.2. Image Processing and Analysis

Image analysis based on calculation of the $\Omega_\alpha^{(l \rightarrow m)}$, I_α , and P_α is demonstrated on five standard grayscale multi-image series (Table 1). All images were processed using Whole Image mode in an Image Info Extractor Professional software (Institute of Complex Systems, FFPW, USB, Nové Hradky, Czech Republic). A pair of images 5000–5001 of a simulated Belousov–Zhabotinsky (BZ) reaction and a pair of images motion01.512–motion02.512 were recalculated for 40 values of $\alpha = \{0.1, 0.2, \dots, 0.9, 0.99, 1.1, 1.2, \dots, 4.0\}$. The rest of series were processed for 13 values of $\alpha = \{0.1, 0.3, 0.5, 0.7, 0.99, 1.3, 1.5, 1.7, 2.0, 2.5, 3.0, 3.5, 4.0\}$. The transformation at 13 α was followed by clustering of the matrices $[P_\alpha, I_\alpha]$ vs. `Img.` by k -means method (squared Euclidian distance metrics). Due to a high data variance in the BZ simulation, the clustering was preceded by the z-score standardization of the matrices over α . The resulted indices of clusters were reclassified to be consecutive (i.e., the first image of the series and the first image of the following group are classified into gr. 1 and 2, respectively, etc.).

5. Conclusions

In this paper, we derived novel variables from the Rényi entropy—a Point Divergence Gain $\Omega_\alpha^{(l \rightarrow m)}$, a Point Divergence Gain Entropy I_α , and a Point Divergence Gain Entropy Density P_α . We have

discussed their theoretical properties and made a brief comparison with the related quantity called Point Information Gain Γ_{α}^i [2]. Moreover, we have shown that the $\Omega_{\alpha}^{(l \rightarrow m)}$ and related quantities can find their applications in multidimensional data analysis, particularly in video processing. However, due to element-by-element computation, we can characterize time-spatial (4-D) changes much more sensitively than using, e.g., the previously derived Γ_{α}^i . The $\Omega_{\alpha}^{(l \rightarrow m)}$ can be considered as a microstate of the information changes in the space-time. However, the $\Omega_{\alpha}^{(l \rightarrow m)}$, I_{α} , and P_{α} show a property that is similar to the Γ_{α}^i and its relative macroscopic variables. Due to the derivation from the Rényi entropy, they are good descriptors of multifractality. Therefore, they can be utilized to characterize patterns in datasets and to classify the (sub)data into groups of similar properties. This has been successfully utilized in clustering of multi-image sets, image filtration, and image segmentation, namely in microscopic digital imaging.

Acknowledgments: This work was supported by the Ministry of Education, Youth and Sports of the Czech Republic—projects CENAKVA (No. CZ.1.05/2.1.00/01.0024), CENAKVA II (No. LO1205 under the NPU I program), the CENAKVA Centre Development (No. CZ.1.05/2.1.00/19.0380)—and from the European Regional Development Fund in frame of the project Kompetenzzentrum MechanoBiologie (ATCZ133) in the Interreg V-A Austria—Czech Republic programme. J.K. acknowledges the financial support from the Czech Science Foundation Grant No. 17-33812L and the Austrian Science Fund, Grant No. I 3073-N32.

Author Contributions: Renata Rychtáriková is the main author of the text and tested the algorithms; Jan Korbek is responsible for the theoretical part of the article; Petr Macháček is the developer of the Image Info Extractor Professional software; Dalibor Štys is the group leader who derived the point divergence gain. All authors have read and approved the final manuscript.

Conflicts of Interest: The authors declare no conflict of interest.

References

- Rychtáriková, R. Clustering of multi-image sets using Rényi information entropy. In *Bioinformatics and Biomedical Engineering (IWBBIO 2016)*; Lecture Notes in Computer Science Series; Ortuño, F., Rojas, I., Eds.; Springer: Cham, Switzerland, 2016; pp. 527–536.
- Rychtáriková, R.; Korbek, J.; Macháček, P.; Císař, P.; Urban, J.; Štys, D. Point information gain and multidimensional data analysis. *Entropy* **2016**, *18*, 372.
- Jizba, P.; Kleinert, H.; Shefaat, M. Rényi's information transfer between financial time series. *Phys. A Stat. Mech. Appl.* **2012**, *391*, 2971–2989.
- Jizba, P.; Korbek, J. Multifractal diffusion entropy analysis: Optimal bin width of probability histograms. *Phys. A Stat. Mech. Appl.* **2014**, *413*, 438–458.
- Jizba, P.; Korbek, J. Modeling Financial Time Series: Multifractal Cascades and Rényi Entropy. In *ISCS 2013: Interdisciplinary Symposium on Complex Systems; Emergence, Complexity and Computation Series*; Sanayei, A., Zelinka, I., Rössler, O., Eds.; Springer: Berlin/Heidelberg, Germany, 2014.
- Rychtáriková, R.; Náhlík, T.; Smaha, R.; Urban, J.; Štys, D., Jr.; Císař, P.; Štys, D. Multifractality in imaging: Application of information entropy for observation of inner dynamics inside of an unlabeled living cell in bright-field microscopy. In *ISCS14: Interdisciplinary Symposium on Complex Systems*; Sanayei, A., Zelinka, I., Rössler, O.E., Eds.; Springer: Berlin/Heidelberg, Germany, 2015; pp. 261–267.
- Rychtáriková, R.; Náhlík, T.; Shi, K.; Malakhova, D.; Macháček, P.; Smaha, R.; Urban, J.; Štys, D. Super-resolved 3-D imaging of live cells' organelles from bright-field photon transmission micrographs. *Ultramicroscopy* **2017**, *179*, 1–14.
- Chevalier, C.; Bect, J.; Ginsbourger, D.; Vazquez, E.; Picheny, V.; Richet, Y. Fast parallel kriging-based stepwise uncertainty reduction with application to the identification of an excursion set. *Technometrics* **2014**, *56*, 455–465.
- Eidsvik, J.; Mukerji, T.; Bhattacharjya, D. *Value of Information in the Earth Sciences: Integrating Spatial Modeling and Decision Analysis*; Cambridge University Press: Cambridge, UK, 2015.
- Helle, K.B.; Pebesma, E. Optimising sampling designs for the maximum coverage problem of plume detection. *Spat. Stat.* **2015**, *13*, 21–44.
- Jizba, P.; Arimitsu, T. The world according to Rényi: Thermodynamics of multifractal systems. *Ann. Phys.* **2004**, *312*, 17–59.

12. Rényi, A. On measures of entropy and information. In Proceedings of the Fourth Symposium on Mathematical Statistics and Probability, Berkeley, CA, USA, 20 June–30 July 1961; Volume 1, pp. 547–561.
13. Kullback, S.; Leibler, R.A. On information and sufficiency. *Ann. Math. Stat.* **1951**, *22*, 79–86.
14. Csiszár, I. I-divergence geometry of probability distributions and minimization problems. *Ann. Probab.* **1975**, *3*, 146–158.
15. Harremoës, P. Interpretations of Rényi entropies and divergences. *Phys. A Stat. Mech. Appl.* **2006**, *365*, 5–62.
16. Van Erven, T.; Harremoës, P. Rényi divergence and Kullback-Leibler divergence. *J. Latex Class Files* **2007**, *6*, 1–24.
17. Van Erven, T.; Harremoës, P. Rényi divergence and majorization. In Proceedings of the IEEE International Symposium on Information Theory, Austin, TX, USA, 13–18 June 2010; pp. 1335–1339.
18. Shannon, C.E. A mathematical theory of communication. *ACM SIGMOBILE Mob. Comput. Commun.* **2001**, *5*, 3–55.
19. Volume 1: Textures. Available online: <http://sipi.usc.edu/database/database.php?volume=textures&image=61#top> (accessed on 31 January 2018).
20. Štys, D.; Jizba, P.; Zhyrova, A.; Rychtáriková, R.; Štys, K.M.; Náhlík, T. Multi-state stochastic hotchpotch model gives rise to the observed mesoscopic behaviour in the non-stirred Belousov-Zhabotinsky reaction. *arXiv* **2016**, arXiv:1602.03055. Available online: <https://arxiv.org/abs/1602.03055> (accessed on 31 January 2018).
21. Štys, D.; Náhlík, T.; Zhyrova, A.; Rychtáriková, R.; Papáček, Š.; Císař, P. Model of the Belousov-Zhabotinsky reaction. In Proceedings of the International Conference on High Performance Computing in Science and Engineering, Soláň, Czech Republic, 25–28 May 2015; Kozubek, T., Blaheta, R., Šístek, J., Eds.; Springer: Cham, Switzerland, 2016; pp. 171–185.
22. Štys, D.; Štys, K.M.; Zhyrova, A.; Rychtáriková, R. Optimal noise in the hodgepodge machine simulation of the Belousov-Zhabotinsky reaction. *arXiv* **2016**, arXiv:1606.04363. Available online: <https://arxiv.org/abs/1606.04363> (accessed on 31 January 2018).
23. Štys, D.; Náhlík, T.; Macháček, P.; Rychtáriková, R.; Saberioon, M. Least Information Loss (LIL) conversion of digital images and lessons learned for scientific image inspection. In Proceedings of the International Conference on Bioinformatics and Biomedical Engineering, Granada, Spain, 20–22 April 2016; Ortuño, F., Rojas, I., Eds.; Springer: Cham, Switzerland, 2016; pp. 527–536.
24. Braat, J.J.M.; Dirksen, P.; van Haver, S.; Janssen, A.J.E.M. Extended Nijboer-Zernike (ENZ) Analysis & Aberration Retrieval. Available online: <http://www.nijboerzernike.nl> (accessed on 12 December 2017).
25. Rychtáriková, R.; Steiner, G.; Kramer, G.; Fischer, M.B.; Štys, D. New insights into information provided by light microscopy: Application to fluorescently labelled tissue section. *arXiv* **2017**, arXiv:1709.03894. Available online: <https://arxiv.org/abs/1709.03894> (accessed on 31 January 2018).
26. Jolliffe, I.T. *Principal Component Analysis*, 2nd ed.; Springer Series in Statistics; Springer: New York, NY, USA, 2002.
27. Arthur, D.; Vassilvitskii, S. k-means++: The advantages of careful seeding. In Proceedings of the 18th ACM-SIAM, Philadelphia, PA, USA, 7–9 January 2007; pp. 1027–1035.



■ **Quasi-spectral characterization of intracellular regions in bright-field light microscopy images**

K. Lonhus, **R. Rychtáriková**, G. Platonova a D. Štys, *Quasi-spectral characterization of intracellular regions in bright-field light microscopy images*, Scientific Reports **10** (2020), 18346.

V této práci je odvozena metoda stanovení transmittančních spekter využitím obyčejné digitální barevné kamery, tzv. (kvazi)spektrální analýza. Tu je možné potenciálně použít při mikrospektroskopických měřeních struktur buněk a materiálů jako plošnou, a tudíž rychlejší verzi hyperspektrální kamery. Výpočet (kvazi)spekter zahrnuje výpočetní metodu kalibrace a korekce mikroskopických obrazových dat popsanou v

- G. Platonova, D. Štys, P. Souček, K. Lonhus, J. Valenta a **R. Rychtáriková**, *Spectroscopic approach to correction and visualisation of bright-field light transmission microscopy biological data*, Photonics **8** (2021), 333.

Publikace byla obsahem tiskové zprávy z 18. 11. 2020 s cca 30 mediálními výstupy včetně ČT.



OPEN

Quasi-spectral characterization of intracellular regions in bright-field light microscopy images

Kirill Lonhus[✉], Renata Rychtáriková, Ganna Platonova & Dalibor Štys

Investigation of cell structure is hardly imaginable without bright-field microscopy. Numerous modifications such as depth-wise scanning or videoenhancement make this method being state-of-the-art. This raises a question what maximal information can be extracted from ordinary (but well acquired) bright-field images in a model-free way. Here we introduce a method of a physically correct extraction of features for each pixel when these features resemble a transparency spectrum. The method is compatible with existent ordinary bright-field microscopes and requires mathematically sophisticated data processing. Unsupervised clustering of the spectra yields reasonable semantic segmentation of unstained living cells without any a priori information about their structures. Despite the lack of reference data (to prove strictly that the proposed feature vectors coincide with transparency), we believe that this method is the right approach to an intracellular (semi)quantitative and qualitative chemical analysis.

List of symbols

\mathbb{B}_{mn}	Set of pixels that form lines between pixels m and n
c	Colour of a camera filter or an image channel; for colour camera $c = \{red, green, blue\}$
C	Number of image channels
D_k	Central intensity gradient in pixel $k \in \mathbb{B}_{mn}$ in calculation of G_{mn}
E	Energy absorbed by a camera sensor during an exposure time t_e
\mathcal{E}_k	Parameter in computation of G_{mn} which indicates if the pixel k is classified as an region edge
f	Variable which reflects a dependence between the spectral energy and the sensor response; $f = 1$
$F_c(\lambda)$	Spectral quantum efficiency of a camera filter c
F_m	Spectral quantum efficiency of a pixel m
G_{mn}	Measure of discontinuousness between pixels m and n
i	Label of a discrete wavelength; $i = \{1, 2, \dots, w\}$
iter	Iteration
it_max	Maximal iteration (predetermined)
I_c	Pixel intensity at colour channel c
k	Pixel in the set \mathbb{B}_{mn}
L_c	Light effectively incoming onto a camera sensor, i.e. onto a camera filter
m, n	Pixel labels
M_i	Intensity value in the image
N	Number of pixels in the set \mathbb{N}_m
\mathbb{N}_m	Set of pixels with the Euclidean distance to the pixel m equal or less than \mathcal{T}_{ED}
q	Parameter related to the degree of discontinuousness in spectral regions
\vec{r}	Position vector for a pixel at coordinates (x, y)
S	Integral of the spectrum measured by the fibre spectrophotometer in each point S_i
$S(\lambda)$	Light spectrum of a light source
t_e	Camera exposure time

University of South Bohemia in České Budějovice, Faculty of Fisheries and Protection of Waters, South Bohemian Research Center of Aquaculture and Biodiversity of Hydrocosenoses, Kompetenzzentrum MechanoBiologie in Regenerativer Medizin, Institute of Complex Systems, Zámek 136, 373 33 Nové Hradky, Czech Republic. ✉email: lonhus@frov.jcu.cz

T	Thermodynamic temperature; kelvin [K]
$T_m(\lambda_i)$	Transparency spectrum of pixel m at wavelength λ_i
$T_n(\lambda_i)$	Transparency spectrum of pixel n at wavelength λ_i
$T(x, y, \lambda)$	Transparency spectrum of a medium at each pixel in general
T_b	Bias parameter in computation of G_{mn} ; $T_b = 0.9$
T_{ED}	Threshold for the selection of the neighbourhood of pixel m , i.e., the Euclidean distance between pixels m and n ; $T_{ED} = 1$
\vec{u}	Change of a pixel position vector
w	Number of discrete wavelengths
x, y	Vertical and horizontal pixel coordinates
ϵ	Parameter which reflects the studied pixel's neighbourhood size in general
λ	Light wavelength; nanometer [nm]

Bright-field microscopy in videoenhancement mode shows an unprecedented success as a method of living object investigation since it is cheap and non-intrusive in preparation of samples, and, in its innovative set-up¹, has an excellent spatial and temporal resolution, which opens many possibilities for automation. Classical image-processing techniques such as feature extraction or convolution neural networks do not work so well due to huge variability in microworld data. It calls for image pre-processing techniques that would utilize all available information to supply rich, physically relevant feature vectors in subsequent methods of analysis.

Indeed, classical bright-field microscopy measures properties of incoming light affected by a sample. If multi-photon processes are negligible and, then, intensities are reasonable, a linear response model can be used. Then, a medium observed in such a model can be fully characterized by a transparency spectrum $T(\vec{r})$ defined for each pixel. Such a spectrum can give ultimate information about the medium and boost subsequent machine learning methods significantly.

The most convenient, classical way of obtaining such a spectrum is to modify a measuring device (microscope). It is mostly done using single scanning interferometers², matrices of them³, matrices of color filter arrays⁴, or other adjustable media^{5,6}. Such technical arrangements can be further successfully coupled with machine learning methods as well⁷. Purely instrumental methods are certainly the most correct but require sophisticated equipment and are not fully compatible with typical bright-field techniques like depth-wise z-scanning. Due to both hardware and algorithms, this makes these methods rather a separated group than a subtype of the bright-field methods.

For classical bright-field microscopy, the most approaches rely on trained (or fitted) models based on a set of reference images with known properties⁸. Most mature methods rely on the principal component analysis⁹ or sparse spatial features¹⁰. Some of such techniques do not aim to full-spectral reconstruction but rather to a more effective colour resolution (which has been very useful in distinguishing fluorescence peaks)¹¹. The main disadvantage of such methods is the global approach, which is feasible only for homogeneous images. Most "local" methods include different artificial neural networks¹², and can work well if they are trained with a reference dataset that is similar to the observed system. The data of this kind almost never occurs in microscopy due to bigger variability of objects in microworld (for the reason that, e.g., known objects are artificial, an investigated system is living, or the in-focus position can be ambiguous). This gives a cutting edge to physically inspired methods which make no assumption about type of observed object and does not use special equipment except of a classical bright-field microscope.

Theoretical model

For most biologically relevant objects multi-photon interactions can be neglected¹³. Thus, a linear response model can be used for description of the measurement process. The model consists of four entities (Fig. 1) which are physically characterized as follows:

1. *Light source* gives a light spectrum $S(\lambda)$, which is assumed constant and spatially homogeneous.
2. *Medium* is, in each point of the projection onto a camera sensor plane, characterized by an unknown transparency spectrum $T(x, y, \lambda)$.
3. *Camera filter*, where each camera channel c is characterized by a quantum efficiency curve $F_c(\lambda)$.
4. *Camera sensor* is described (by purely phenomenological approach) by exposure time t_e and energy load curve $I_c = f(E)$, where I_c is the pixel sensor output (intensity) and E is energy absorbed by the pixel sensor during the exposure time. We assume that the image is not saturated and, thus, $f(E)$ can be approximated linearly.

Mathematically, it can be expressed as

$$I_c = f \cdot \int_0^{t_e} \int_{\lambda_{\min}}^{\lambda_{\max}} S(\lambda) \cdot T(\lambda) \cdot F_c(\lambda) \cdot d\lambda \cdot dt, \quad (1)$$

where I_c is the image intensity at a given pixel. All observable, biologically relevant, processes are slow compared with the camera exposure time (usually in a few ms) and, therefore, the outer integral can be eliminated. More importantly, let variable f , which reflects the dependence between the spectral energy and the sensor response, be 1. The multiplication inside the internal integral is commutative, which allows us to introduce an effective incoming light $L_c(\lambda) = S(\lambda) \cdot F_c(\lambda)$. These all mathematical treatments give the reduced equation for the measurement process as

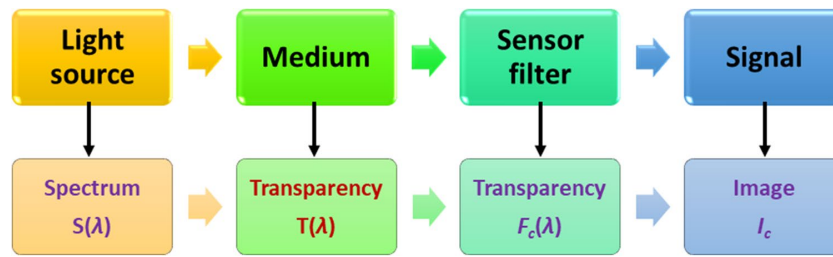


Figure 1. Measurement process model.

$$I_c = \int_{\lambda_{min}}^{\lambda_{max}} L_c(\lambda) \cdot T(\lambda) \cdot d\lambda. \tag{2}$$

Intentionally, this simple model does not include any properties of optics, sophisticated models of light-matter interactions, and spatial components (focus, sample surface, etc.). The aim of the method is to describe an observed object in the best way, with minimal assumptions on its nature or features.

Model extension for continuous media

In order to extract a transparency profile from the proposed model, one has to solve an inverse problem for a system of three integral equations (in case of a 3-channel, RGB, camera). This cannot be solved directly, since the model is heavily underdetermined. (In this text, by terms “transparency” and “spectrum” we mean “quasi-transparency” and “quasi-spectrum” since this method determines only the properties of a microscopy image which are similar to the transparency spectra but not the transparency itself).

Additional information can be squeezed from the physical meaning of the observed image—neighbouring pixels are not fully independent. The observed object usually has no purely vertical parts (which is quite typical for cell-like structures) and other Z-axis related changes are not fast¹⁴. If this holds, the image can be treated as a continuous projection of the object’s surface (in optical meaning) onto the camera sensor. In this case, the neighbouring pixels correspond to neighbouring points in the object.

In addition, let us assume that the object’s volume can be divided into subvolumes in a way that the transparency spectra inside a subvolume will be spatially continuous (in L2 meaning). This assumption is quite weak, because it can be satisfied only if the volumetric image has a subvolume of the size which is equal to the voxel size.

For biological samples which show almost no strong gradients of structural changes holds that the pixel demarcates the projected image. Formally, this criterion can be expressed as

$$\int_{\lambda_{min}}^{\lambda_{max}} |T(\vec{r}, \lambda) - T(\vec{r} + \vec{u}, \lambda)|^2 d\lambda < q, \quad \forall |\vec{u}| < \epsilon, \tag{3}$$

where \vec{u} is a random vector and q, ϵ are small numbers. This equation closely resembles the Lyapunov stability criterion. The ϵ reflects the neighbourhood size and q is related to the degree of discontinuousness. It can be violated, if \vec{u} crosses a border between objects, but not inside a single object.

Optimization procedure

For pixel m , the combination of optimization criteria in Eqs. (2) and (3) gives (in discrete form)

$$F_m = \sum_{c=1}^C e^{|\int_{\lambda_0}^{\lambda_w} L_c(\lambda) \cdot T_m(\lambda) d\lambda - I_m|} - C + \frac{1}{N} \sum_{n \in \mathbb{N}_m} G_{mn} \sum_{i=1}^w [T_m(\lambda_i) - T_n(\lambda_i)]^2, \tag{4}$$

where C is the number of channels, w is the number of discrete wavelengths, G_{mn} is a measure of discontinuousness between pixels m and n . The \mathbb{N}_m is a set of points, which have the Euclidean distance to the pixel m equal or less than T_{ED} . Authors used $T_{ED} = 1$, but a larger neighbourhood may improve convergence speed. The integral in the first part of Eq. (4) is supposed to be solved numerically. Authors used the Simpson integration method¹⁵ with discretization $|\lambda_i| = 48$.

The trickiest issue in Eq. (4) is calculation of discontinuousness measure G_{mn} . We defined it as

$$G_{mn} = \frac{1}{L_{mn}} \prod_{k \in \mathbb{B}_{mn}} \{[\mathcal{E}_k = 0] + [\mathcal{E}_k \neq 0] \cdot (1 - T_b) \cdot (1 - D_k)\}, \tag{5}$$

where D_k is a central gradient in pixel k , T_b is a bias parameter (authors used $T_b = 0.9$), and \mathbb{B}_{mn} is a set of points, which form lines between pixels m and n . The set of such points is calculated using the Bresenham algorithm¹⁶. The \mathcal{E}_k indicates whether pixel k is classified as an edge. For this we used the Canny edge detection algorithm¹⁷ applied to a gradient matrix smoothed by a 2D Gaussian filter with the standard deviation equal¹⁸ to 0.5.

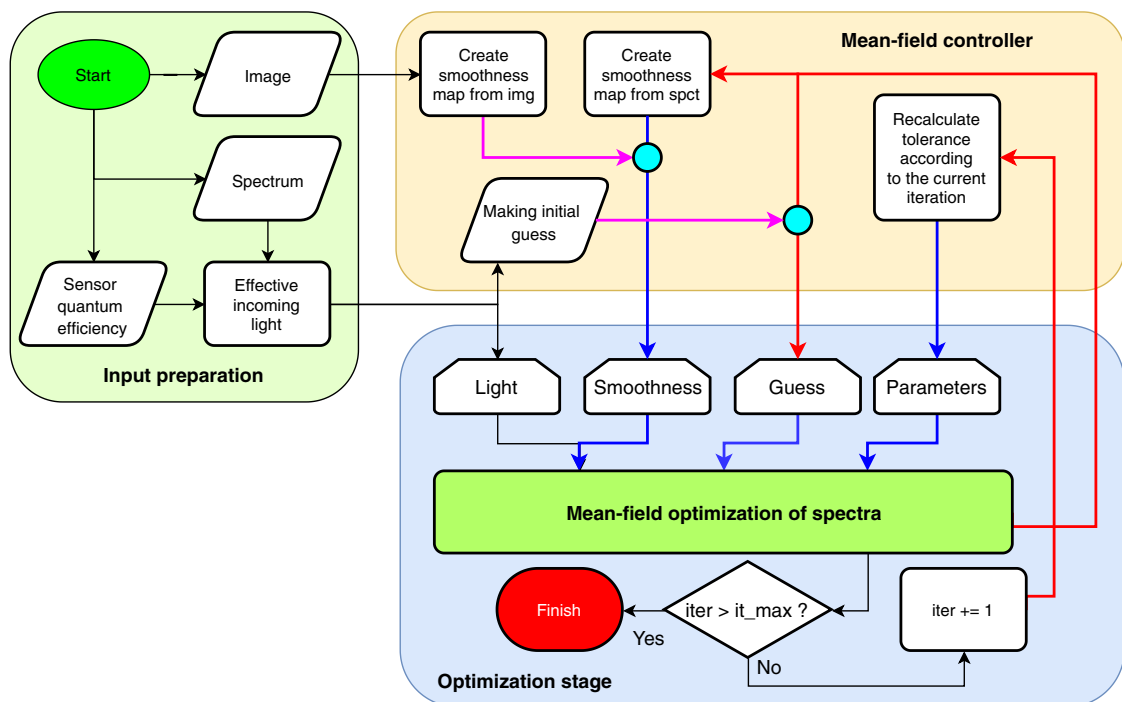


Figure 2. The flow chart of the method. The magenta lines denote the routes for the 1st iteration. The red and blue lines show the direct and indirect feedback between iterations, respectively.

The gradient calculation is different for the first and further iterations. In the first iteration, there is no valid spectral guess, and the gradients and the edge detection are calculated for the original image. The used edge detection algorithm requires a single-channel (grayscale) image, however, the input image is RGB. We used the principal component analysis (PCA)^{19,20} and retained only the first principal component in order to obtain the maximal information on the grayscale representation of data.

In the non-first iterations, there is a spectral guess and, instead of the gradient, we used the cross-correlation with zero lag: $D_k = T_{k-1}(\lambda) * T_{k+1}(\lambda)$. The vertical and horizontal gradient were merged by the Euclidean norm.

For numerical optimization of Eq. (4), the covariance matrix adaptation evolution strategy (CMA-ES)²¹ was proved to be a suitable robust global optimization method²². Due to the mean-field nature of the second part of Eq. (4), the method is iterative with, usually, 20–40 iterations to converge. In each iteration step and for each pixel, the minimization is conducted until a predefined value of loss function is achieved. Different schedules of tolerance changes can be applied, authors used the simplest one—linear decrease. The algorithm flow chart is presented in Fig. 2.

Microscopy system and camera calibration

In order to obtain reasonable local spectra, we must ensure that camera sensor pixels have homogeneous responses. From hardware point of view, they are printed as semiconductor structures and cannot be changed. Therefore, we introduced a spectral calibration in the form of post-processing routine, which is designed for obtaining equal responses from all camera pixels.

The first part of calibration is experimental and aimed at measuring each pixel's sensitivity. We took a photograph of the background through a set of gray layers with varying transparency, covering a 2-mm thick glass (type Step ND Filter NDL-10S-4). After that, we replaced the microscope objective by a fibre of a spectrophotometer (Ocean Optics USB 4000 VIS-NIR-ES) to record spectra corresponding to each of the filters, see Fig. 3a.

The second part is computational. For each pixel, we constructed a piece-wise function $S(M)$, where S is an integral of the spectrum measured by the fibre spectrometer in each point S_i and M_i is an intensity value in the image. Between these points, the function $S(M)$ is linearly interpolated, see Fig. 3d. For a colour camera that we used, the algorithm is slightly different. Most of the RGB cameras are equipped with a Bayer filter, which effectively discriminates 3 sorts of pixels. Each 'sort' has a different dependence of the quantum efficiency on the wavelength, see Fig. 3b. These dependencies are usually supplied by the camera producer. In this case, the recorded spectrum should be multiplied by the corresponding efficiency curve prior to the integration. The result of the multiplication is shown in Fig. 3c.

The proposed method of calibration is universal, applicable to any camera producing raw data, and is not based on any assumption about nature of image or underlying acquisition processes. The algorithm itself is

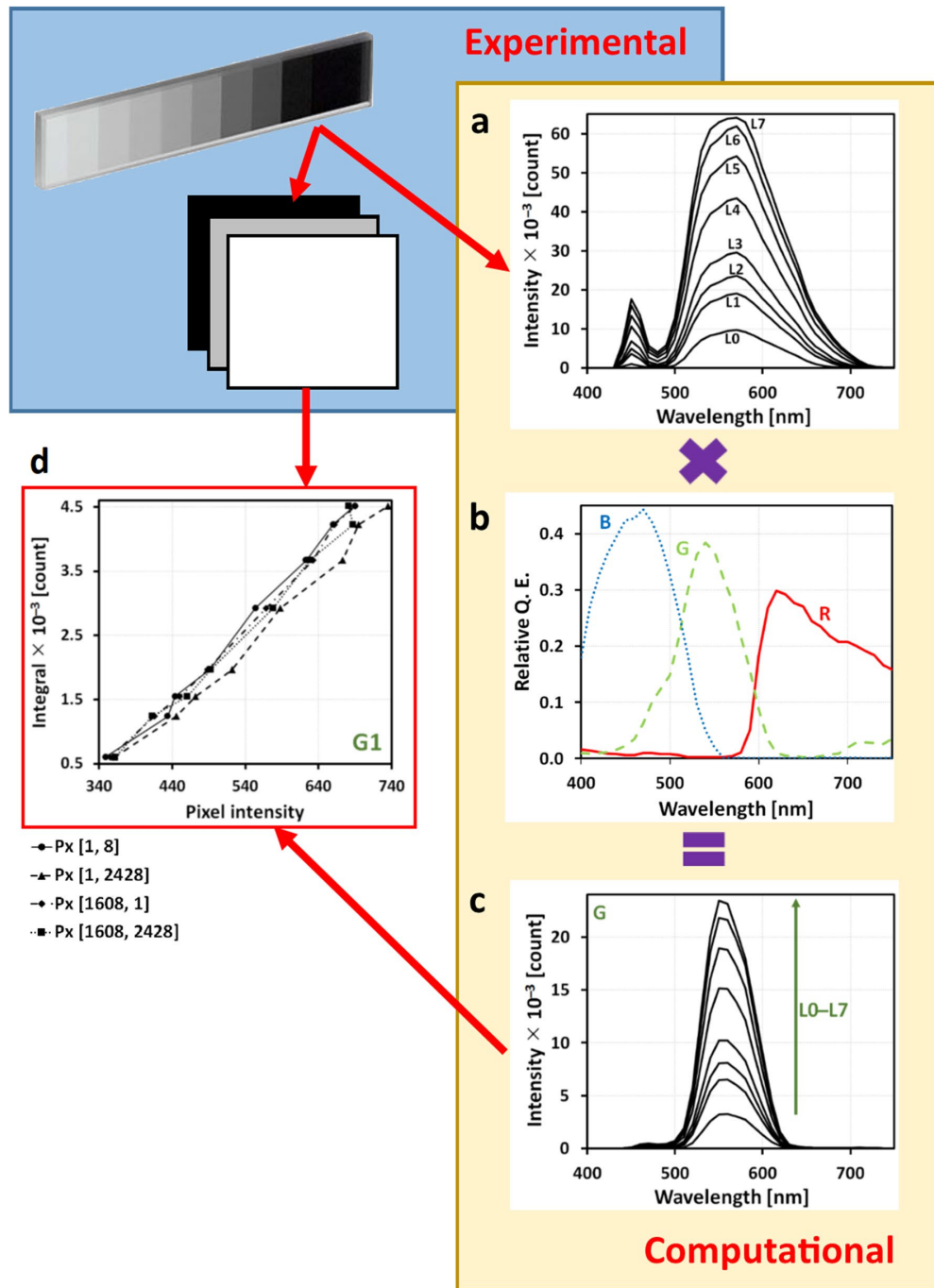


Figure 3. (a) Light spectra of grayscale layers measured by a fibre spectrophotometer, (b) declared spectra of RGB camera filters, (c) calculated spectra of incoming light reaching the blue camera channel. The integral under the curve (c) was used as a calibration value for the construction of the calibration curve. (d) Calibration curves for selected blue camera pixels lying in the same column (pixel indices are depicted).

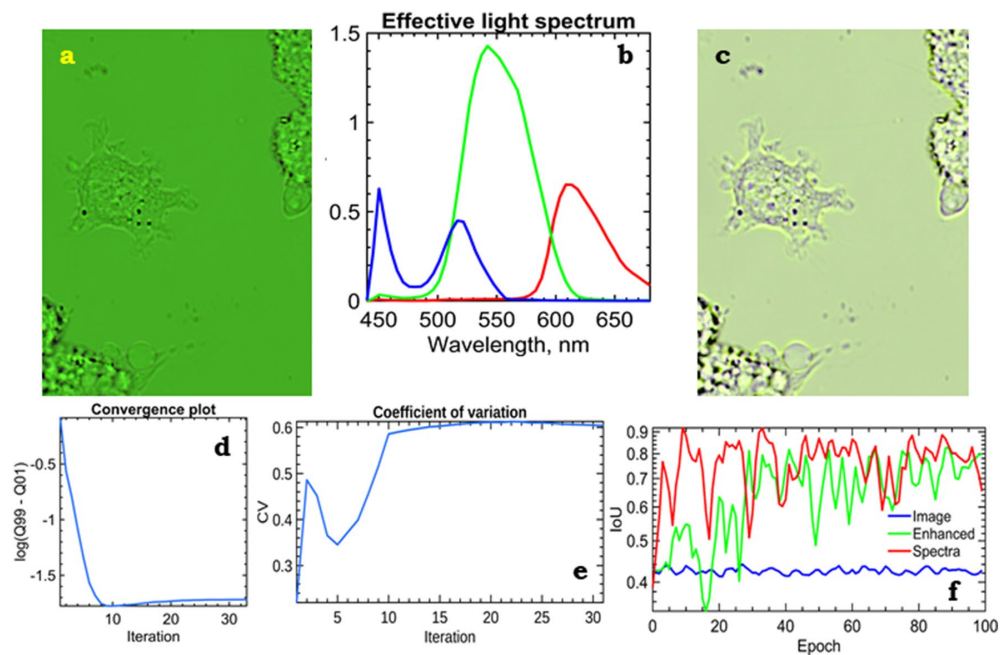


Figure 4. The method of quasi-spectra extraction was applied to a raw image of a live cell from a bright-field wide-field light microscope (a) combined with the effective light spectra (b). The cost (d) and variation coefficient (e) demonstrate a quite non-monotonous behaviour. This implies a self-organization of the model. After the reconstruction of the transparency spectra, the image can be viewed under arbitrary illumination such as the absolute black body with $T = 5800$ K (c). Comparison of the quality of U-Net supervised segmentation for original (raw), contrast-enhanced, and quasi-spectral images (f) shows advantages of the proposed quasi-spectral approach.

post-processing technique and requires calibration images and data from spectrometer. All results described below were obtained after this image correction. The calibration and correction routines are implemented as a native application and are freely available.

Results

The method essentially requires only three specific inputs: an image, incoming light spectrum, and camera filter profiles. The camera filter profiles are usually supplied with the camera or can be measured directly using an adjustable monochromatic light source. The incoming light spectrum is less straightforward, because the light emitted by the source is somehow altered by the light path. A convenient way is to replace the objective inlet by a cosine corrector with a spectrometer and measure the incident light spectrum. This implies that, in case of any substantial changes in the optical path (e.g., like the objective replacement), the incoming light spectrum has to be remeasured. In practice, it makes no problem to measure a set of spectra corresponding to a different objective, iris settings, etc.

The proposed method appears to be quite robust to parametrization inaccuracies and errors. We used the quantum efficiency curves supplied by the vendor and measured the spectrum, which is reaching the sample, and obtained practically feasible results. The method can be applied to any bright-field microscope set-up. The only condition is to access the camera primary signal immediately after the analog-to-digital conversion, before some kind of thresholding, white-balancing, gamma correction, or another visual improvement is employed.

The sample has to obey three assumptions: localized gradients, reasonable flatness, and linear response. If these assumptions hold, the obtained results will be in agreement with physical properties of the medium. Most of relatively flat biological samples (e.g., a single layer of cells) fulfil all these criteria. In order to show the capacity of the method, we used it for analysis of images of unstained live L929 mouse fibroblasts recorded using a video-enhanced bright-field wide-field light microscope in time lapse and with through-focusing. For determination of the best focal position in the z -stack, we used the graylevel local variance²³. The effective light spectrum as the result of multiplication of the light source spectrum by the camera filter transparency curves is shown in Fig. 4b. The original raw image is shown in Fig. 4a and looks greenish due to the prevalence of green colour in incoming light spectrum.

As clearly seen in Fig. 4d and e, the method has a non-trivial convergence behaviour of the variation coefficient (with the local maximum at iteration 2 and the local minimum at iteration 4) and of the cost. The behaviour of the iteration computing process is not related to changes in the schedule of tolerances. This behaviour in iteration process is linearly decreasing until iteration 10, and then is kept constant and the iteration process is

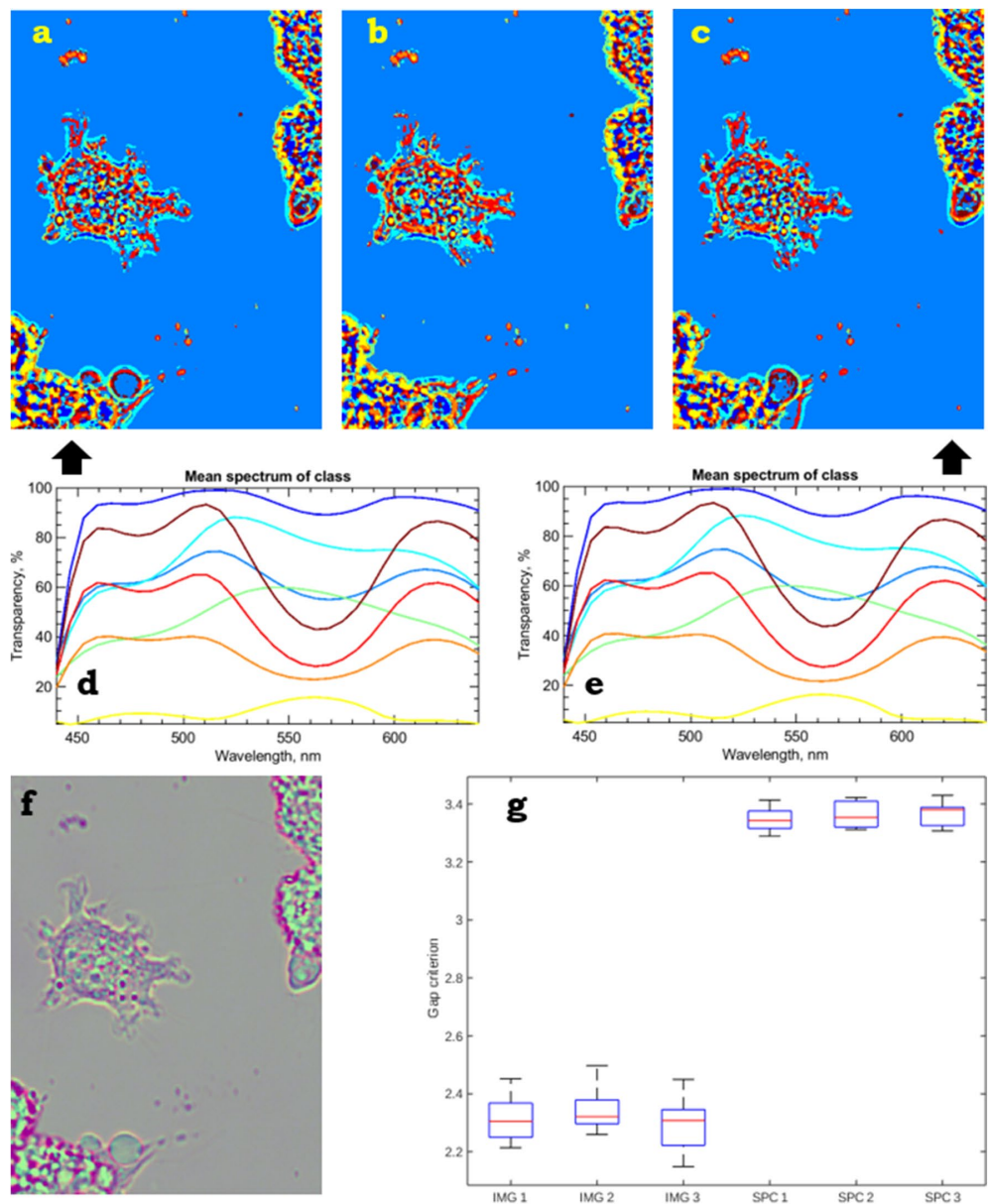


Figure 5. A live cell L929 in time lapse (a–c) at k -means clusterization, $k = 10$. The corresponding mean spectra of classes for images (a,c) are shown in (d,e). These spectra are pretty much similar, despite the different images. The gap criteria for the raw data and the relevant spectral counterparts are presented in (g). Dimensionality reduction techniques, e.g., PCA, can be used for better visualization and digital staining (f).

stopped if the value of change is 0.01. We have not investigated the reason for this course deeply, but it is definitely repeatable for all the tested measurements (e.g., Fig. S3b,c). A natural way of visual verification of an image of transparency spectra is artificial illumination. We used a spectrum of the black body at $T = 5800$ K according to the Planck Law (Figs. 4c, S3a). The transformed image is quite similar to the raw data, which supports the method validity. To obtain such an image, we multiplied each pixel's transparency spectra by the illumination spectrum and the CIE standard matching curves. The integrals of the corresponding curves gave coordinates in the CIE 1931 colour space.

Evaluation of the asset of the proposed method of the quasi-spectral reconstruction (Fig. 5a–e) for clusterization against the raw data is quite tricky, because we have no ground truth. But, nevertheless, there are numerous methods of quality estimation for unsupervised learning²⁴. Such methods are usually used for determination of

the optimal number of clusters in datasets. Our aim is slightly different—to compare the accuracy of the clusterization for two datasets with different dimensionality. This naturally yields a choice of metric—cosine—since this metric is normalized and not affected by magnitude to such an extent as the Euclidean metric. Another fact that can be utilized from the data is that each single image provides 10^5 – 10^6 points. It enables us to use a distribution-based method for estimation of clustering accuracy. One of the most general method from this family is gap statistics²⁵, which is reported to perform well and robust even on noisy data, if a sufficient number of samples is present²⁴. As the clusterization method itself, we used *k*-means with 10 clusters and the cosine metric. Figure 5g shows gap criteria for time-lapse raw images and relevant spectral counterparts. The proposed method leads to better and more stable clustering concurrently. We also investigated different dimensionality reduction techniques (namely PCA¹⁹, Factor Analysis²⁶, and NNM²⁷), which can be applied before the clustering, but these techniques did not bring any improvement in cluster quality. Despite that, these techniques can be used, e.g., for digital staining and highlighting the details in objects, see Fig. 5f.

In order to verify the benefits of the clusterization of the obtained spectra using *k*-means against the direct image clusterization, simple phantom experiments on microphotographs of oil-air and egg protein-air interface, respectively, were conducted. These phantom experiments showed that the spectral clusterization resulted in both a higher cluster accuracy and a lower variation. Moreover, in order to prove the capacity of the method, we applied supervised segmentation, namely a classical semantic segmentation network, U-Net²⁸. It is a symmetric encoder-decoder convolution network with skip connections, designed for pixel-wise segmentation of medical data. One of the strongest advantage of this network is a very low amount of data needed for successful learning (only a few images can be sufficient for this purpose). We employed 6 images for the network training and 1 image for the method validation. To avoid the data overfitting in the training phase, aggressive dropout (0.5, after each convolution layer) and intensive image augmentation (in detail in Suppl. Material 1) was rendered. We compared the performance of the U-Net network for the original raw images, contrast-enhanced images, and spectral images (Fig. 4f). The results of segmentation for the spectral images showed a significantly (> 10%) increased accuracy, intersection over union (IoU) 0.9, and a faster convergence speed (8 epochs vs. 40 epochs for contrast-enhanced images). The results were stable to changes in the training and test sets (even when using a single validation image or a set of augmented images derived from validation as mentioned above).

Discussion

The primary aim of the method is, in the best possible way, to characterize individual cell parts physically (by a colour spectrum) and, consequently, identify them as different cell regions. Currently, the standard approach for the recognition of organelles is fluorescent (or other dye) staining. In unstained cells, identity of an organelle is guessed from its shape and position. Our approach gives the promise to be able to identify the organelles according to their spectra. However, in order to obtain the same spectra for cells of different samples, full reproducibility of the whole experiment such as optical properties of a Petri dish, thickness and colour of cultivation medium has to be ensured.

An important issue that we have not investigated yet is the influence of sample thickness. The question remains what is the identity of the spectrum if the sample has a non-zero thickness. In Rychtáriková et al.¹, we showed that the position of the effective focus differs even with the usage of a fully apochromatic lens. This is the biggest complication in interpreting the spectrum. In case of a relatively thick and homogeneous organelle it can be assumed that, in the centre of the focus, the contribution from geometrically different levels are similar. The full answer to this question would be given by a complete 3D analysis that has to be theoretically based on completely new algorithms and is currently out of the possibilities of our computing capacity. To this point, however, we allow to claim that the thickness of the sample affects mainly the integrals below the spectra, not the shapes of the spectra themselves. The usage of the cosine metric, which is, in effect, the angle between distance vectors and is insensitive to the magnitude, would help to mitigate this problem.

It is worth mentioning that, for some real-life biological samples, the measurement model can be violated. We implicitly assume that light intensity reaching the camera chip is always lower than at the time of its production by a light source. The transparency coefficient is bounded by the range [0, 1]. Indeed, this is not always true because the sample can contain light-condensing objects (most of these objects are bubbles or vacuoles) which act as micro-lenses. It does not break the method generally but, due to inability to fulfil Eq. (2), the local optimization gives an abnormally high cost. Such objects should be eliminated from a subsequent analysis because their quasi-spectra are unreliable. After excluding those dubious regions (which occupy only a very small part of the image, provided they are present at all), the rest of the image can be analysed in an ordinary way.

The obtained quasi-spectra should not be considered as object features but are rather imaging process features. Due to the model-free nature of the method, the obtained classes reflect the observed data, not the internal structures of the objects. We think that the convenient bridge between the observed, phenomenological, spectra and the structure is machine learning, since it shows advantage of enormously good statistics (10^5 – 10^6 samples per image) and compensate influence of the complicated shape.

Conclusions

This novel method of extraction of quasi-spectra aims at a very challenging problem, which cannot be solved precisely even in theory: some information is irrecoverably lost. The method arises from very general assumptions on the measurement system. The method does not rely on any light-media interaction model or physical properties of the system, which makes this method quite universal. The obtained spectra are applicable in practice for visualization and automatic segmentation task. We intentionally did not consider questions of voxel spectrum, Z-stack spectral behaviour, and meaning of the compromised focus in order to keep the method and its application simple. We pose the described method as an ultimate information squeezing tool, which is a

nearly model-free way how to compress the colour and spatial information into representation of the physically relevant features. We believe that, in the future, the method will find its use in robust, mainly qualitative, (bio) chemical analysis.

Microscopy data acquisition

Sample preparation. A L929 (mouse fibroblast, Sigma-Aldrich, cat. No. 85011425) cell line was grown at low optical density overnight at 37 °C, 5% CO₂, and 90% RH. The nutrient solution consisted of DMEM (87.7%) with high glucose (> 1 g L⁻¹), fetal bovine serum (10%), antibiotics and antimycotics (1%), L-glutamine (1%), and gentamicin (0.3%); all purchased from Biowest, Nuaillé, France).

Cells fixation was conducted in a tissue dish. The nutrient medium was sucked out and the cells were rinsed by PBS. Then, the cells were treated by glutaraldehyde (3%) for 5 min in order to fix cells in a gentle mode (without any substantial modifications in cell morphology) followed by washing in phosphate buffer (0.2 mol L⁻¹, pH 7.2) two times, always for 5 min. The cell fixation was finished by dewatering the sample in a concentration gradient of ethanol (50%, 60%, and 70%) when each concentration was in contact with the sample for 5 min.

The time-lapse part of the experiment was conducted with living cells of the same type.

Bright-field wide-field videoenhanced microscopy. The cells were captured using a custom-made inverted high-resolved bright-field wide-field light microscope enabling observation of sub-microscopic objects (ICS FFPW, Nové Hradý, Czech Republic)¹. The optical path starts by two Luminus CSM-360 light emitting diodes charged by the current up to 5000 mA (in the described experiments, the current was 4500 mA; according to the LED producer, the forward voltage was 13.25 V which gave the power of 59.625 W) which illuminate the sample by series of light flashes (with the mode of light 0.2261 s–dark 0.0969 s) in a gentle mode and enable the videoenhancement²⁹. The microscope optical system was further facilitated by infrared 775 nm short-pass and ultraviolet 450 nm long-pass filters (Edmund Optics). After passing through a sample, light reached an objective Nikon (in case of the live cells, CFI Plan Achromat 40×, N.A. 0.65, W.D. 0.56 mm; in case of the fixed cells, LWD 40×, Ph1 ADL, ∞/1.2, N.A. 0.55, W.D. 2.1 mm). A Mitutoyo tubus lens (5×) and a projective lens (2×) magnify and project the image on a JAI camera with a 12-bpc colour Kodak KAI-16000 digital camera chip of 4872 × 3248 resolution (camera gain 0, offset 300, and exposure 293.6 ms). At this total magnification, the size of the object projected on the camera pixel is 36 nm. The process of capturing the primary signal was controlled by a custom-made control software. The z-scan was performed automatically by a programmable mechanics with the step size of 100 nm.

Microscopy image data correction and visualization. The acquired image data were corrected by simultaneous calibration of the microscope optical path and camera chip as described in Suppl. Material 1. In this way, we obtained the most informative images on spectral properties of the observed cells.

For visualization, very bright pixels which correspond to light-focusing structures in the sample (mostly bubbles that act as micro-lenses) and violate the assumptions of the model of the proposed quasi-spectral method were detected (as 99% percentile of intensities) and treated as saturated. After their elimination, the rest of intensities was rescaled to the original range.

Data availability

The software for quasi-spectral characterization of images, the relevant Matlab codes, the software for image calibration, the U-Net segmentation package, and testing images are available in the supplementary materials at the Dryad Data Depository³⁰.

Received: 24 September 2019; Accepted: 12 October 2020

Published online: 27 October 2020

References

- Rychtáriková, R. *et al.* Super-resolved 3-d imaging of live cells organelles' from bright-field photon transmission micrographs. *Ultramicroscopy* **179**, 1–14 (2017).
- Lindner, M., Shotan, Z. & Garini, Y. Rapid microscopy measurement of very large spectral images. *Opt. Express* **24**, 9511 (2016).
- Heist, S. *et al.* 5D hyperspectral imaging: fast and accurate measurement of surface shape and spectral characteristics using structured light. *Opt. Express* **26**, 23366 (2018).
- Wu, J. *et al.* Snapshot hyperspectral volumetric microscopy. *Sci. Rep.* **6**, 24624 (2016).
- Wachman, E. S. *et al.* Simultaneous imaging of cellular morphology and multiple biomarkers using an acousto-optic tunable filter-based bright field microscope. *J. Biomed. Opt.* **19**, 056006 (2014).
- Dahlberg, P. D. *et al.* A simple approach to spectrally resolved fluorescence and bright field microscopy over select regions of interest. *Rev. Sci. Instrum.* **87**, 113704 (2016).
- Zhu, S., Gao, L., Zhang, Y., Lin, J. & Jin, P. Complete plenoptic imaging using a single detector. *Opt. Express* **26**, 26495 (2018).
- Garini, Y., Young, I. T. & McNamara, G. Spectral imaging: principles and applications. *Cytometry A* **69A**, 735–747 (2006).
- Maloney, L. T. Evaluation of linear models of surface spectral reflectance with small numbers of parameters. *J. Opt. Soc. Am. A* **3**, 1673 (1986).
- Parmar, M., Lansel, S. & Wandell, B. A. Spatio-spectral reconstruction of the multispectral datacube using sparse recovery. In *2008 15th IEEE International Conference on Image Processing (IEEE, 2008)*.
- Wang, Y., Yang, B., Feng, S., Pessino, V. & Huang, B. Multicolor fluorescent imaging by space-constrained computational spectral imaging. *Opt. Express* **27**, 5393 (2019).
- Alvarez-Gila, A., van de Weijer, J. & Garrote, E. Adversarial networks for spatial context-aware spectral image reconstruction from RGB. In *2017 IEEE International Conference on Computer Vision Workshops (ICCVW)* (IEEE, 2017).
- Hoover, E. E. & Squier, J. A. Advances in multiphoton microscopy technology. *Nat. Photon.* **7**, 93–101 (2013).
- Lugagne, J.-B. *et al.* Identification of individual cells from z-stacks of bright-field microscopy images. *Sci. Rep.* **8**, 11455 (2018).

15. Velleman, D. J. The generalized Simpson's rule. *Am. Math. Monthly* **112**, 342 (2005).
16. Kuzmin, Y. P. Bresenham's line generation algorithm with built-in clipping. *Comput. Graph. Forum* **14**, 275–280 (1995).
17. Canny, J. A computational approach to edge detection. *IEEE Trans. Pattern Anal. Mach. Intell.* **PAMI-8**, 679–698 (1986).
18. Elboher, E. & Werman, M. Efficient and accurate Gaussian image filtering using running sums. In *2012 12th International Conference on Intelligent Systems Design and Applications (ISDA)* (IEEE, 2012).
19. Pearson, K. On lines and planes of closest fit to systems of points in space. *Lond. Edinb. Dublin Philos. Mag. J. Sci.* **2**, 559–572 (1901).
20. Hair, J., Black, W., Babin, B. & Anderson, R. *Multivariate Data Analysis* (Cengage Learning EMEA, 2018). https://www.ebook.de/product/33402106/university_of_south_alabama_joseph_hair_william_black_barry_louisiana_tech_university_babin_rolph_drexel_university_anderson_multivariate_data_analysis.html.
21. Hansen, N. & Ostermeier, A. Completely derandomized self-adaptation in evolution strategies. *Evol. Comput.* **9**, 159–195 (2001).
22. Hansen, N. The CMA evolution strategy: a comparing review. In *Towards a New Evolutionary Computation* (eds Lozano, J. et al.) 75–102 (Springer, Berlin Heidelberg, 2007).
23. Pech-Pacheco, J., Cristobal, G., Chamorro-Martinez, J. & Fernandez-Valdivia, J. Diatom autofocusing in brightfield microscopy: a comparative study. In *Proceedings 15th International Conference on Pattern Recognition. ICPR-2000* (IEEE Comput. Soc., 2002).
24. Mekaroonkamon, T. & Wongsas, S. A comparative investigation of the robustness of unsupervised clustering techniques for rotating machine fault diagnosis with poorly-separated data. In *2016 Eighth International Conference on Advanced Computational Intelligence (ICACI)* (IEEE, 2016).
25. Tibshirani, R., Walther, G. & Hastie, T. Estimating the number of clusters in a data set via the gap statistic. *J. R. Stat. Soc. B* **63**, 411–423 (2001).
26. Stephenson, W. Technique of factor analysis. *Nature* **136**, 297 (1935).
27. Lee, D. D. & Seung, H. S. Learning the parts of objects by non-negative matrix factorization. *Nature* **401**, 788–791 (1999).
28. Ronneberger, O., Fischer, P. & Brox, T. U-net: convolutional networks for biomedical image segmentation. In *Medical Image Computing and Computer-Assisted Intervention - MICCAI 2015* (eds Navab, N. et al.) 234–241 (Springer International Publishing, Cham, 2015).
29. Lichtscheidl, I. K. & Foissner, I. Video microscopy of dynamic plant cell organelles: principles of the technique and practical application. *J. Microsc.* **181**, 117–128 (1998).
30. Lonhus, K., Rychtáriková, R., Platonova, G. & Štys, D. Supplementary to *Quasi-spectral characterization of intracellular regions in bright-field light microscopy images. Dryad Dataset*. <https://doi.org/10.5061/dryad.w0vt4b8p6>.

Acknowledgements

This work was supported by the Ministry of Education, Youth and Sports of the Czech Republic—project CENAKVA (LM2018099)—and from the European Regional Development Fund in frame of the project Kompetenzzentrum MechanoBiologie (ATCZ133) and Image Headstart (ATCZ215) in the Interreg V-A Austria–Czech Republic programme. The work was further financed by the GAJU 013/2019/Z project.

Author contributions

K.L. is the main author of the paper and of the novel algorithm, G.P. and R.R. are responsible for sample preparations, microscopy data acquisition, and image calibration, R.R. contributed to the text of papers substantially, D.Š. is an inventor of the videoenhanced bright-field wide-field microscope. D.Š. and R.R. lead the research. All authors read the paper and approved its final version.

Competing interests

The authors declare no competing interests.

Additional information

Supplementary information is available for this paper at <https://doi.org/10.1038/s41598-020-75441-7>.

Correspondence and requests for materials should be addressed to K.L.

Reprints and permissions information is available at www.nature.com/reprints.

Publisher's note Springer Nature remains neutral with regard to jurisdictional claims in published maps and institutional affiliations.



Open Access This article is licensed under a Creative Commons Attribution 4.0 International License, which permits use, sharing, adaptation, distribution and reproduction in any medium or format, as long as you give appropriate credit to the original author(s) and the source, provide a link to the Creative Commons licence, and indicate if changes were made. The images or other third party material in this article are included in the article's Creative Commons licence, unless indicated otherwise in a credit line to the material. If material is not included in the article's Creative Commons licence and your intended use is not permitted by statutory regulation or exceeds the permitted use, you will need to obtain permission directly from the copyright holder. To view a copy of this licence, visit <http://creativecommons.org/licenses/by/4.0/>.

© The Author(s) 2020

■ **Super-resolved 3-D imaging of live cells' organelles from bright-field photon transmission micrographs**

R. Rychtáriková, T. Náhlík, K. Shi, D. Malakhova, P. Macháček, R. Smaha, J. Urban a D. Štys, *Super-resolved 3-D imaging of live cells' organelles from bright-field photon transmission micrographs*, *Ultramicroscopy* **179** (2017), 1–14.

Tato publikace je výchozí prací ÚKS FROV JU v oblasti buněčné mikroskopie a popisuje komplexní přístup ke světelné mikroskopii neznačené živé buňky od konstrukce mikroskopu po obrazovou analýzu. Tímto článkem jsme pravděpodobně získali světovou prioritu v konstrukci trojrozměrného časoprostorového modelu neznačené buňky z transmisní světelné mikroskopie.

Časopis *Ultramicroscopy* održel dle WoS v oboru Mikroskopie pro rok 2017 rank 1. Článek byl vybrán vydavatelstvím Elsevier mezi 30 fyzikálních článků k další propagaci, což se stalo podnětem pro vydání tiskové zprávy FROV JU z 24. září 2017 s cca 15 mediálními výstupy včetně ČT.



Super-resolved 3-D imaging of live cells' organelles from bright-field photon transmission micrographs



Renata Rychtáriková^{a,*}, Tomáš Náhlík^a, Kevin Shi^b, Daria Malakhova^a, Petr Macháček^a,
Rebecca Smaha^c, Jan Urban^a, Dalibor Štýs^a

^aInstitute of Complex Systems, Faculty of Fisheries and Protection of Waters, University of South Bohemia, Zámek 136, 373 33 Nové Hradky, Czech Republic

^bPrinceton University, Princeton, New Jersey 08544, USA

^cDepartment of Chemistry, Stanford University, Stanford, California 94305, USA

ARTICLE INFO

Article history:

Received 11 February 2016

Accepted 15 March 2017

Available online 18 March 2017

Keywords:

Super-resolution
Bright-field microscopy
Light transmission
Live cell imaging
3D

ABSTRACT

Current biological and medical research is aimed at obtaining a detailed spatiotemporal map of a live cell's interior to describe and predict cell's physiological state. We present here an algorithm for complete 3-D modelling of cellular structures from a z-stack of images obtained using label-free wide-field bright-field light-transmitted microscopy. The method visualizes 3-D objects with a volume equivalent to the area of a camera pixel multiplied by the z-height. The computation is based on finding pixels of unchanged intensities between two consecutive images of an object spread function. These pixels represent strongly light-diffracting, light-absorbing, or light-emitting objects. To accomplish this, variables derived from Rényi entropy are used to suppress camera noise. Using this algorithm, the detection limit of objects is only limited by the technical specifications of the microscope setup—we achieve the detection of objects of the size of one camera pixel. This method allows us to obtain 3-D reconstructions of cells from bright-field microscopy images that are comparable in quality to those from electron microscopy images.

© 2017 Elsevier B.V. All rights reserved.

1. Introduction

Bright-field microscopy is a classical method, favored for its convenience and ability to observe the physiology and morphology of unlabelled living cells and tissues. It avoids potentially complicated sample preparation procedures and visual artifacts due to complex optical paths and, in addition, is non-destructive. However, the main issue that hinders the segmentation and analysis of bright-field microscopy images [1–8] is the low contrast of structures in the focal plane caused by distortions from an object spread function (OSF), which is unknown for most objects. These distortions are particularly relevant in a biological context, as biological specimens are significantly thicker than the depth-of-field of typical bright-field microscope lenses [9] and also have particular physicochemical properties that lead to optical inhomogeneities and further complicate the OSF. Its analysis is in addition complicated by the dynamic nature of living cells, which causes spatiotemporal changes in the image. Finally, the discretization performed during image capture may also produce inaccuracies. The resulting standard bright-field microscopy image represents multiple processes and exhibits a multifractal character.

These issues impose several constraints on the type of algorithm and microscope appropriate for this task:

1. It is necessary to obtain the most real and natural images possible in order to discover the spectral properties of a cell's spread function. This can be carried out using a high-resolution camera equipped with an image sensor overlaid with a Bayer filter, capturing RAW files in a higher-bit colour depth and processing them using a non-interpolating algorithm [10,11]. Precise microscope mechanics should ensure the smallest possible movement along the z-axis.
2. The analytical method must be able to recognize spontaneous and random processes that underlie self-organization and multifractality [12]. Extracting the information from an image using Rényi entropy [13] parametrized by α ($\alpha \geq 0$ and $\alpha \neq 1$) serves as an appropriate basis for this task.
3. The method must be sensitive to diffraction, which is the main interactive process between light and cellular structures. Properties of the light wavefront that arises from diffraction and is projected at the objective lenses are described in full by Mie scattering theory [14]. Under the condition that the size of a particle is much larger than the wavelength of light, ray tracing techniques (geometry optics) provide a sufficient model for the characterization of the shape of the particle. Then, the behaviour of light at the

* Corresponding author.

E-mail address: rnychtarikova@frov.jcu.cz (R. Rychtáriková).

Table 1
Microscope setup.

Cell	Series			Camera			Piezo ^a
	Number of img. ^b	Step (nm)	Time (min:s)	Offset	Gain	Exposure (ms)	
MG63- a	93 (155)	119	03:35.4	0	268	3327	Yes
MG63- b	128 (201)	150	10:22.7	266	347	2466	No
L929	173 (358)	158	11:09.0	221	336	2632	No

^a If yes, the image series underwent image alignment (registration).

^b The original number of image in the series before z-step selection is parenthesized.

interface of the strong diffracting object can be described by the phenomenon of total external light reflection and diffraction (**Supplementary Fig. 1b**).

- The method must recognize the focus of the cell in its spread function. According to the Extended Nijboer-Zernike (ENZ) theory [15–17], the focus of a fluorescent and light-diffracting object is located at the position of the highest and lowest energy density, respectively (**Supplementary Fig. 1a**).

Here, we demonstrate a novel mathematical approach to reach superresolution in bright-field microscopy. This method, validated using atomic force microscopy, was applied to 3-D reconstructions and spectral and dynamic analysis of organelles and OSFs from z-stacks of bright-field microscopy images of live mammalian cells.

2. Results

The method is demonstrated on two cells of MG-63 human osteosarcoma (labelled **a** and **b**) from different cultivation batches and a cell of L929 mouse adipose tissue; the z-stacks of 12-bit bright-field microscopic RAW files were collected with an average z-step of 119, 150, and 158 nm, respectively. The detailed scanning conditions are described in **Table 1**. The z-stacks underwent image pre-processing such as vertical image registration (the MG63-**a** cell) and the removal of defective (dead and hot) camera pixels (the MG63-**b** and L929 cells) to avoid image defects, which, in addition, demonstrates the robustness of the method.

The overall preview of the image processing of the z-stack of the input data—12-bit RAW files with a cell of interest and background—with respect to the items mentioned above is shown in **Fig. 1a** and discussed in detail in the following sections.

2.1. Segmentation of a cell's focal region

In the first step, a cell of interest was segmented from its background by identifying green pixels whose intensities remain unchanged for each two consecutive RAW files (**Algorithm 1, Fig. 1b**). The intensities of the green pixels in each Bayer mask quadruplet were averaged to give quarter-resolved grayscale images [10,11], which were then subtracted. The unchanged intensities (i.e. zero values in the differential image) concurrently higher than 0 and lower than a 0.95-fold intensity mode of the cell-free second image contributed to the cumulative binary mask. In the focal region, these unchanged dark green pixels are the primary contributors to the cumulative binary mask (**Supplementary video 1**).

This binary mask was further processed by standard morphological operations—dilating the image (a 3 pixels disk-shaped structuring element), filling image holes (corresponding, in the original image, to the fluorescent objects and positive light interferences in the Airy diffraction pattern [18]), and filtering the cell of interest according to its specific features (in our case, as an object of the maximal size)—resulting in a final binary mask. The final binary mask of the cell was rescaled by a factor of two and applied to the whole z-stack of the original RAW files in order to distinguish a sum of point spread functions of the cell.

Computation of the binary mask from RAW files' red and blue pixels did not give the desired results. Due to the high frequency of consecutive pixels with constant intensities, the image of the cell merged with its background. The reason for this may be found either in light absorption in the infra-red and ultra-violet regions [19] or in lower photon quantum efficiency of the respective camera filters [20]. Therefore, in all segmentations, the green intensity wide range histogram was used.

The next step consists of selecting the focal sub-stack of the cell and assessing cell topography. The focal region of the z-stack was determined via clustering point information gain entropy density (Ξ_α) spectra [21] obtained for all RAW files of the separated cell. The variable Ξ_α [bit] was derived from the Rényi entropy as

$$\Xi_{\alpha,l} = \frac{1}{1-\alpha} \sum_{j=1}^k \log_2 \frac{\sum_{i=1}^k p_{j,i,l}^\alpha}{\sum_{j=1}^k p_{j,l}^\alpha}, \quad (1)$$

where p_j and $p_{j,i}$ are the probabilities of occurrence of intensity j in an intensity histogram of the l th image in the z-stack with and without an element of the intensity i , respectively. The additive term $\frac{1}{1-\alpha} \log_2 \frac{\sum_{i=1}^k p_{j,i,l}^\alpha}{\sum_{j=1}^k p_{j,l}^\alpha}$ is called a point information gain ($\Gamma_{\alpha,j}$, bit) and can determine an information contribution of intensity j to the intensity histogram obtained from either the whole image (a global measure $\Xi_{\alpha,Wh}$) or its part (local measures). For image processing of the presented cells, we used local values evaluated from pixels either on the vertical-horizontal cross ($\Xi_{\alpha,Cr}$) or on a 9 pixels circle around the examined pixel ($\Xi_{\alpha,Circle}$). The kind of local information was chosen according to the distribution of intensities in the image. Whereas the z-stacks of the MG63-**a** and L929 cells suffered from cross camera noise, the images of the MG63-**b** cell did not (**Supplementary videos 2 and 3**). In the latter case, the 9 pixels circular type of surroundings approximately traced the borders of intracellular structures.

For the overall multifractal characterization of the images, Ξ_α -spectra were calculated for a set of $\alpha = \{0.1, 0.3, 0.5, 0.7, 0.99, 1.3, 1.5, 1.7, 2.0, 2.5, 3.0, 3.5, 4.0\}$, for each colour channel separately. While the values $\Gamma_{\alpha,j}$, and consequently $\Xi_{\alpha,j}$, for the red and blue channels (indexed R and B , respectively) were computed by eliminating one element of intensity j from the respective intensity histogram, these values for the green pixels (indexed G) were obtained via eliminating two elements that were relevant to the intensities of the Bayer mask quadruplet.

Matrices composed of vectors that specify each image l in the z-stack via α -dependent subvectors of the respective information content in the respective colour channel, i.e.

$$\Xi_{(l)} = [\Xi_{\alpha,Wh,R}, \Xi_{\alpha,Wh,G}, \Xi_{\alpha,Wh,B}, \Xi_{\alpha,Cr,R}, \Xi_{\alpha,Cr,G}, \Xi_{\alpha,Cr,B}] \quad (2)$$

for series of the MG63-**a** and L929 cells and

$$\Xi_{(l)} = [\Xi_{\alpha,Wh,R}, \Xi_{\alpha,Wh,G}, \Xi_{\alpha,Wh,B}, \Xi_{\alpha,Cr,R}, \Xi_{\alpha,Cr,G}, \Xi_{\alpha,Cr,B}, \Xi_{\alpha,Circle,R}, \Xi_{\alpha,Circle,G}, \Xi_{\alpha,Circle,B}] \quad (3)$$

for the series of the MG63-**b** cell, were standardized with z-scores and underwent k-means clustering (squared Euclidean distance metric, 50 iterations) into two groups (**Algorithm 2**). Due to the

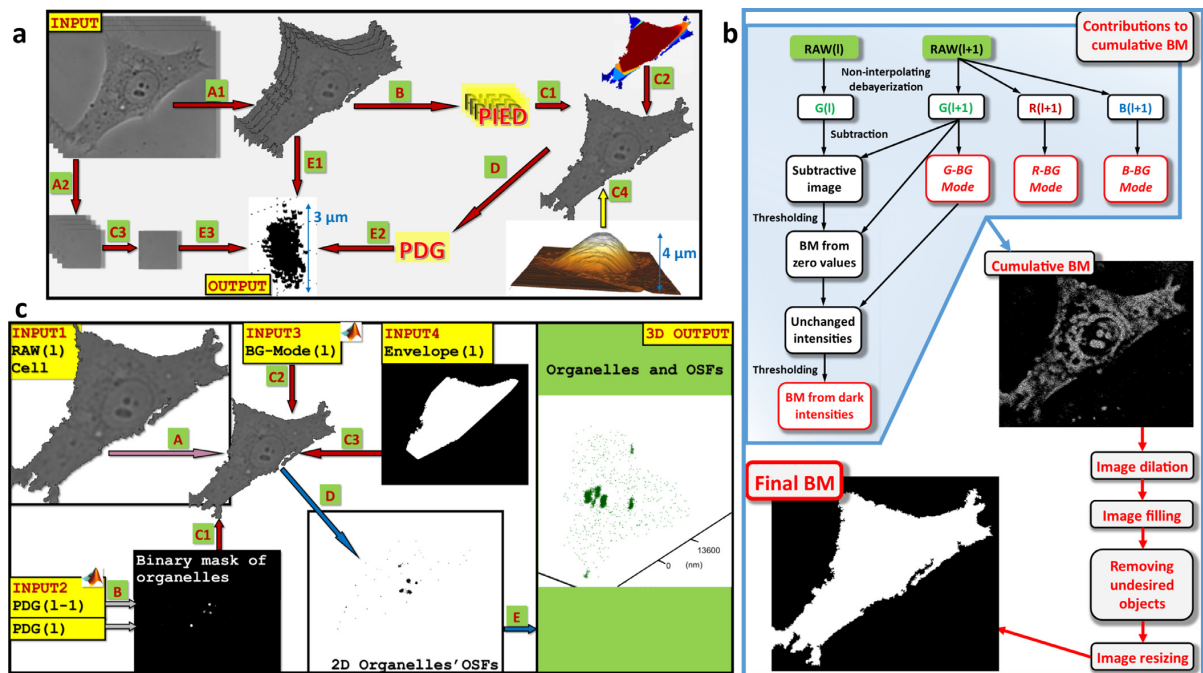


Fig. 1. Scheme of the algorithm for 3-D reconstruction of organelles inside a live cell from bright-field photon microscopy (illustrated on stable homogenous diffracting organelles inside the MG63-a cell). (a) Total overview of the algorithm. **A1** – 2-D cell segmentation from the original input z-stack images (in 12-bit RAW files, Algorithm 1); **B** – calculating $\Xi_{\omega,c}$ (PIED) spectra, where c is a colour channel, for each z-stack image; **C1** – selection of the focal region of the z-stack according to $\Xi_{\omega,c}$ -spectra (Algorithm 2); **C2** – calculation of the cell topography (Algorithm 3); **C4** – comparison of the z-stack region with the AFM profile of the cell (Supplementary Fig. 4); **D** – calculating $\omega_{\alpha,l,x,y,c}$ values from two consecutive z-stack images; **A2**, **G**-, and **B**-intensity histograms, respectively; **C3** – selection of background values in the focal plane (complementary to the image of the cell in the focal region); **E1, E2, E3** – 3-D organelle segmentation and reconstruction (the output of Algorithm 4) from the focal region of the cell, including its $\omega_{\alpha,l,x,y,c}$ -images and background values. (b) Detailed scheme of the cell segmentation (**A1** process in panel a, Algorithm 1). (c) Detailed scheme of organelle segmentation (Algorithm 4). **A** – non-interpolating demosaicing of the RAW files of the segmented cell (input 1); **C2** – removing undesirable objects via comparison of the cell intensity histogram with the mode of the background histogram (input 3); **C3** – application of the binary topological envelope (input 4) to each z-stack; **B** – creation of a binary mask via overlapping of $\omega_{\alpha,l,x,y,G} = 0$ values from two consecutive images; **C1** – 2-D segmentation of organelles and OSFs; **D** – 3-D reconstruction of organelles; **E** – 3-D stacking of 2-D organelle segments. Image processing was performed in 12-bit intensity depth and is visualized in 8 bit.

spectral properties of the OSF, this clustering properly selected a focal region of the cell from the rest of the z-stack.

In Algorithm 2, the sub-stack of the focal region was chosen as a cluster with a RAW file whose average intensity of green pixels is the inflection point of the dependence of the average intensity of green pixels on the position of the RAW file in the z-stack. To smooth the dependence, a fourth-order polynomial was used. This part of the algorithm assumes that in the focal region the intensities over the z-stack change significantly, whereas the intensities of blurred images remain relatively constant.

The topological envelope of the cell (explained as a binary image at each z-level, Algorithm 3) was evaluated from the focal sub-stack of RAW files as the absolute value of the subtraction of the unblurred and blurred green pixels at the same z-level after non-interpolating de-mosaicing of green pixels of RAW files. The blurring of each particular image was performed with a filter created from a 10 pixels disk-shaped structural element. After that, the pixels of interest at each z-level were chosen as those brighter than twelve times the maximal intensity of the subtracted image. These pixels underwent a morphological closing (a 3 pixels disk-shaped structuring element), removing the undesirable pixels via morphological erosion and dilation, and computation of the binary convex hull around the rest of the binary objects. A subsequent dilation of the binary convex hull (a 20 pixels disk-shaped structuring element) ensured extension and rounding of the cell boundaries.

From each series, a multiplication of the number of images in the focal region by the respective average scanning step (Table 3) gave us a height of the part of the OSF that is occupied by the cell, i.e. 5.6, 3.6, and 5.4 μm for the MG63-a, MG63-b, and L929 cells, respectively. The shapes and the heights of the cells (Fig. 3b and Supplementary Figs. 2 and 3b) obtained from the bright-field microscopy images using the presented algorithm are in agreement with live cell imaging using atomic force microscopy [22] (Supplementary Fig. 4 and Supplementary information 1). In the MG-63 cell line, hill-shaped cells with a protuberant nuclei, of the size of 5.2 ± 1.1 and 4.0 ± 1.0 μm on different substrates, prevail. L929 cells are approximately 0.4 μm lower and flatter. Similar results have been depicted in scanning microscopy images and described in literature [23–26]. For the microscopy experiments, the dish bottoms were not treated.

2.2. Classification, segmentation, and investigation of properties of organelles

This section describes how to extract information about the 3-D shapes and dynamics of organelles from a focal region of a z-stack of bright-field optical transmission micrographs of a detached cell. The sub-stacks of the MG63-a, MG63-b, and L929 cells were obtained with average z-step sizes of 116, 156, and 147 nm and with a scanning frequency of 0.440, 0.213, and 0.298 img. s^{-1} , respectively (Table 3).

Algorithm 1

creating a binary mask to segment a cell of interest from a bright-field optical transmission z-stack.

INPUT:

n RAW files of with cell of interest;
x1, x2, y1, y2 as coordinates of the background region;
c1 as a threshold constant of the background (**c1** = 0.95);
c2 as a size of the structural image dilating element (**c2** = 3);
BM as a zero matrix of the quarter size than the RAW file

OUTPUT:

CellBM as a binary mask of the cell of interest

```

for i = 1:(n-1)
    raw1 = readIm(i);
    raw2 = readIm(i+1);
        % read the (i)th and (i+1)th RAW file , respectively
    G1 = demosaicG(raw1);
    G2 = demosaicG(raw2);
        % create a quarter-resolved image by averaging two green pixels of
        each Bayer mask's quadruplet in the (i)th and (i+1)th RAW file ,
        respectively
    m = findMode(G2(x1:x2, y1:y2));
        % find the intensity mode of the background in the (i+1)th image

```

In order to maximize and analyze the change in the OSF's volume, we have previously derived a information-entropic variable point divergence gain [10] (PDG: $\omega_{\alpha,l,x,y,c}$, bit), which evaluates the information divergence for all pixels between two consecutive RAW files in the focal section of the z-stack:

$$\omega_{\alpha,l,x,y,c} = \frac{1}{1-\alpha} \log_2 \frac{\sum_{j=1}^k p_{i,l,c}^{\alpha}}{\sum_{j=1}^k p_{i,(l+1),x,y,c}^{\alpha}}, \quad (4)$$

where l is the order of an image in the focal region of the z-scan, and x and y are coordinates of the particular pixel in the image l . Probabilities $p_{i,l,c}$ and $p_{i,(l+1),x,y,c}$ describe the frequencies of occurrence of colour intensities in the image (l) and in the same image after exchanging the pixel at coordinates (x, y, l) for the pixel at $(x, y, (l+1))$. The $\omega_{\alpha,l,x,y,c}$ -values for pixels of each colour in the RAW file's quadruplet were calculated in the same way as the Ξ_{α} -values in Eq. (4): red and blue channels of the resulting quarter-resolved $\omega_{\alpha,l,x,y,R/B}$ -matrices were computed after exchanging one pixel of the respective colour, whereas the green channel was obtained after exchanging two green pixels of the respective pixel quadruplet.

Compared to the simple subtraction of two consecutive images, calculating $\omega_{\alpha,l,x,y,c}$ -values classifies the image pixels with respect to their probability of occurring in volume and also introduces dynamics into the examined system. Zero values of $\omega_{\alpha,l,x,y,c}$ correspond to pixels with relatively high occurrences in the image, and thus ones that do not change in a z-step. These represent stable, large, non-moving objects at a high image resolution and the smallest possible z-step, mainly organelles down to the size of one voxel. The more extremely negative or positive values of $\omega_{\alpha,l,x,y,c}$ show pixels with the highest change from image to image, which correspond mainly to moving objects. Other $\omega_{\alpha,l,x,y,c}$ -values detect either sums of point spread functions of organelles or organelles themselves, which are composed of lower-occurrence intensities at the given z-level and, concurrently, whose OSFs are divergent over distances smaller than the size of the z-step.

Here, coefficient α represents multifractality and defines distribution. Low values of α merge frequently-occurring $\omega_{\alpha,l,x,y,c}$ -values and separate rare pixels—the most dynamic organelles in this case. High α values give wider distributions of $\omega_{\alpha,l,x,y,c}$ -values. A suitable value of this parameter must be always derived or estimated with regards to the multifractal character of the given

intensity distribution. We decided to use α equal to 5 (MG63-a) and 6 (MG63-b, L929), at which value the images of the organelles' OSFs, mainly in the green channel, are adequately condensed after camera noise and another defects in the image are suppressed (Figs. 2a, 3c, and **Supplementary Figs. 2 and 3a**). At zero $\omega_{\alpha,l,x,y,c}$ of a higher-order α , we already observe a strong combination of intensities of light-interferences in the image. As the size of the z-step increases, larger α -values must be used to merge the correct image intensities.

Analysis of $\omega_{\alpha,l,x,y,c}$ -values in each colour channel showed that there is mainly autofluorescence projected in the blue channel. The

green channel further displays diffraction. The red channel shows also the contribution of near infra-red absorption. The application of each colour channel can be viewed when zero $\omega_{\alpha,l,x,y,c}$ -values are compared with original images (Fig. 2b) and provide a potential for classification and recognition of organelles with the respect to their composition, without the usage of any labelling technique (cf. [27]).

Because computing $\omega_{\alpha,l,x,y,c}$ -values for three consecutive z-stack images gives information about the shape and dynamics of organelles in the middle image, a binary mask for segmenting objects in a z-level was created by thresholding and uniting

Algorithm 2 selecting the focal region using Ξ_{α} values.

INPUT:

n RAW files of cell of interest;
piEd as a matrix of the size of (number of colour image channels x
 number of alpha) x **n**

OUTPUT:

focReg as a matrix specifying images which belong to the focal region

```

piEd = zscore(piEd);
    % calculate a z-score for each sample (image) spectrum over alphas
idx = cluster(piEd, 2);
    % cluster samples (images) into 2 groups (via k-means algorithm with
    % Euclidian distance) and assign a number of group to each sample (
    % image) into vector idx

    % find a focal plane of the series as the image of the average darkest
    % intensity
averInt = zero(n, 1);
    % create a zero matrix averInt for the storage of RAW files' average G-
    % intensities

for i = 1:n
    rawCell = readIm(i);
    G = demosaicG(rawCell);
    averInt(i) = nonzeroMean(G);
  
```

(continued on next page)

Algorithm 2 (continued)

```

end

% calculate the average intensity of G-channel for each image in the z-
% stack (omit a black background from the calculation)

fitInt = smoothCurve(averInt);

% fit the dependency of average G-intensity on the position in the z-
% stack by a smooth curve (a polynom of order 4)

inflex = findInflexion(fitInt);

% find an inflexion point of the smoothed curve, which corresponds to
% the best focused image in the z-stack

idxInflex = findIdx(idx == inflex);

% find the number of cluster in the idx matrix, which corresponds to the
% image at the position of the inflexion point

focReg = findRegion(idx == idxInflex);

% find the focal region as the number of cluster with the image, which
% corresponds to the inflexion point of the intensity curve

```

identical $\omega_{\alpha,l,x,y,c}$ -values from two consecutive $\omega_{\alpha,l,x,y,c}$ -matrices (input 2 in Fig. 1c). This mask was applied to the respective quarter-resolved image of the cell (input 1 in Fig. 1c), which was obtained by adapting the Bayer quadruplet's pixels of red, blue and average green to the respective colour channel. The subsequent matching of the respective binary topological mask (input 4 in Fig. 1c) with the image of the detached objects selected objects relevant for the given z-level (Algorithm 4).

The last part of the algorithm (input 3 in Fig. 1c) filtered irrelevant intensities from the images, which completely describe the spectral properties of the cell's image. For each colour channel, strongly light-diffracting or absorbing organelles were detached as those darker than the cell-free background. In contrast, light-emitting organelles were reconstructed from intensities brighter than the background (Fig. 1-B1– B3, Algorithm 4).

In this paper, we demonstrate a novel method for 3-D reconstruction and examination of large homogeneous non-moving

cellular objects, which are projected at the most frequent value of $\omega_{\alpha,l,x,y,c} = 0$ (Fig. 3c and **Supplementary Figs. 2 and 3c**). Apart from the large homogeneous non-moving objects (e.g. nucleoli in diffraction), the method detected objects of the size of a few voxels [28], which might be shown to be real objects by video-enhanced microscopy or correspond to other frequent intensities remaining constant through a z-step.

The OSFs of light-diffracting objects are substantially smaller than those of light-emitting objects, which implies that transmission microscopy has an advantage over fluorescent microscopy in biological experiments (**Supplementary Fig. 1a**). The consistently smaller number of detected objects in the green channel is probably caused either by the mathematical averaging of two green pixels of the Bayer mask quadruplet during the calculation of $\omega_{\alpha,l,x,y,c}$ -values or by the broader green spectrum (caused by technical reasons, as noted above) decreasing the probability of occurrence of the same intensity between two consecutive pixels.

Table 2
Image processing of the presented cells.

Cell	Coordinates of background	Selection of focus	3-D imaging	
	x_1, x_2, y_1, y_2	Local Ξ_{α}	α for $\omega_{\alpha,l,x,y,c}$	R, G, B threshold
MG63- a	4, 268, 652, 894	Cross	5	
MG63- b	26, 322, 1296, 1618	Cross, 9 pixels circle	6	1250, 2300, 1500
L929	144, 792, 803, 1268	Cross	6	1000, 1700, 1170

3. Discussion

Knowing the distribution and mutual interactions of biomolecules can help determine the morphological and physiological state of a cell. Since the 17th century [29], observations of intracellular processes have been provided by microscopic techniques based on different physical principles. Imaging based on

fluorescent microscopy has been a leading technique for defining the subcellular location of proteins for decades. However, fluorescent protein tagging technology suffers from some limitations, including the need for a physiological level of light-emitting protein production, mislocalization artifacts, relatively low resolution, and the necessity to intervene in the cell's physiological state after insertion of a dye [30]. The breakage of the Abbe diffraction

Algorithm 3 obtaining the topography.

INPUT:

n RAW files of a cell of interest;
c as a threshold constant (**c** = 12)

OUTPUT:

envelope as a binary matrix with **a** levels of the topological set of the cell

```

BM = resizeIm(logical(readIm(1)), 0.5);
    % create a binary image of the cell, which is of a quarter resolution in
    % comparison to the original image
envelope = zeros(size(BM, 1), size(BM, 2), length(flr));
    % create a zero matrix of the size of the whole z-stack
envelope(:,:,2) = BM;
    % save the binary mask of the original cell into the second layer of the
    % envelope matrix

BM = erodeBW(BM, strel('disk', 10));
    % erode the original binary mask with a structural element (a 10-px disk
    % ) to remove the edges of the cell in a image obtained via a
    % subtraction of the blurred and unblurred input image
BM([1:10, end-10:end], :) = 0;
BM(:, [1:10, end-10:end]) = 0;
    % remove the edges of the bw-image which touch the edges of the picture
for i = 3:n
    rawCell = readIm(i);
    Cell = demosaicG(rawCell); % demosaic a G-channel

```

(continued on next page)

Algorithm 3 (continued)

```

filtCell = filterIm(Cell);
    % filter the image Cell with a circular averaging filter (pillbox of
    % the 10-px radius) to create a blurred image of the cell
difCell = abs(double(Cell) - double(filtCell));
    % calculate absolute values in the image, which is a subtraction of
    % a focal image and its blurred version
cutDifCell = difCell .* double(BM);
    % cut the edges of the cell using a binary mask BM;

thresh = findMax(cutDifCell)/c;
    % calculate a threshold for the selection of the immovable objects
    % as a ratio of the maximal value in the subtractive image
    % cutDifCell and input constant c
thCutDifCell = cutDifCell > thresh;
    % threshold the values in the subtractive image higher than the
    % threshold thresh
closeObjects = closeBW(thCutDifCell);
    % perform image closing (with a 3px disk structural element on the
    % threshold image)
bigObjects = filterObjects(closeObjects);
    % remove small objects in the closed image
envelope(:,: ,i) = uniteObject(bigObjects);
    % unite the rest of objects and create an envelope
envelope(:,: ,i) = envelope(:,: ,i) .* envelope(:,: ,i-1);
    % apply the previous envelope to the current one to make the mask
    % gradually smaller

end

```

limit [31] in fluorescent microscopy was achieved by the invention of super-resolved fluorescent imaging, which was awarded the 2014 Nobel prize in chemistry [32]. On the other hand, contrast techniques in optical microscopy such as phase contrast [33], differential interference contrast [34], digital microscopic holography [38], interferometric microscopy [35], and optical coherence

tomography [36] require the insertion of an optical element into the optical path of the microscope, which distorts the image of the observed biological specimen and makes image interpretation much more difficult. Electron microscopy (in both transmission and scanning modes) is an ancillary method in cell biology [37], since it may only be used to observe dried samples after a prepa-

Table 3
Characterization of the focal regions.

Cell	Coordinates of position x_1, x_2, y_1, y_2	Number of img.	Average step (nm)	z-Height (nm)	Time (min:s)	Img. frequency (s^{-1})
MG63-a	55, 1928, 1, 2278	49	116	5568	1:51.3	0.440
MG63-b	1, 2436, 139, 3248	24	156	3588	1:52.2	0.213
L929	767, 1798, 341, 1432	38	147	5436	2:07.7	0.298

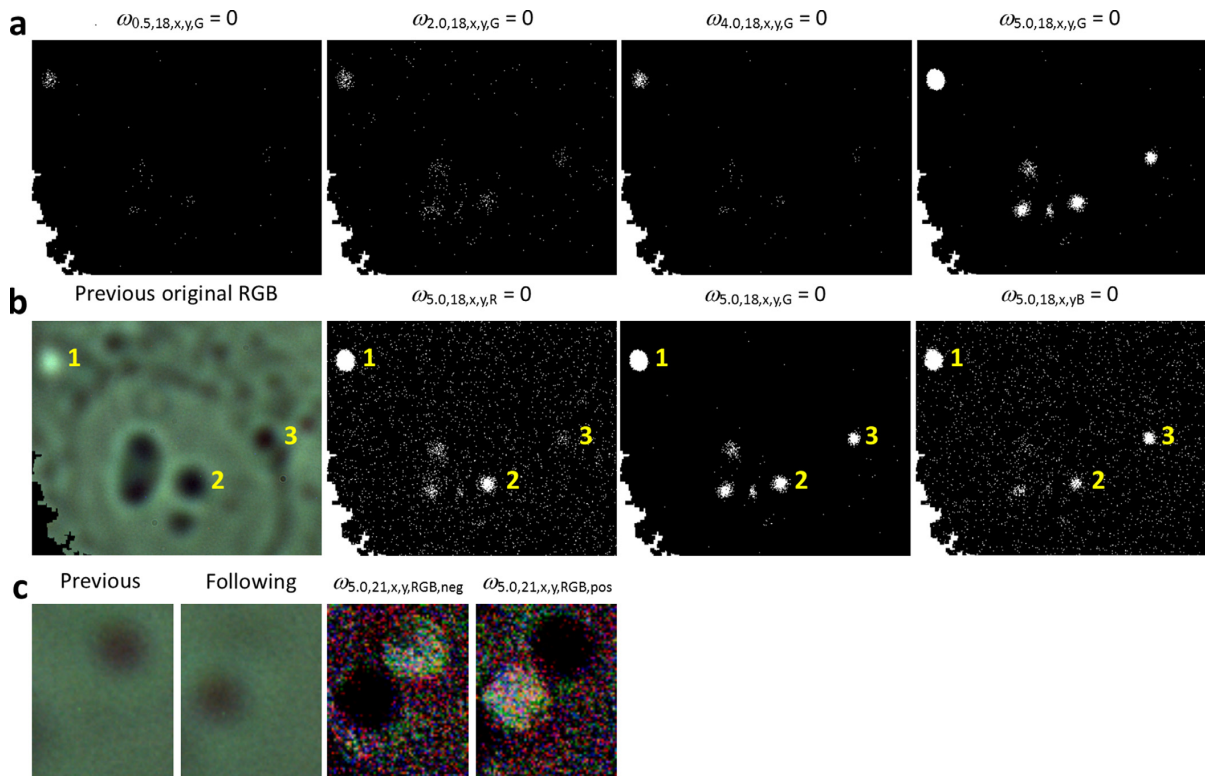


Fig. 2. Details of $\omega_{\alpha,l,x,y,c}$ -images of a focal plane of a z-stack of live cell from bright-field transmission optical microscopy computed using two consecutive images (illustrated on the interior of a MG63-a cell). (a) Zero values of $\omega_{\alpha,l,x,y,c}$ -transformed images with points that show unchanged information at α equal to 0.5, 2.0, 4.0, and 5.0, respectively. The original section of the cell is identical to that of b. (b) An original RGB section of the cell (visualized in 8 bpc) and its values $\omega_{\alpha,l,x,y,c} = 0$ for the red, green, and blue channels. Autofluorescent organelle 1 shows spectral characteristics in all colour channels. Organelle 2 (nucleolus) diffracts in the green and red channels and has weak autofluorescence due to its content of nucleic acids. Organelle 3 bound to the nucleolar envelope is detectable only in the blue and green channels. (c) Movement of an organelle demonstrated on 8-bit images transformed from the original $\omega_{5.0,21,x,y,RGB}$ -values in double precision floating point format (some $\omega_{5.0,l,x,y,RGB}$ -values are merged into one intensity of the $\omega_{5.0,21,x,y,RGB}$ -image). White and black pixels in the $\omega_{5.0,21,x,y,RGB,neg}$ -image (e.g., the highest and the lowest negative $\omega_{\alpha,l,x,y,c}$ -values, respectively) correspond to the position of the organelle in the previous and following original RGB images of the cell, respectively (and vice versa for the $\omega_{5.0,21,x,y,RGB,neg}$ -image). The sizes of the sections in a–b is $23.732 \times 19.176 \mu\text{m}^2$ and $4.352 \times 5.372 \mu\text{m}^2$ in c ($68 \text{ nm}^2 \text{ px}^{-1}$). (For interpretation of the references to colour in this figure legend, the reader is referred to the web version of this article.)

ration time of several days. However, the resolution obtained by electron microscopy may go down to a few nanometers. The newest imaging method—atomic force microscopy, e.g. [39]—is a kind of non-optical topographical technique that reaches high resolution but does not provide the possibility of fully imaging intracellular composition and interactions. Connecting the benefits of these different imaging methods can be achieved by combining them; for instance, correlative light electron microscopy (CLEM, e.g. [40]) is the most well-known and commercially available example of combined imaging.

This article reports a method to comprehensively analyze the information provided by label-free bright-field photon transmission microscopy (calibrated and validated by AFM [22]), which detects minute objects of Nobelish resolution [30,32] in a living cell. We do not develop a quantum physical theoretical foundation of

the origin of information in the image. We instead follow the Extended Nijboer–Zernike Theory [15–17], which claims that the focus is at the position of the lowest/highest density of electromagnetic radiation. Provided that two points of the same energy detected by a digital camera chip lie above each other, they are considered to be a light-diffracting or light-emitting object. The extent of the detection as well as of the reliability of the interpretation is heavily limited by the microscope's optical and mechanical properties. The resolution limit is not influenced by the camera sensitivity but by the number of photons. A high number of photons enables objects to be localized (known as discriminability) [28,41]. It is an analogy to super-resolved fluorescence microscopy, where the limit is based on a few photons.

We demonstrate some of the extraordinary properties of an image of elementary light-diffracting, light-emitting, or light-

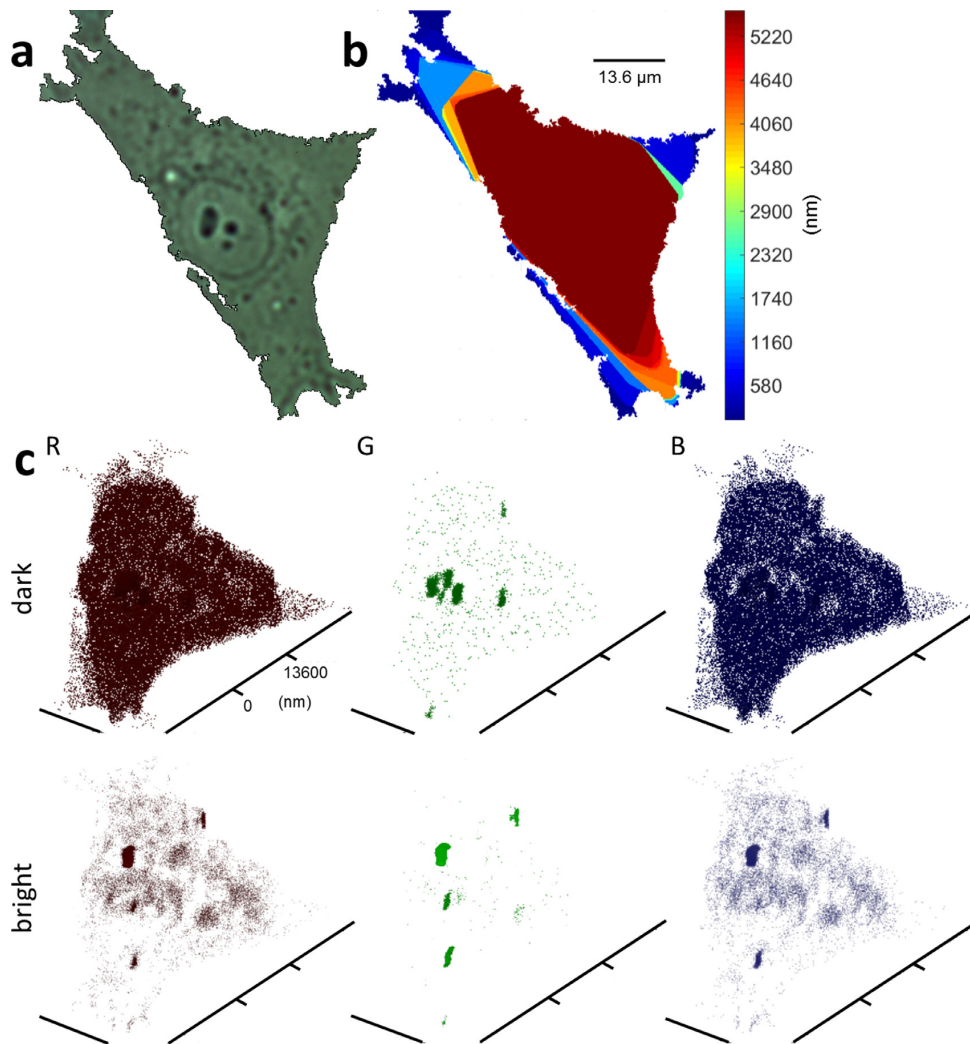


Fig. 3. 3-D reconstruction of a MG63-a cell. (a) An original 2-D image of the segmented MG63-a cell from the center of the focal region (obtained using **Algorithms 1–2** and visualized in 8 bpc). (b) Isocontours of the topological space of the occurrence of the MG63-a cell in its OSF (calculated using **Algorithms 1–3** in Methods). (c) 3-D reconstruction of the large non-moving objects in the MG63-a interior (found using Algorithms 1–4 in Methods). The dark objects (upper row) represent strongly light-diffracting and light-absorbing objects or pixels of destructive light interference (visualization of ranges of intensities 465–884, 1152–2169, and 593–1082 in the R, G, and B channels, respectively). The bright objects (lower row) represent autofluorescent objects or pixels of positive light interference (visualization of ranges of intensities 865–2519, 2137–3445, and 1063–3310 in the R, G, and B channels, respectively).

absorbing objects. Objects of the size of one camera pixel are detected. To re-phrase this observation in the terminology of the depth-of-focus in digital microscopy: the depth of focus is a step along the z-axis within which the information contained in one camera pixel remains within this pixel and is not transferred into the neighbouring pixel. Our results demonstrate that such a definition is very sharp. It means that each point in the image of $\omega_{\alpha,l,x,y,c}$ will be equal to 0. The fact that we have observed only a few points at $\omega_{\alpha,l,x,y,c} = 0$ indicates that objects' spread functions, which give rise to the image in these camera points, have homogeneous intensity over more than one z-level. The latter conclusion indicates that objects detected with $\omega_{\alpha,l,x,y,c} = 0$ at all α values are located within the volume of the voxel. For these objects, the information obtained by our approach is equivalent to a 3-D reconstruction constructed from electron microscopy images. The detection limit of other objects, which gives rise to a certain

distortion in the optical paths, is solely technical. It is due to mechanical precision in the z-step and x-y reproducibility, the size of the camera pixel, the objective magnification, a simple optical path, homogeneous illumination, the scanning frequency, the distribution of camera noise, the bit depth of the camera, and image storage and computational capacity.

4. Methods

Cell cultivation

MG-63 (human osteosarcoma, Serva, cat. No. 86051601) and L929 (mouse fibroblast, Serva, cat. No. 85011425) cell lines were grown at low optical density overnight at 37 °C in a synthetic dropout media with 30% raffinose as the sole carbon source. The nutrient solution for the MG-63 cells consisted of: 86% EMEM, 10% newborn-calf serum, 1% antibiotics and antimycotics, 1% L-glutamine, 1% non-essential amino acids, 1% NaHCO₃ (all compo-

nents were purchased from PAA Laboratories). During microscopy experiments, cells were cultivated in a Biotech FCS2 Closed Chamber System.

Microscopy

Microscopy of a living MG-63 cell culture was performed using a versatile sub-microscope: a nanoscope developed for the Institute of Complex Systems FFPW by the company Optax Ltd. (Czechia). The optical path consisted of two Luminus 360 light emitting diodes, a condenser system, a firm sample holder, and an 40× objective system made of two complementary lenses that allow a change of distance between the objective lens and the sample. The UV and IR light was blocked by a 450 nm long-pass filter and a 775 nm short-pass filter (Edmund Optics), respectively. Next,

a projective lens magnified the image onto a Kodak KAI-16000 camera chip with 4872×3248 resolution and 12-bit colour depth. The size of the original camera pixel using primary magnification was $34 \times 34 \text{ nm}^2$. The z-scan was performed automatically by a programmable piezomechanic (servo) motor. The scanning conditions are presented in [Table 1](#) and [Supplementary data 1](#).

Image processing algorithm

The relevant stacks of micrographs (ca. 2/3 of the original z-stack) were selected from the original z-stacks using the “ILCZ” (MG63-b, L929) tag from the Exif metadata of each image using the file pngparser.exe (in imagesInfo.txt in [Supplementary material](#) available via ftp connection [42]). For the MG63-a cell, the same process was performed using Matlab® scripts: RellmgSelec-

Algorithm 4 2-D segmentation of objects.

INPUT:

rawCell2 as the second RAW file of a cell of interest from two consecutive images;

PDG1C and **PDG2C** as matrices of point divergence gain values calculated for the respective colour channel of two consecutive images, respectively;

m as an intensity mode of the background in the respective colour channel of the second image;

envelope2 as a binary **envelope** of the cell at the second z-level

level as a value of PIED (**level** = 0 for large non-moving objects)

OUTPUT:

dark1 and **bright1** as 2D segments of organelles of different spectral properties

```
Cell2 = demosaicC(rawCell2);
```

```
    % create a quarter-resolved image of the cell in its respective colour
    % channel via non-interpolating algorithm \cite{Tkacik}
```

```
PDG1C0 = PDG1C == level;
```

```
PDG2C0 = PDG2C == level;
```

```
    % in each PDG matrix, threshold values level
```

```
OrgBM = (PDG1C0 + PDG2C0) > 0;
```

```
    % from positive values in the summed binary images with thresholded
    % levels, create a binary mask for the export of objects organelles
```

(continued on next page)

Algorithm 4 (continued)

```

Cell2bright = Cell2;    % duplicate the matrix Cell2

Cell2(Cell2 >= m) = 0;

    % select autofluorescent objects (and positive interferences)

Cell2bright(Cell2bright <= m) = 0;

    % select diffraction and absorption (and negative interferences)

dark1 = (Cell2 .* uint(OrgBM)) .* uint(envelope2);

bright1 = (Cell2bright .* uint(OrgBM)) .* uint(envelope2);

    % apply the binary mask with organelles and that with the topology to
    the debayerized image of the cell

```

tion.m and Shift.m (for image alignment). The average steps and total scanning times are described in [Table 1](#).

The bulk of the image processing and analysis of the bright-field optical micrographs were carried out with Matlab® R2014b software fortified by Image Processing and Statistics Toolboxes (Mathworks, USA) using an OrganelleExtraction script package (ICS FFPW, USB, Czechia). The variables Point Information Gain Entropy Density (Ξ_{α} , PIED) and Point Divergence Gain ($\omega_{\alpha,l,x,y,c}$, PDG) (Eqs. 1 and 3) were computed using Image Info Extractor Professional v.b11 software (ICS FFPW, USB, Czechia; a GBRG Bayer grid) and stored in double precision floating point format in Matlab® structure arrays. The differences in image processing of the cells are shown in [Table 2](#). The basic algorithms for segmentation of cells and intracellular objects are written below. The optimized m-files, software, and original and processed data are available via ftp connection [42].

Author contribution

D.S. conceived of the project, designed the experimental device and tested its performance, R.R. and T.N. analyzed the data and developed the segmentation algorithm based on the first version of algorithm by K.S., P.M. developed entropy-based computing software, J.U. derived the entropy-based variables, R.R. and R.S. scanned the cells and tested the algorithm and device software, T.M. measured standard samples of beads to verify the algorithm, D.M. performed the AFM measurements of live cells, R.R. prepared a manuscript, and all authors discussed and contributed to the final version.

Competing financial interests

The authors declare that they have no competing financial interests.

Correspondence

Correspondence and requests for materials should be addressed to R.R. or D.S. (emails: rrychtarikova@frov.jcu.cz, stys@jcu.cz).

Acknowledgements

This work was financially supported by the Ministry of Education, Youth and Sports of the Czech Republic – projects CENAKVA (No. CZ.1.05/2.1.00/01.0024), CENAKVA II (No. LO1205 under the NPU I program) and The CENAKVA Centre Development (No. CZ.1.05/2.1.00/19.0380) – and by GA JU 017/2016/Z project. Authors thank to Vladimír Kotal and Dalibor Štys Jr. for their contribution to instrument and instrument software testing, and Hana Návarová, Monika Homolková, Šárka Beranová, Pavlína Tláškalová and students of Summer Schools in Nové Hradky (Magdalena Koutová, Marie Hyblová, Adam Charvát, Marco Gómez, Kateryna Akulich, Kaijia Tian, Isabel Mogollon and others) for laboratory work.

Supplementary material

Supplementary material associated with this article can be found, in the online version, at [10.1016/j.jmedia.2015.05.007](https://doi.org/10.1016/j.jmedia.2015.05.007)

Supplementary information

Supplementary information 1. 3-D shapes and heights of MG63 and L929 cells obtained using an atomic force microscope Axio Observer.A1, Zeiss in contact mode.

Supplementary Fig. 1 (a) left – The Extended Nijboer Zernike simulation of fluorescence (parameters $NA = 0.5$, $d = 0.2 \mu\text{m}$, $\lambda = 0.2 \mu\text{m}$, $m = 0$, $n = 0$). right – A real (measured) object spread function of a $0.22 \mu\text{m}$ bead in diffraction with sections of RGB images. The central sections of object spread functions show the positions of focus. (b) A model of phenomena of geometric optics that occur during the interaction of light with an object. The main process is diffraction. In the case of total diffraction of light at the sample interface, it can be considered that the intensities of the sample interior are black and constant, whereas the intensities of light interferences around the sample are brighter and change more in space.

Supplementary Fig. 2. 3-D reconstruction of a MG63-b cell. (a) An original 2-D image of the segmented MG63-b cell from the cen-

ter of the focal region (obtained using **Algorithms 1–2** and visualized in 8 bpc). **(b)** Isocontours of the topological space of the occurrence of the MG63-**b** cell in its OSF (calculated using **Algorithms 1–3** in Methods). **(c)** 3-D reconstruction of the large non-moving objects in the MG63-**b** interior (found using **Algorithms 1–4** in Methods). The dark objects (upper row) represent strongly light-diffracting and light-absorbing objects or pixels of destructive light interference (visualization of ranges of intensities 647–921, 1216–1741, and 747–1030 in the R, G, and B channels, respectively). The bright objects (lower row) represent autofluorescent objects or pixels of positive light interference (visualization of ranges of intensities 910–1475, 1723–2584, and 1026–1495 in the R, G, and B channels, respectively).

Supplementary Fig. 3. 3-D reconstruction of a L929 cell. **(a)** An original 2-D image of the segmented L929 cell from the center of the focal region (obtained using **Algorithms 1–2** and visualized in 8 bpc). **(b)** Isocontours of the topological space of the occurrence of the MG63-**b** cell in its OSF (calculated using **Algorithms 1–3** in Methods). **(c)** 3-D reconstruction of the large non-moving objects in the L929 interior (found using **Algorithms 1–4** in Methods). The dark objects (upper row) represent strongly light-diffracting and light-absorbing objects or pixels of destructive light interference (visualization of ranges of intensities 445–763, 676–1257, and 533–920 in the R, G, and B channels, respectively). The bright objects (lower row) represent autofluorescent objects or pixels of positive light interference (visualization of ranges of intensities 757–1102, 1247–1630, and 908–1212 in the R, G, and B channels, respectively).

Supplementary Fig. 4. Live cell imaging using an atomic force microscope Axio Observer.A1, Zeiss in contact mode. **(a)** 3-D images and heights of a MG63 (similar to presented cells MG63-**b** and L929). **(b)** Average size of MG63 and L929 cells spreading on a mat coated with either fibrinogen or fibronectin. The standard deviations were calculated from 8 cells for the MG63 cell line on both substrates, 6 cells for the L929 cell line on fibrinogen, and 3 cells for the L929 cell line on fibronectin.

Supplementary data 1. Image pre-processing of bright-field transmission z-stacks, including information about the positions of images in the z-stacks. The gray sections correspond to the focal regions. Average values of z-positions and scanning times are reported in **Tables 2** and **3**.

Supplementary video 1. The creation of a binary mask for segmentation of cells over the whole z-stack of 12-bit RAW files from bright-field optical transmission (described in **Algorithm 1**, demonstrated on the MG63-**a** cell). The white points correspond to the zeros in a differential image calculated from the dark green pixels of two consecutive images. With an increasing number of z-levels, white points gradually accumulate in the binary image. The highest amount of these points is achieved in the focal region (z-levels 36–84). After passing the algorithm through the whole z-stack, the binary image underwent the morphological operations of dilation, filling holes, and filtering cells.

Supplementary video 2 The points of unchanged intensity between two consecutive images in the focal region of the z-stack of 12-bit RAW files from bright-field optical transmission of the MG63-**a** cell. The white points were found by overlapping two differential images calculated from the green channels of three consecutive images (instead of $\omega_{\alpha, l, x, y, c} = 0$ in **Algorithm 4**). Without merging levels of similar intensities in histograms of original images due to the Rényi entropy, no organelles were detected. The algorithm only highlighted the cross camera noise (of dark green intensities, cf. **Supplementary video 2**). The course of the video for the MG63-**b** cell was similar.

Supplementary video 3 The points of unchanged intensity between two consecutive images in the focal region of the z-stack of 12-bit RAW files from bright-field optical transmission of the L929

cell. The points were found by overlapping two differential images calculated from the dark green pixels of three consecutive images (instead of $\omega_{\alpha, l, x, y, c} = 0$ in **Algorithm 4**). Since the z-stack of images is noise-free, some organelles were already detected via simple subtraction of consecutive images (cf. **Supplementary video 3**).

The image data, Matlab® codes, and other software are available via ftp connection [42].

References

- [1] S.A. Alexandrov, et al., Novel approach for label free super-resolution imaging in far field, *Sci. Rep.* 5 (2015). Article No. 13274.
- [2] S.S. Vissapragada, Bright-Field Imaging of 3-Dimensional (3-D) Cell-Matrix Structures using New Deconvolution and Segmentation Techniques, Faculty of Drexel University, 2008 Msc. thesis.
- [3] C.N. Hernández Candia, B. Gutiérrez-Medina, Direct imaging of phase objects enables conventional deconvolution in bright field light microscopy, *PLoS ONE* 9 (2014) e89106.
- [4] J. Selinuummi, et al., Bright field microscopy as an alternative to whole cell fluorescence in automated analysis of macrophage images, *PLoS ONE* 4 (2009). Article No. e7497.
- [5] H. Mohamadlou, J.C. Shope, N.S. Flann, Maximizing Kolmogorov complexity for accurate and robust bright field cell segmentation, *BMC Bioinform.* 15 (2014). Article No. 32.
- [6] S.Y. Wu, N. Dugan, B.M. Hennelly, Investigation of autofocus algorithms for brightfield microscopy of unstained cells, in: F. Wyrowski, et al. (Eds.), *Optical Modelling and Design III*, Proc. SPIE 9131, 2014. Article No. 91310T.
- [7] A. Zaritsky, N. Manor, L. Wolf, E. Ben-Jacob, I. Tsarfaty, Benchmark for multi-cellular segmentation of bright field microscopy images, *BMC Bioinform.* 14 (2013). Article No. 319.
- [8] F. Buggenthin, et al., An automatic method for robust and fast cell detection in bright field images from high-throughput microscopy, *BMC Bioinform.* 14 (2013). Article No. 297.
- [9] J.N. Turner, et al., Three-dimensional light microscopy: observation of thick objects, *J. Histotechnol.* 23 (2000) 205–217.
- [10] R. Rychtáriková, et al., Multifractality in imaging: Application of information entropy for observation of inner dynamics inside of an unlabeled living cell in bright-field microscopy, in: Sanayei, et al. (Eds.), *Emergence, complexity and computation*, ICS14, Springer, Switzerland, 2015, pp. 261–267.
- [11] G. Tkacik, et al., Natural images from the birthplace of the human eye, *PLoS ONE* 6 (2011) e20409.
- [12] D. Štys, P. Jizba, S. Papacek, T. Nahlik, P. Cisar, On measurement of internal variables of complex self-organized systems and their relation to multifractal spectra, in: F. Kuipers, P. Heegaard (Eds.), *IWSOS 2012, LCNS*, vol. 7166, Springer, Heidelberg, Berlin, 2012, pp. 36–47.
- [13] A. Rényi, On measures of information and entropy, in: J. Neyman (Ed.), *Proc. 4th Berkeley Symposium on Mathematics, Statistics and Probability 1960*, 1961, pp. 547–561. University of California Press (Berkeley and Los Angeles).
- [14] G. Mie, Beiträge zur optik trüber medien, speziell kolloidaler metallösungen, *Ann. Phys.* 330 (1908) 377–445. Berlin.
- [15] J.J.M. Braat, P. Dirksen, A.J.E.M. Janssen, Assessment of an extended Nijboer-Zernike approach for the computation of optical point-spread functions, *J. Opt. Soc. Am. A* 19 (2002) 858–870.
- [16] F. Zernike, The concept of degree of coherence and its application to optical problems, *Physica* 5 (1938) 785–795.
- [17] B.R.A. Nijboer, *The Diffraction Theory of Aberrations*, University of Groningen, Groningen, The Netherlands, 1942 Ph.d. dissertation.
- [18] G.B. Airy, On the diffraction of an object-glass with circular aperture, *Camb. Phil. Soc. Trans.* 5 (1835) 283–291.
- [19] S. Niehren, Petri Dishes for Cultivation and Microscopy, 2009, Patent No. WO 2009127975 A3.
- [20] Kodak KAI-1600 Image Sensor. Device Performance Specification, 2007, Revision 3.0 MTD/PS-1027, Kodak Image Sensor Solution, Nov 5.
- [21] R. Rychtáriková, et al., Point information gain and multidimensional data analysis, *Entropy* 18 (2016) 372.
- [22] D. Malakhova, D. Štys, R. Rychtáriková, Adjustment of dynamic high resolution images of living cells by combination of an optical microscopy in transmitting light, atomic force microscopy and image information analysis, *Chem. Listy* 107 (2013) s402–s404.
- [23] A. de Melo, A.C. Bet, J. Assreuy, N.A. Debacher, V. Soldi, Adhesion of L929 mouse fibroblast cells on poly(styrene)/poly(methyl methacrylate) films, *J. Braz. Chem. Soc.* 20 (2009) 1753–1757.
- [24] O. Jonas, C. Duschl, Force propagation and force generation in cells, *Cytoskeleton* 67 (2010) 555–563.
- [25] H. Chang, Y. Wang, Cell responses to surface and architecture of tissue engineering scaffolds, in: D. Eberli (Ed.), *Regenerative medicine and tissue engineering – Cells and biomaterials*, 2011. ISBN 978-953-307-663-8.
- [26] D. Docheva, et al., Researching into the cellular shape, volume and elasticity of mesenchymal stem cells, osteoblasts and osteosarcoma cells by atomic force microscopy, *J. Cell. Mol. Med.* 12 (2008) 537–552.
- [27] E. Eckers, M. Deponte, No need for labels: The autofluorescence of *leishmaniantarentolae* mitochondria and the necessity of negative controls, *PLoS ONE* 7 (2012) e47641.

- [28] I.K. Lichtscheidel, I. Foissner, Video microscopy of dynamic plant cell organelles: principles of the technique and practical application, *J. Microsc.* 181 (1996) 117–128. Oxford.
- [29] C. Dobell, Antony van Leeuwenhoek and His "Little Animals": Being Some Account of the Father of Protozoology and Bacteriology and His Multifarious Discoveries in These Disciplines, Harcourt, Brace and Company, New York, 1932, pp. 37–41. [Reprinted 1960 (Dover Publications).]
- [30] E.F. Fornasiero, F. Opazo, Super-resolution imaging for cell biologists: concepts, applications, current challenges and developments, *Bioessays* 37 (2015) 436–451.
- [31] E. Abbe, Beiträge zur theorie des mikroskops und der mikroskopischen wahrnehmung, *Arch. Mikroskop. Anat.* 9 (1874) 469–480.
- [32] W.E. Moerner, Single-molecule spectroscopy, imaging, and photocontrol: foundations for super-resolution microscopy (nobel lecture), *Angew. Chem. Int. Ed.* 54 (2015) 8067–8093.
- [33] F. Zernike, How I discovered phase contrast, *Science* 121 (1955) 345–349.
- [34] D. Murphy, Differential interference contrast (DIC) microscopy and modulation contrast microscopy, in: *Fundamentals of Light Microscopy and Digital Imaging*, Wiley-Liss, New York, 2001, pp. 153–168.
- [35] B. Kemper, P. Langehanenberg, G. von Bally, Digital holographic microscopy: a new method for surface analysis and marker? Free dynamic life cell imaging, *Optik Photonik* 2 (2007) 41–44.
- [36] Y. Kuznetsova, A. Neumann, S.R. Brueck, Imaging interferometric microscopy approaching the linear systems limits of optical resolution, *Opt. Express* 15 (2007) 6651–6663.
- [37] A.M. Zysk, F.T. Nguyen, A.L. Oldenburg, D.L. Marks, S.A. Boppart, Optical coherence tomography: a review of clinical development from bench to bedside, *J. Biomed. Opt.* 12 (2007). Article No. 051403.
- [38] L.F. Kourkoutis, J.M. Plitzko, W. Baumeister, Electron microscopy of biological materials at the nanometer scale, *Annu. Rev. Mater. Res.* 42 (2012) 33–58.
- [39] V.J. Morris, A.R. Kirby, A.P. Gunning, *Atomic Force Microscopy for Biologist*, Imperial College Press, London, 2001.
- [40] P. de Boer, J.P. Hoogenboom, B.N.G. Giepmans, Correlated light and electron microscopy: ultrastructure lights up!, *Nat. Meth.* 12 (2015) 503–513.
- [41] J. Urban, N.K. Afseth, D. Štys, Fundamental definitions and confusions in mass spectrometry about mass assignment, centroiding and resolution, *TrAC-Trend. Anal. Chem.* 53 (2014) 126–136.
- [42] [Ftp://160.217.215.251:21/microscope](ftp://160.217.215.251:21/microscope) (user: anonymous; password: anonymous).

■ **Cell segmentation from telecentric bright-field transmitted light microscopy images using a Residual Attention U-Net: A case study on HeLa line**

A. Ghaznavi, **R. Rychtáriková**, M. Saberioon a D. Štys, *Cell segmentation from telecentric bright-field transmitted light microscopy images using a Residual Attention U-Net: A case study on HeLa line*, *Computers in Biology and Medicine* **147** (2022), 105805.

Jedná se o článek, u něhož jsem spoluautorkou, který dosáhl relativně (vzhledem k mým publikacím) nejvyššího počtu citací v časopise s relativně nejvyšším IF.

Článek popisuje použití metody umělé inteligence k segmentaci savčích neznačených buněk z velkých dat pořízených mikroskopii v procházejícím světle. Na tento článek navazuje podobná publikace o využití umělé inteligence při segmentaci buněk z dat z reflexní světelné mikroskopie

- A. Ghaznavi, **R. Rychtáriková**, P. Císař, Mohammad Mehdi Ziaei a D. Štys, *Symmetry breaking in the U-Net: Hybrid deep-learning multi-class segmentation of HeLa cells in reflected light microscopy images*, *Symmetry* **16** (2024), 227.

Uvedené metody segmentace digitálně-obrazových dat mohou urychlit a zpřesnit výstupy fyzikálně-chemických měření uvnitř živé neznačené buňky.



Cell segmentation from telecentric bright-field transmitted light microscopy images using a Residual Attention U-Net: A case study on HeLa line

Ali Ghaznavi^a, Renata Rychtáriková^{a,*}, Mohammadmehdi Saberioon^b, Dalibor Štys^a

^a Faculty of Fisheries and Protection of Waters, South Bohemian Research Center of Aquaculture and Biodiversity of Hydrocenoses, Institute of Complex Systems, University of South Bohemia in České Budějovice, Zámek 136, 373 33, Nové Hradky, Czech Republic

^b Helmholtz Centre Potsdam GFZ German Research Centre for Geosciences, Section 1.4 Remote Sensing and Geoinformatics, Telegrafenberg, Potsdam 14473, Germany

ARTICLE INFO

Keywords:

Deep learning
Neural network
Cell detection
Microscopy image segmentation
Tissue segmentation
Semantic segmentation
Watershed segmentation

ABSTRACT

Living cell segmentation from bright-field light microscopy images is challenging due to the image complexity and temporal changes in the living cells. Recently developed deep learning (DL)-based methods became popular in medical and microscopy image segmentation tasks due to their success and promising outcomes. The main objective of this paper is to develop a deep learning, U-Net-based method to segment the living cells of the HeLa line in bright-field transmitted light microscopy. To find the most suitable architecture for our datasets, a residual attention U-Net was proposed and compared with an attention and a simple U-Net architecture.

The attention mechanism highlights the remarkable features and suppresses activations in the irrelevant image regions. The residual mechanism overcomes with vanishing gradient problem. The Mean-IoU score for our datasets reaches 0.9505, 0.9524, and 0.9530 for the simple, attention, and residual attention U-Net, respectively. The most accurate semantic segmentation results was achieved in the Mean-IoU and Dice metrics by applying the residual and attention mechanisms together. The watershed method applied to this best – Residual Attention – semantic segmentation result gave the segmentation with the specific information for each cell.

1. Introduction

Image object detection and segmentation can be defined as a procedure to localize a region of interest (ROI) in an image and separate an image foreground from its background using image processing and/or machine learning approaches. Cell detection and segmentation are the primary and critical steps in microscopy image analysis. These processes play an important role in estimating the number of the cells, initializing cell segmentation, tracking, and extracting features necessary for further analysis. In the text below, the segmentation methods were categorized as (1) traditional, feature- and machine learning (ML)-based methods and (2) deep learning (DL)-based methods.

1.1. Traditional cell segmentation methods

Traditional segmentation methods have achieved impressive results in cell boundary detection and segmentation, with an efficient processing time [1,2]. These methods include low-level pixel processing approaches. The region-based methods are more robust than the

threshold-based segmentation methods [2]. However, in low-contrast images, cells placed close together or flat cell regions can be segmented as blobs. Rojas-Moraleda et al. [1] proposed a region-based method on the principles of persistent homology with an overall accuracy of 94.5%. The iterative morphological and Ultimate Erosion [3,4] suffer from poor segment performance when facing small and low-contrast objects. Guan et al. [5] detected rough circular cell boundaries using the Hough transform and the exact cell boundaries using fuzzy curve tracing. Compared with the watershed-based method [6], this method was more robust to the noise and the uneven brightness in the cells. Winter et al. [7] combined the image Euclidean distance transformation with the Gaussian mixture model to detect elliptical cells. This method requires solid objects for computing the distance transform. The target objects' large holes or extreme internal irregularities make the distance transform unreliable and reduce the method performance. Buggenthin et al. [8] identified nearly all cell bodies and segmented multiple cells instantly in bright-field time-lapse microscopy images by a fast, automatic method combining the Maximally Stable Extremal

* Corresponding author.

E-mail addresses: ghaznavi@frov.jcu.cz (A. Ghaznavi), rrychtarikova@frov.jcu.cz (R. Rychtáriková), saberioon@gfz-potsdam.de (M. Saberioon), stys@frov.jcu.cz (D. Štys).

<https://doi.org/10.1016/j.complbiomed.2022.105805>

Received 17 March 2022; Received in revised form 3 June 2022; Accepted 26 June 2022

Available online 28 June 2022

0010-4825/© 2022 Elsevier Ltd. All rights reserved.

Regions (MSER) with the watershed method. The main challenges for this method remain the oversegmentation and poor performance for out-of-focus images.

The machine learning methods have expanded due to the microscopy images' complexity and the previous methods' low performance to detect and segment cells. The ML methods can be classified into two groups: supervised vs unsupervised. The supervised methods produce a mathematical function or model from the training data to map a new data sample [9]. Mualla et al. [10] utilized the Scale Invariant Feature Transform (SIFT) as a feature extractor and the Balanced Random Forest as a classifier to calculate the descriptive cell keypoints. The SIFT descriptors were invariant to illumination conditions, cell size, and orientation. Tikkanen et al. [11] developed a method based on the Histogram of Oriented Gradients (HOG) and the Support Vector Machine (SVM) to extract feature descriptors and classify them as a cell or a non-cell in bright-field microscopy data. The proposed method is susceptible to the number of iterations in the training process as a crucial step to eliminating false positive detections.

The unsupervised ML algorithms require no pre-assigned labels or scores for the training data [12]. The best known unsupervised methods are clustering methods. Mualla et al. [13] segmented unstained cells in bright-field micrographs using a combination of a SIFT to extract key points, a self-labelling, and two clustering methods. This method is fast and accurate but sensitive to the feature selection step to avoid overfitting.

1.2. Deep learning cell segmentation methods

In the last decade, Deep Learning has emerged as a new area of machine learning. The DL methods contain a class of ML techniques that exploit many layers of non-linear information processing for supervised or unsupervised feature extraction and transformation for pattern analysis and classification. The Deep Convolutional Networks exhibited impressive performance in many visual recognition tasks [14]. Song et al. [15] used a multiscale convolutional network (MSCN) to extract scale-invariant features and graph-partitioning method for accurate segmentation of cervical cytoplasm and nuclei. This method significantly improved the Dice metric and standard deviation compared with similar methods. Shibuya et al. [16] proposed the Feedback U-Net using the convolutional Long Short-Term Memory (LSTM) network for cell image segmentation, working on four classes of *Drosophila* cell image dataset. However, the proposed method suffered from a low accuracy rate depending on the segmented class. Thi et al. [17] proposed a convolutional blur attention (CBA) network. The network consists of down- and upsampling procedures for nuclei segmentation in standard challenge datasets [18,19]. The authors achieved a good value of the aggregated Jaccard index. The reduced number of trainable parameters led to a reasonable decrease in the computational cost. Xing et al. [20] also proposed an automated nucleus segmentation method based on a deep convolutional neural network (DCNN) to generate a probability map. However, the proposed mitosis counting remains laborious and subjective to the observer.

One of the most popular models for semantic segmentation is Fully Convolutional Network (FCN) architectures. The FCN combines deep semantic information with a shallow appearance to achieve satisfactory segmentation results. The convolutional networks can take the arbitrary size of input images to train end-to-end, pixel-to-pixel, and produce an output of the corresponding size with efficient inference and learning to achieve semantic segmentation in complex images, including microscopy and medical images [21,22]. Ronneberger et al. [23] proposed a training strategy that relies on the strong use of data augmentation by applying U-Net Neural Network, contracting the path to capture context, and expanding the path symmetrically to achieve a precise localization. This method was optimized with a low amount of training labelled samples and efficiently performed electron microscopy image segmentation. Long et al. [24] proposed an enhanced U-Net-based

architecture called light-weighted U-Net (U-Net+) with a modified encoded branch for potential low-resources computing of nuclei segmentation in bright-field, dark-field, and fluorescence microscopy images. However, the proposed method did not achieve higher accuracy in the Mean-IoU metric. Bagyaraj et al. [25] proposed two automatic deep learning networks called U-Net-based deep convolution network and U-Net with a dense convolutional network (DenseNet) for segmentation and detection of brain tumour cells. The authors achieved remarkable results by applying the DenseNet architecture.

As described above, traditional ML methods are not much efficient to segment cells in a microscopy image with a complex background, particularly bright-field microscopy tiny cells [8,11,13]. These methods cannot build sufficient models for big datasets. On the other hand, some Convolution Neural Networks (CNNs) require a vast number of manually labelled training datasets and higher computational costs compared with the ML methods [21,26].

Deep learning-based methods have delivered better outcomes in segmentation tasks than other methods. Therefore, the main objective of this research is to propose a highly accurate and reasonably computationally cost deep learning-based method to segment human HeLa cells in unique telecentric bright-field transmitted light microscopy images. The U-Net was chosen since it is one of the most promising methods used in semantic segmentation [23]. Different U-Net architectures such as Attention and Residual Attention U-Net were examined to find the most suitable architecture for our datasets.

Human Negroid cervical epithelioid carcinoma line HeLa [27] was chosen as a testing cell line for described microscopy image segmentation. The reason for choosing is that HeLa is the oldest, immortal, and most used model cell line ever. HeLa is cultivated in almost all tissue and cell laboratories worldwide and utilized in many fields of medical research, such as research on carcinoma or testing the material biocompatibility.

The processed microscopy data are specific to high-pixel resolution in rgb mode and requires preprocessing to suppress optical vignetting and camera noise. The data shows unlabelled living cells in their physiological state. The cells are shown in-focused and out-of-focus. Thus, the obtained segmentation method is applicable in a 3D visualization of the cell.

2. Materials and methods

2.1. Cell preparation and microscope specification

Human HeLa cell line (European Collection of Cell Cultures, Cat. No. 93021013) was cultivated to low optical density overnight at 37 °C, 5% CO₂, and 90% relative humidity. The nutrient solution consisted of Dulbecco's modified Eagle medium (87.7%) with high glucose (>1 g L⁻¹), fetal bovine serum (10%), antibiotics and antimycotics (1%), L-glutamine (1%), and gentamicin (0.3%; all purchased from Biowest, Nuaille, France). The HeLa cells were maintained in a Petri dish with a cover glass bottom and lid at room temperature of 37 °C.

Time-lapse image series of living human HeLa cells on the glass Petri dish were captured using a high-resolved bright-field light microscope for observation of microscopic objects and cells. This microscope was designed by the Institute of Complex System (ICS, Nové Hradý, Czech Republic) and built by Optax (Prague, Czech Republic) and Image-Code (Brloh, Czech Republic) in 2021. The microscope has a simple construction of the optical path. The light from two light-emitting diodes CL-41 (Optika Microscopes, Ponteranica, Italy) passes through a sample to reach a telecentric measurement objective TO4.5/43.4-48-F-WN (Vision & Control GmbH, Shul, Germany) and an Arducam AR1820HS 1/2.3-inch 10-bit RGB camera with a chip of 4912 × 3684 pixel resolution. The images were captured as a primary (raw) signal with theoretical pixel size (size of the object projected onto the camera pixel) of 113 nm. The software (developed by the ICS) controls the capture of the primary signal with the camera exposure of 2.75 ms. All these experiments were performed in time-lapse to observe cells' behaviour over time.

2.2. Data acquisition

Different time-lapse experiments on the HeLa cells were completed under the bright-field microscope (Section 2.1). The algorithm proposed in [28] was fully automated and implemented in the microscope control software to calibrate the microscope optical path and correct all image series to avoid image background inhomogeneities and noise.

After the image calibration, we converted the raw image representations to 8-bit colour (rgb) images of resolution (number of pixels) quarter of the original raw images. We employed quadruplets of Bayer mask pixels [29]: Red and blue camera filter pixels were adopted into the relevant image channel and each pair of green camera filter pixels' intensities were averaged to create the green image channel. Then, images were rescaled to 8-bits after creating the image series intensity histogram and omitting unoccupied intensity levels. This bit reduction ensured the maximal information preservation and mutual comparability of the images through the time-lapse series.

The means denoising method [30] minimized the background noise in the constructed RGB images at preserving the texture details. Afterwards, the image series were cropped to the 1024×1024 pixel size. The steps described above gave us 500 images from different time-lapse experiments. The image dataset is accessible at the Dryad [31].

The cells in the images were labelled manually by MATLAB (MathWorks Inc., Natick, Massachusetts, USA) as Ground-Truth (GT) single class masks with the dimension of 1024×1024 (Fig. 1). The labelled images (512×512 pixels) were used as training (80%), testing (20%), and evaluation (20% of the training set) sets in the proposed U-Net networks.

2.3. U-Net model architectures

The U-Net [23] is a semantic segmentation method proposed on the FCN architecture. The FCN consists of a typical encoder–decoder convolutional network. This architecture includes several feature channels to combine shallow and deep features. The deep features are used for positioning, whereas the shallow features are utilized for precise segmentation. The architecture of the simple U-Net was chosen (Fig. 2) for training the model with the specific size of input images.

The first layer of the encoder part consists of the input layer, which accepts RGB images with the size 512×512 . Each level in the five-“level” U-Net structure includes two 3×3 convolutions. Batch normalization follows each convolution, and “LeakyReLU” activation functions follow a rectified linear unit. In the down-sampling (encoder) part (Fig. 2, left part), each “level” in the encoder consists of a 2×2 max pooling operation with the stride of two. The max-pooling process extracts the maximal value in the 2×2 area. By completing down-sampling in each level of the encoder part, convolutions will double the number of feature channels.

In the up-sampling (decoder) section (Fig. 2, right part), the height and width of the existing feature maps are doubled in each level from bottom to top. Then, the high-resolution deep semantic and shallow features were combined and concatenated with the feature maps from the encoder section. After concatenation, the output feature maps have channels twice the size of the input feature maps. The output decoder layer at the top with a 1×1 convolution size predicts the probabilities of pixels. Padding in the convolution process allowed to achieve the same input and output layers size. The computational result, combined with the Binary Focal Loss function, becomes the energy function of the U-Net.

Between each Encoder–Decoder layer in the simple U-Net (Fig. 2), there is a connection combining the down-sampling path with the up-sampling path to achieve the spatial information. Nevertheless, at the same time, this process brings also many irrelevant feature representations from the initial layers. The self-attention U-Net architecture (Fig. 3-A) with an impressive performance in medical imaging [32] was applied to prevent this problem and improve semantic segmentation

result achieved by standard U-Net. As an extension to the standard U-Net model architecture, the attention gate at the skip connections between encoder and decoder layers highlights the remarkable features and suppresses activations in the irrelevant regions. The advanced function of an attention mechanism is to map a set of key–value pairs and a query to an output. The key, query, values, and outputs are vectors. The compatibility function of the query, together with the corresponding key, is computed to be assigned by weights. Then, weighted sums of the values are computed and generate the output. The weights represent the relative importance of the inputs (the keys) for a particular output (the query) [33]. In this way, the attention gate improves the model sensitivity and performance without requiring complicated heuristics.

The attention gate (Fig. 3-B) has two inputs: x^l and g . Input x^l comes from the skip connection from the encoder layers. Since coming from the early layers, input x^l contains better spatial information. Providing x^l is an output from layer l , a feature activation can be formulated as

$$x_i^l = \sigma_1 \left(\sum_{c' \in F_1} x_{c'}^{l-1} \otimes k_{c',c} \right), \quad (1)$$

by applying a rectified linear unit $\sigma_1(x_{i,c}^l) = \max(0, x_{i,c}^l)$ repeatedly, where i and c correspond to spacial and channel dimensions, respectively, and F_1 denotes the number of feature maps in layer l and \otimes indicates the convolution operation.

Input g – a gating signal – comes from a deeper network layer and contains a better feature representation and contextual information to determining the focus region. Attention coefficients $\alpha \in [0, 1]$ determine, extract, and preserve the valuable features corresponding to the important part of the image regions. The attention part weights different images' parts. This process will add the weights to the pixels based on their relevance in the training steps. The image's relevant parts will get higher weights than the less relevant parts. The output of the attention gate is the multiplication of the input feature maps $x_{i,c}^l$ and the achieved attention coefficient α :

$$p_{att}^l = \psi^T (\sigma_1(W_x^T x_i^l + W_g^T g_i + b_g)) + b_\psi, \quad (2)$$

$$\alpha_i^l = \sigma_2(p_{att}^l(x_i^l, g_i; \Theta_{att})), \quad (3)$$

where parameter σ_2 represents the sigmoid activation function and Θ_{att} contains parameters including linear transformations W_x and W_g , function ψ and bias terms b_ψ and b_g [32]. The achieved weights are also trained in the training process and make the trained model more attentive to the relevant regions.

Another architecture used in this study and developed based on the U-Net models (originally for nuclei segmentation [34]) is the Residual U-Net. The simple U-Net architecture was built based on repetitive Convolutional blocks in each level (Fig. 4-B). Each of these Convolutional blocks consists of the input, two steps of the convolution operation followed by the activation function and the output. On the other hand, we face the vanishing gradient problem when dealing with very deep convolutional networks. The residual step was applied to update the weights in each convolutional block incrementally and continuously (Fig. 4-C) to enhance the U-Net architecture performance by overcoming the vanishing gradient problems.

In the traditional neural networks, each convolutional blocks feed the next blocks. The other problem in a DCNN-based network, such as stacking convolutional layers, is that a deeper structure of these kind of networks will affect generalization ability. To overtake this problem, the skip connections – the residual blocks – improve the network performance, with each layer feeding the next layer and layers about two or three steps apart (Fig. 4-C). The Residual and Attention U-Net architecture were connected to build more effective and high-performance models from our datasets and improve segmentation results.

The watershed algorithm based on morphological reconstruction [35] was applied after completion of the semantic segmentation by

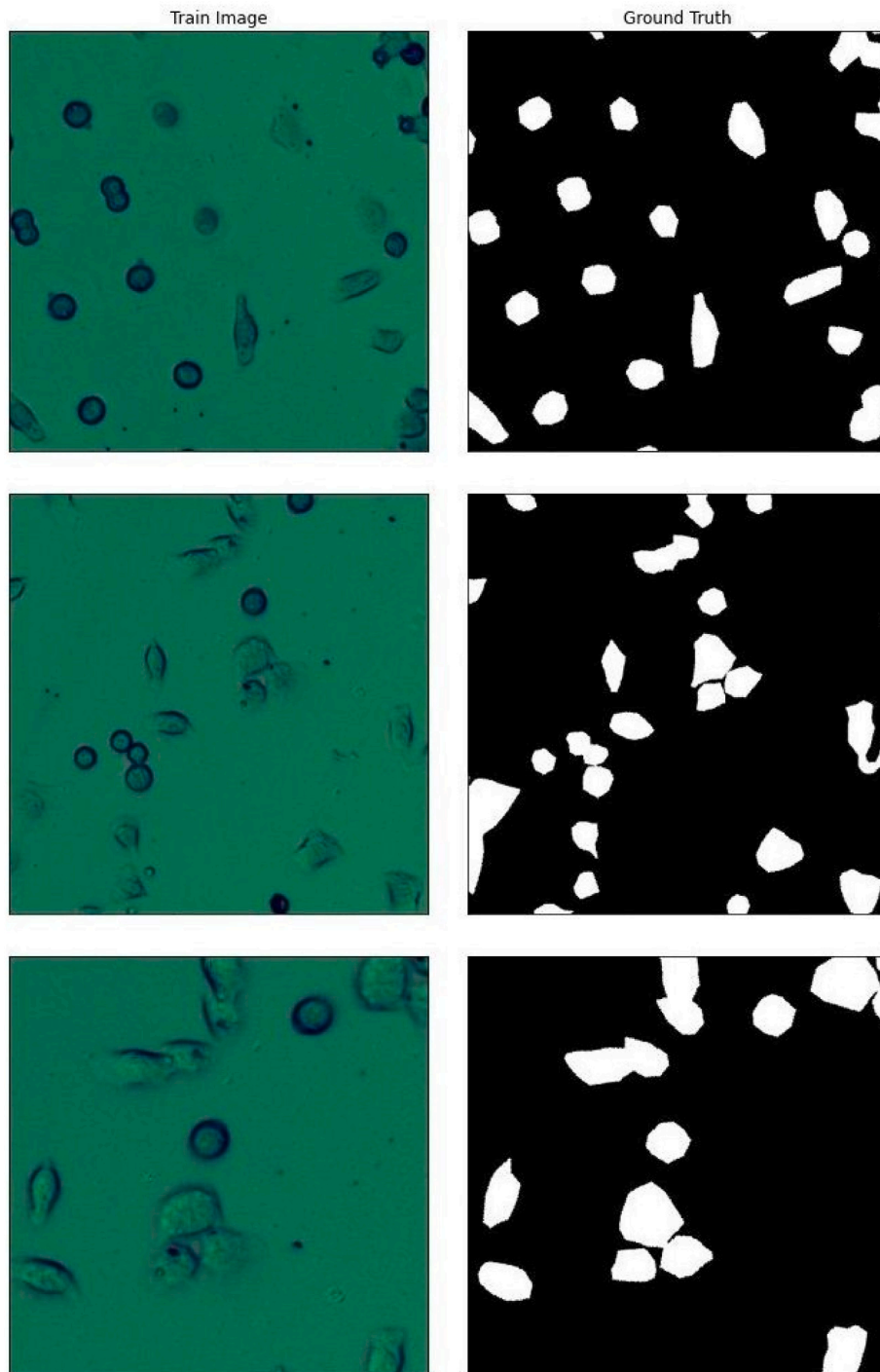


Fig. 1. Examples of the train sets and their ground truths. The image size is 512×512 .

U-Net methods described above. The U-Net semantic segmentation results were first transformed into a binary image using the Otsu method [36]. After that, the background was determined using ten iterations of binary dilation. The simple Euclidean distance transform defined the foreground of eroded cell regions. The unknown region

was achieved by subtraction of the particular foreground region from the background. The watershed method applied to the unknown regions separated the cell borders. The watershed segmentation further helped to solve the over- and under-segmented regions and specify each separated cell by, e.g., cell diameters, solidity, or mean intensity. The

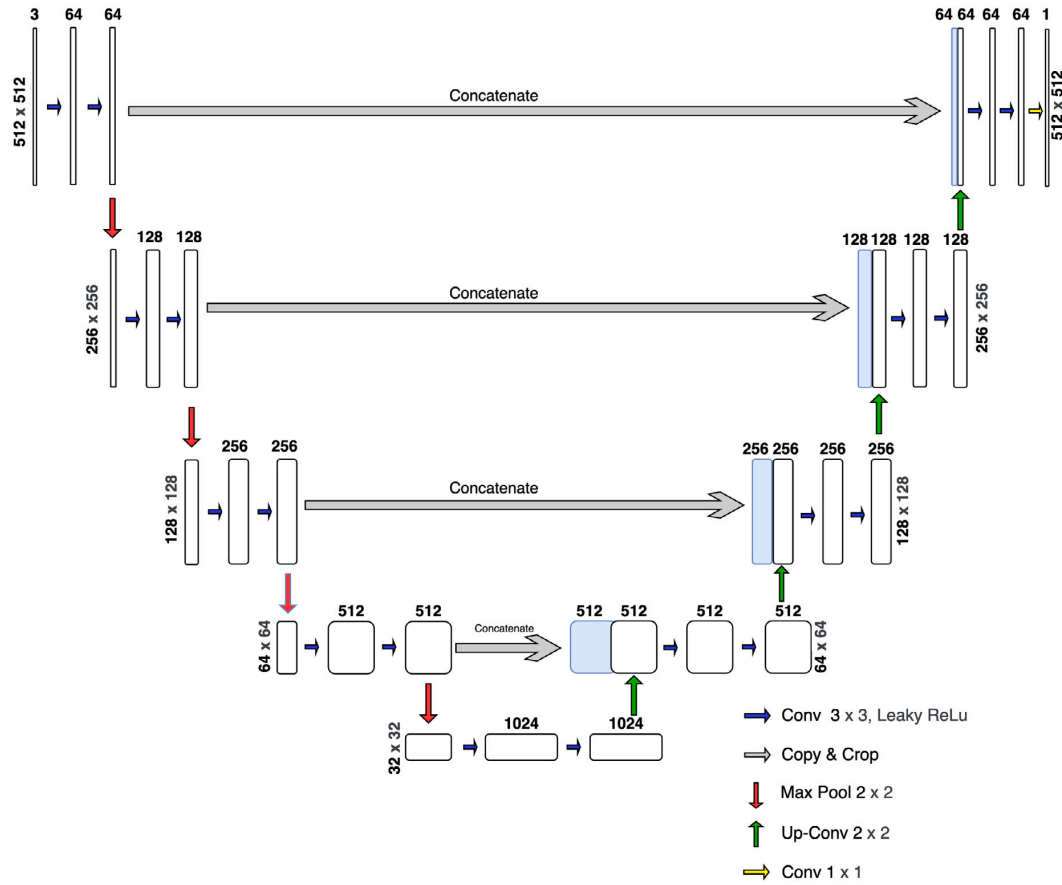


Fig. 2. Architecture of the proposed simple U-Net model.

Table 1
Number of the trainable parameters and the run time for each U-Net model.

Network	Run time	Training parameter
U-Net	3:42:18"	31,402,501
Attention U-Net	4:04:23"	34,334,665
Residual Att U-Net	4:11:24"	39,090,377

segmentation results were optimized using the marked images. Wrongly detected residual connections between different cell regions were cut off, which improved the method accuracy. Fig. 5 presents a general diagram of the proposed U-Net based methods. The U-Net models are hosted on the GitHub [37].

2.4. Training models

The computation was implemented in Python 3.7. The framework for deep learning was Keras, and the backend was Tensorflow [38]. The whole method, including the Deep Learning framework, was transferred and executed on the Google Colab Pro account with P100 and T4 GPU, 24 Gb of RAM, and 2 vCPU [39]. After data preprocessing (Section 2.2), The primary dataset was divided into training (80%) and test (20%). A part (20%) of the training set was used for model validation in the training process to avoid over-fitting and achieve higher performance. Among a 500-image dataset of the mixture of under-, over-, and focused images, 320 images were randomly selected to train the model, and 80 images were chosen randomly to validate the

process. The rest of the 100 dataset images were considered for testing and evaluating the model after training.

Before the training, the images were normalized: the pixel values were rescaled in the range from 0 to 1. Since all designed network architectures work with a specific input image size, all datasets were resized to 512 × 512 pixel size. Data augmentation parameters were also applied in training all three U-Net architectures. The optimized values of the hyperparameters used in the training process are written in Table 2. The “rotation range” represents an angle of the random rotation, “width shift range” represents an amplitude of the random horizontal offset, “height shift range” corresponds to an amplitude of the random vertical offset, “shear range” is a degree of the random shear transformation, “zoom range” represents a magnitude of the random scaling of the image. Early stopping hyperparameters were applied to avoid over-fitting during the model training. The patient value was considered as 15. The activation function was set to the LeakyRelu, and the Batch size was set to 8. To optimize the network, we chose the Adam optimizer and set the learning rate to 10⁻³.

Semantic image segmentation can be considered as a pixel classification as either the cell or background class. The Dice loss was used to compare the segmented cell image with the GT and minimize the difference between them as much as possible in the training process. One of the famous loss functions used for semantic segmentation is the Binary Focal Loss (Eq. (4)) [40]:

$$\text{Focal Loss} = -\alpha_r(1 - p_r)^{\gamma} \log(p_r), \tag{4}$$

where $p_r \in [0, 1]$ is the model’s estimated probability for the GT class with label $y = 1$; a weighting factor $\alpha_r \in [0, 1]$ for class 1 and $1 - \alpha_r$ for

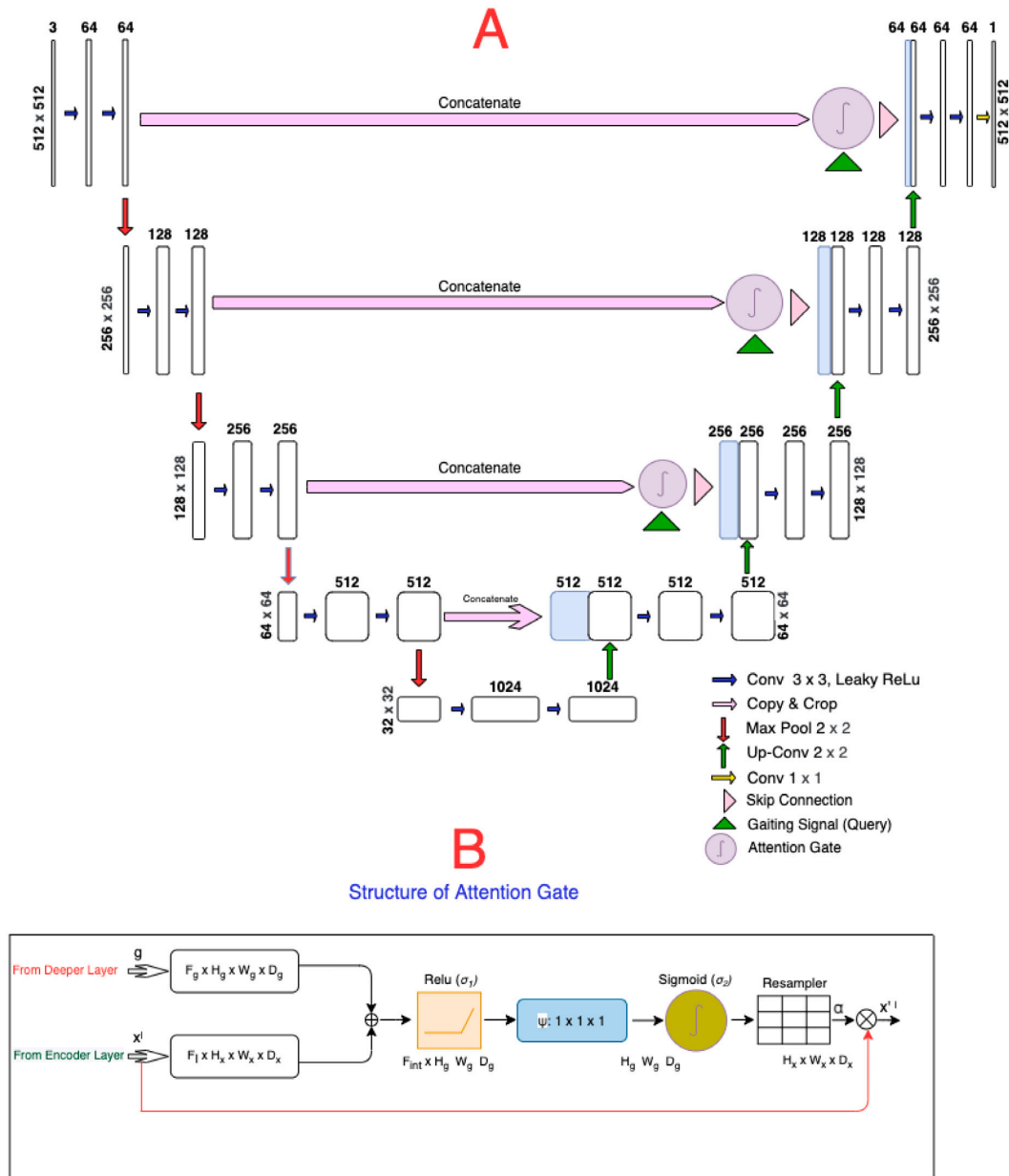


Fig. 3. (A) Architecture of the proposed Attention U-Net model, (B) the attentive module mechanism. The size of each feature map is shown in $H \times W \times D$, where H , W , and D indicate height, width, and number of channels, respectively.

class -1 ; $\gamma \geq 0$ is a tunable focusing parameter. The focal loss can be enhanced by the contribution of hardly segmented regions (e.g., cells with vanished borders) and distinguish parts between the background and the cells with unclear borders. The second benefit of the focal loss is that it controls and limits the contribution of the easily segmented pixel regions (e.g., sharp and apparent cells) in the image at the loss of the model. In the final step, updating the gradient direction is under the control of the model algorithm, dependent on the loss of the model.

2.5. Evaluation metrics

The proposed semantic segmentation models were evaluated by different metrics (Eqs. (5)–(9)), where TP, FP, FN, and TN are true positive, false positive, false negative, and true negative metrics, respectively [41]. The metrics were computed for all test sets and explained as mean values (Table 3).

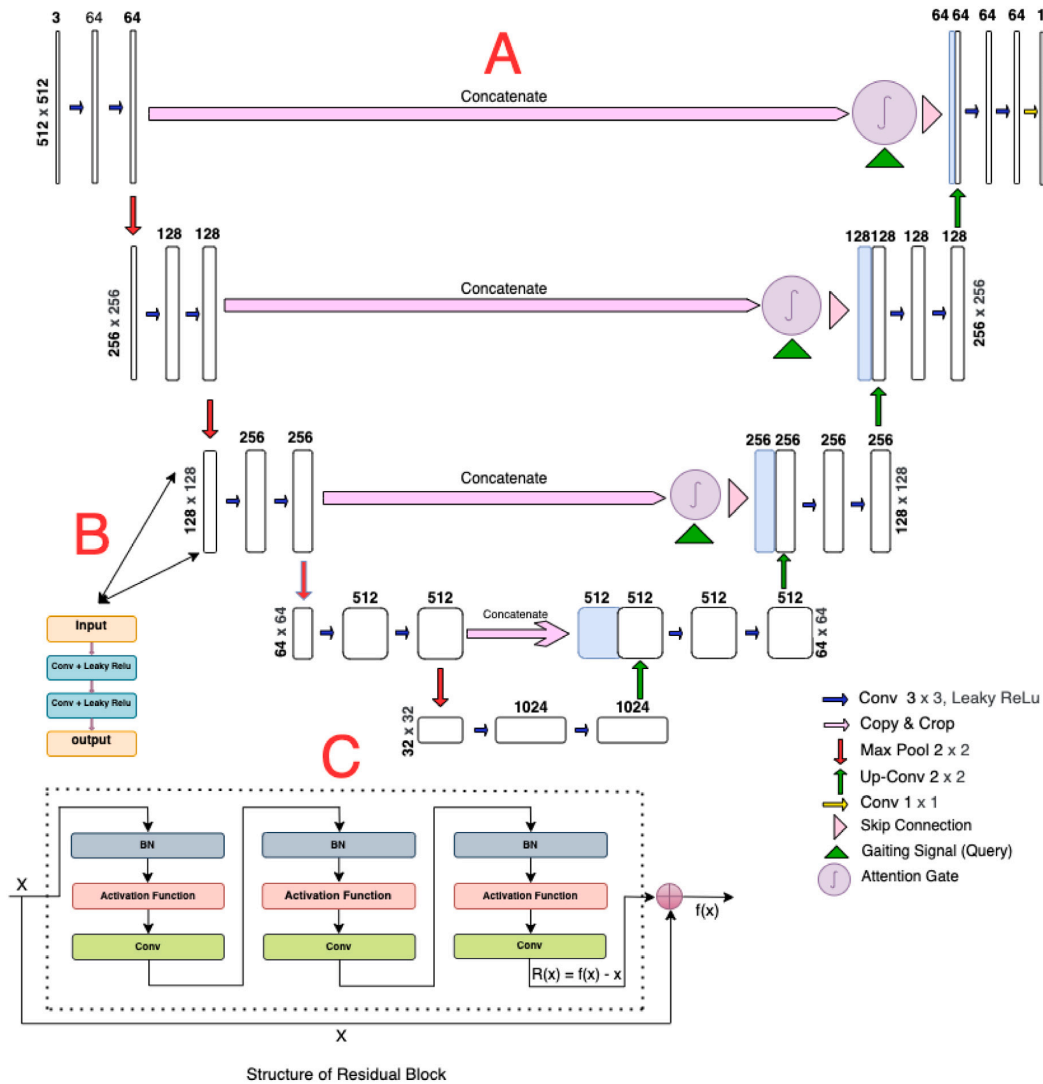


Fig. 4. (A) Architecture of the Residual Attention U-Net model. (B) Each U-Net layer structure. (C) The sample of residual block progress. BN refers to Batch Normalization.

Table 2	
Hyperparameters setting for all three U-Net models.	
Parameter name	Value
Activation function	LeakyRelu
Learning rate	10^{-3}
Batch size	8
Epochs number	100
Early stop	15
Step per epoch	100
Rotation range	90
Width shift range	0.3
Height shift range	0.3
Shear range	0.5
Zoom range	0.3

Overall pixel accuracy (Acc) represents a per cent of image pixels belonging to the correctly segmented cells. Precision (Pre) is a proportion of the cell pixels in the segmentation results that match the GT. The Recall (Recl) represents the proportion of cell pixels in the GT correctly

identified through the segmentation process. The F1-score or Dice similarity coefficient states how the predicted segmented region matches the GT in location and level of details and considers each class's false alarm and missed value. This metric determines the accuracy of the segmentation boundaries [42] and have a higher priority than the Acc. Another essential evaluation metric for semantic image segmentation is the Jaccard similarity index known as Intersection over Union (IoU). This metric is a correlation among the prediction and GT [21,43], and represents the overlap and union area ratio for the predicted and GT segmentation.

$$Acc = \frac{\text{Correctly Predicted Pixels}}{\text{Total Number of Image Pixels}} = \frac{TP + TN}{TP + FP + FN + TN} \quad (5)$$

$$Pre = \frac{\text{Correctly Predicted Cell Pixels}}{\text{Total Number of Predicted Cell Pixels}} = \frac{TP}{TP + FP} \quad (6)$$

$$Recl = \frac{\text{Correctly Predicted Cell Pixels}}{\text{Total Number of Actual Cell Pixels}} = \frac{TP}{TP + FN} \quad (7)$$

$$Dice = \frac{2 \times Pre \times Recl}{Pre + Recl} = \frac{2 \times TP}{2 \times TP + FP + FN} \quad (8)$$

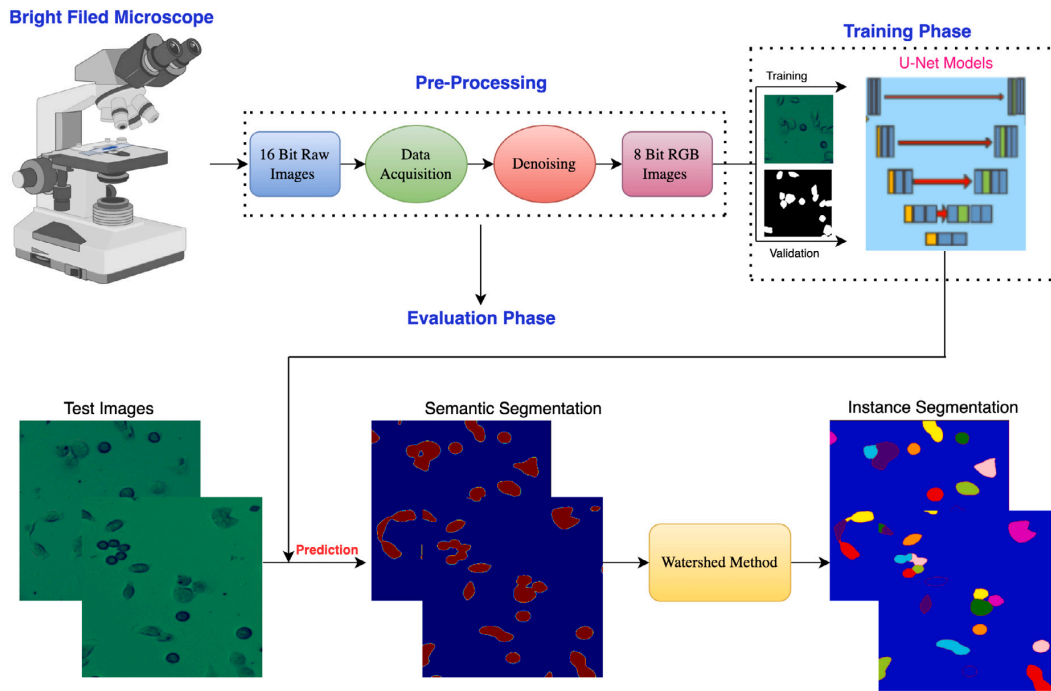


Fig. 5. Flowchart of methodology applied in this study.

$$\text{IoU} = \frac{|y_t \cap y_p|}{|y_t| + |y_p| - |y_t \cap y_p|} = \frac{\text{TP}}{\text{TP} + \text{FP} + \text{FN}} \quad (9)$$

3. Results

All three models were well trained and converged after running 100 epochs based on training/validation loss and Jaccard plots per epochs (Fig. 6). The hyperparameter values listed in Table 2 were selected to tune for the best training performance and stability. Then, the test datasets were used to evaluating the achieved models. All trained models were assessed (Table 3) using the metrics in Eqs. (5) and (9).

Training the model with the simple U-Net method took the shortest run time with the lowest trainable number of parameters (Table 1). Compared with the Attention U-Net and Residual Attention U-Net, the run time difference is not huge in terms of increasing trainable parameters. The computational cost also did not increase dramatically compared with the acceptable improvement in the model performance. Fig. 7 presents the segmentation results achieved by three different U-Net models. The simple U-Net segmentation result did not distinguish some vanished cell borders (Fig. 7-A, black circle). The Attention U-Net (Fig. 7-B) detected cells with the vanish borders more efficiently than the simple U-Net. However, the Attention U-Net segmentation suffers from under-segmentation in some regions (visualized by the yellow circle). The outcome of the Residual Attention U-Net method (Fig. 7-C, red circle) achieved more accurate segmentation of the vanished cell borders. The watershed binary segmentation after the Residual Attention U-Net networks separated and identified the cells with the highest performance (Fig. 7).

As seen in Mean-IoU, Mean-Dice, and Accuracy metrics (Table 3), the Attention U-Net model showed better segmentation performance than the simple U-Net model in the same situation. The segmentation results were further slightly improved after applying the residual step into the Attention U-Net.

4. Discussion

The analysis of bright-field microscopy image sequences is challenging due to living cells' complexity and temporal behaviour. We have to face (1) irregular shapes of the cells, (2) very different sizes of the cells, (3) noise blobs and artefacts, and (4) vast sizes of the time-lapse datasets. Traditional machine learning methods, including random forests and support vector machines, cannot deal with some of these difficulties in terms of higher computational cost and longer run time for huge time-lapse datasets. The traditional methods suffer from low performance in vanishing and tight cell detection and segmentation and are sensitive to training steps [11,44]. The DL methods have been rapidly developed to overcome these problems. The U-Net is one of the most effective semantic segmentation methods for microscopy and biomedical images [23]. This method is based on the FCN architecture and consists of encoder and decoder parts with many convolution layers.

The image data used to train the Residual Attention model are specific in the way of acquisition. Firstly, the optical path was calibrated to obtain the number of photons that reaches each camera pixel with increasing illumination light intensity. This gave a calibration curve (image pixel intensity vs the number of photons reaching the relevant camera pixel) to correct the digital image pixel intensity. This step ensured homogeneity in digital image intensities to improve the quality of cell segmentation by the neural networks. We work with the low-compressed telecentric transmitted light bright-field high-pixel microscopy images. The bright-field light microscope allows us to observe living cells in their most natural state. Due to the object-sided telecentric objective, the final digital raw image of the observed cells is high-resolved and low-distorted, with no light interference halos around objects.

The procedure compressed the raw colour images to ensure the least information loss at the quarter-pixel-resolution decrease of the image. The final pixel resolution of the images inputting into the neural network is higher (512×512) than in the case of any other neural

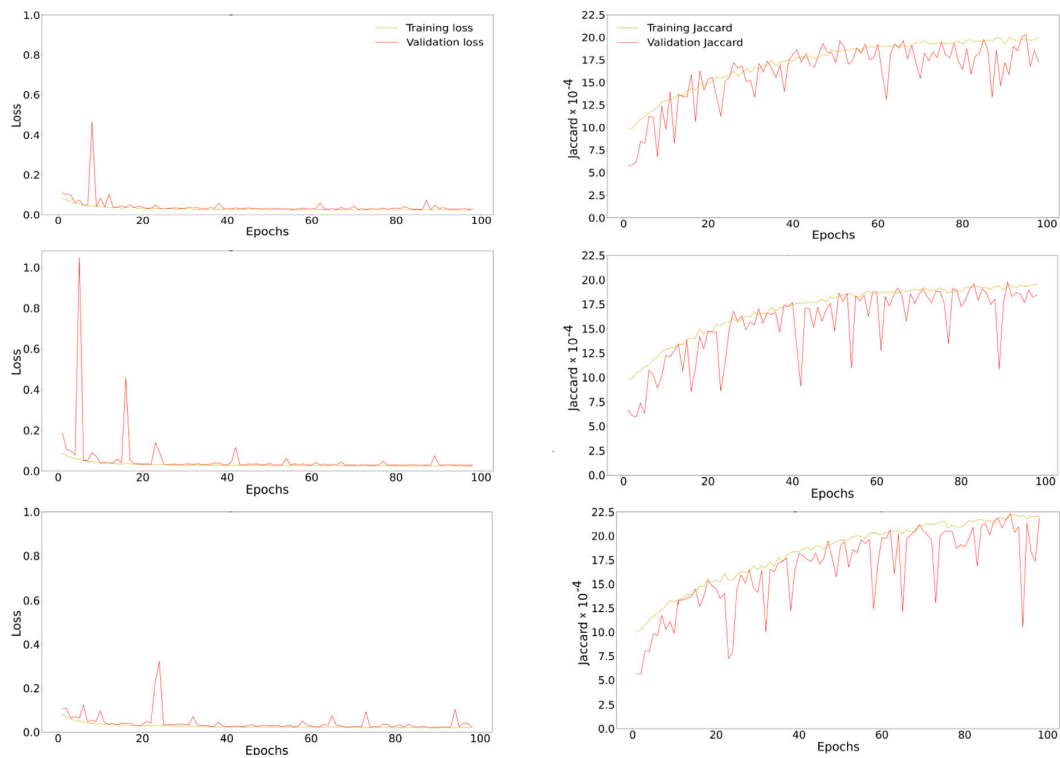


Fig. 6. Training/validation plots for Simple U-Net (left column), Attention U-Net (middle column), and Residual Attention U-Net (right column).

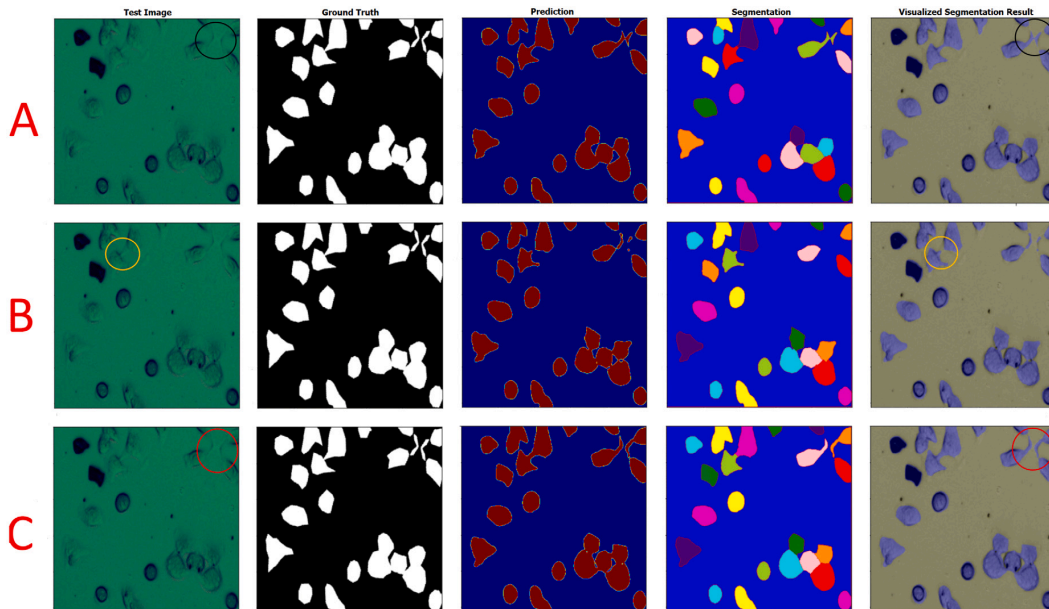


Fig. 7. Segmentation results for (A) the simple U-Net (the black circle highlights the non-segmented, vanished cell borders), (B) Attention U-Net (the yellow circle highlights the undersegmentation problem), and (C) the Residual Attention U-Net (red circle shows the successful segmentation of the cell borders). The image size is 512×512 .

Table 3

Results for metrics evaluating the U-Net Models. Green values represent the highest segmentation accuracy for the related metric.

Network	Accuracy	Precision	Recall	m-IoU	m-Dice
U-Net	0.957418	0.988269	0.961264	0.950501	0.974481
Attention U-Net	0.959448	0.985663	0.965736	0.952471	0.975511
Residual Att U-Net	0.960010	0.986510	0.965574	0.953085	0.975840

Table 4

Performances of the proposed networks and other networks proposed for microscopy and medical applications. Green highlighted value represent the highest segmentation accuracy in term of mentioned metric.

Models	IoU	Dice	Acc
proposed U-Net	0.9505	0.9744	0.9574
proposed Att U-Net	0.9524	0.9755	0.9594
proposed ResAtt U-Net	0.9530	0.9758	0.9600
U-Net [23]	0.9203	0.9019	0.9554
U-Net [45]	0.7608	-	0.9235
U-Net+ [24]	0.567	-	-
DenseNet [25]	-	0.911	-
SegNet [45]	0.7540	-	0.9225
Attention U-Net [32]	-	0.840	0.9734
Residual Attention U-Net [46]	-	0.9081	0.9557
Residual U-Net [47]	-	0.8366	-
Residual Attention U-Net [48]	-	0.9655	0.9887

network datasets. By preserving high image resolution as much as possible, the demands on the neural network's computational memory and performance parameters were increased.

As our microscope and acquired microscopy data are unique, and were not used before in similar research, it is hard to compare the results with other works. Despite this, the performances of the proposed U-Net-based models were compared with similar microscopy and medical works (Table 4). Our first model was based on a simple U-Net structure and achieved the Mean-IoU score of 0.9505. We assume that better value of the Mean-IoU will be achieved after the hyperparameter optimization (Table 2). Ronneberger et al. [23] achieved 0.920 and 0.775 Mean-IoU scores for U373 cell line in phase-contrast microscopy and HeLa cell line in Nomarski contrast, respectively. Pan et al. [45] segmented nuclei from medical, pathological MOD datasets with 0.7608 segmentation IoU accuracy score using the U-Net.

We further implemented an attention gate into the U-Net structure (so-called Attention U-Net) to further improve the U-Net model performance by weighing the relevant part of the image pixels containing the target object. In this way, the Mean-IoU metric was improved to 0.9524. The achieved IoU score represents a noticeable improvement in the trained model performance compared with the simple U-Net model. To the best of our knowledge, not many researchers have applied the Attention U-Net to microscopy datasets, but recent papers are prevalently about its application to medical datasets. Microscopy and medical datasets have their complexity and structure, complicating the comparison of the method performances. Applying the Attention U-Net, pancreas [32] and liver tumour [46] medical datasets showed 0.840 and 0.948 Dice metric segmentation accuracy, respectively.

The proposed model performance were improved by one step and obtained the Residual Attention U-Net to overcome the vanishing gradient problem and generalization ability. As a result, the segmentation accuracy was slightly improved by reaching the Mean-IoU of 0.953. The Residual Attention U-Net showed the Dice coefficient of 0.9655 in the testing phase of medical image segmentation [48]. The Recurrent Residual U-Net (R2U-Net) achieved the Dice coefficient of 0.9215 in the testing phase of nuclei segmentation [34]. Patel et al. [47] applied the Residual U-Net to bright-field absorbance image and achieved the Mean-Dice coefficient score of 0.8366. Long et al. [24] applied the enhanced U-Net (U-Net+) to bright-field, dark-field, and fluorescence

microscopy images and achieved the Mean-IoU score of 0.567. The U-Net with a dense convolutional network (DenseNet) was applied to detect and segment brain tumour cells [25] with the Dice score of 0.911 and the Jaccard index of 0.839.

5. Conclusion

Microscopy image analysis via deep learning methods can be a convenient solution due to the complexity and variability of this kind of data. This research aimed to detect and segment living human HeLa cells in images acquired using an original custom-made bright-field transmitted light microscope. Three types of deep learning U-Net architectures were involved in this research: the simple U-Net, Attention U-Net, and Residual Attention U-Net. The simple U-Net (Table 1) has the fastest training time. On the other hand, the Residual Attention U-Net architecture achieved the best segmentation performance (Table 3) with a run time slightly higher than the other two U-Net models.

The Attention U-Net is a method to highlight only the relevant activations during the training process. This method can reduce the computational resource waste on irrelevant activations to generate more efficient models. The best segmentation performance was achieved due to the integration of the residual learning structure (to overcome the gradient vanishing) together with the attention gate mechanism (to integrate a low and high-level feature representation) into the U-Net architecture. After extracting semantic segmentation binary results (Table 3), the watershed segmentation method was applied to separate the cells from each other, avoid over-segmentation, label the cells individually, and extract vital information about the cells (e.g., the total number of the segmented cells, cell equivalent diameter, mean intensity and solidity). Nevertheless, future works are still essential to expand the knowledge on multi-class semantic segmentation with different and efficient CNN's architecture and combine the constructed CNN models in the prediction process to achieve the most accurate segmentation result.

Funding

This work was supported by the Ministry of Education, Youth and Sports of the Czech Republic – project CENAKVA (LM2018099), by the European Regional Development Fund in frame of the project ImageHeadstart (ATCZ215) in the Interreg V-A Austria–Czech Republic programme, and by the project GAJU, Czech Republic 017/2016/Z.

Declaration of competing interest

The authors declare that they have no known competing financial interests or personal relationships that could have appeared to influence the work reported in this paper.

Data and code availability

The U-Net models are hosted on the GitHub [37] and other data on the Dryad [31].

Acknowledgements

The authors would like to thanks our lab colleagues Šárka Beranová and Pavlína Tláskalová (both from the ICS USB) and Mohammad Mehdi Ziaei for their support of this study.

References

- [1] R. Rojas-Moraleda, W. Xiong, N. Halama, K. Breitkopf-Heinlein, S. Dooley, L. Salinas, D.W. Heermann, N.A. Valous, Robust detection and segmentation of cell nuclei in biomedical images based on a computational topology framework, *Med. Image Anal.* 38 (2017) 90–103, <http://dx.doi.org/10.1016/j.media.2017.02.009>.
- [2] J.R. Tang, N.A. Mat Isa, E.S. Ch'ng, A fuzzy-c-means-clustering approach: Quantifying chromatin pattern of non-neoplastic cervical squamous cells, *PLoS One* 10 (11) (2015) e0142830, <http://dx.doi.org/10.1371/journal.pone.0142830>.
- [3] Z. Wang, A semi-automatic method for robust and efficient identification of neighboring muscle cells, *Pattern Recognit.* 53 (2016) 300–312, <http://dx.doi.org/10.1016/j.patcog.2015.12.009>.
- [4] G. Fan, J.-W. Zhang, Y. Wu, D.-F. Gao, Adaptive marker-based watershed segmentation approach for T cell fluorescence images, in: 2013 International Conference on Machine Learning and Cybernetics, Vol. 02, 2013, pp. 877–883, <http://dx.doi.org/10.1109/ICMLC.2013.6890407>.
- [5] P.P. Guan, H. Yan, Blood cell image segmentation based on the hough transform and fuzzy curve tracing, in: 2011 International Conference on Machine Learning and Cybernetics, Vol. 4, 2011, pp. 1696–1701, <http://dx.doi.org/10.1109/ICMLC.2011.6016961>.
- [6] X. Zhou, F. Li, J. Yan, S.T. Wong, Novel cell segmentation method and cell phase identification using Markov model, *IEEE Trans. Inf. Technol. Biomed.* 13 (2) (2009) 152–157, <http://dx.doi.org/10.1109/ITTB.2008.2007098>.
- [7] M. Winter, W. Mankowski, E. Wait, E.C.D.L. Hoz, A. Aguinaldo, A.R. Cohen, Separating touching cells using pixel replicated elliptical shape models, *IEEE Trans. Med. Imaging* 38 (4) (2019) 883–893, <http://dx.doi.org/10.1109/TMI.2018.2874104>.
- [8] F. Buggenthin, C. Marr, M. Schwarzfischer, P.S. Hoppe, O. Hilsenbeck, T. Schroeder, F.J. Theis, An automatic method for robust and fast cell detection in bright field images from high-throughput microscopy, *BMC Bioinform.* 14 (2013) 297, <http://dx.doi.org/10.1186/1471-2105-14-297>.
- [9] S.J. Russell, *Artificial Intelligence: A Modern Approach*, third ed., Prentice Hall, 2010.
- [10] F. Mualla, S. Schöll, B. Sommerfeldt, A.K. Maier, J. Hornegger, Automatic cell detection in bright-field microscope images using SIFT, random forests, and hierarchical clustering, *IEEE Trans. Med. Imaging* 32 (12) (2013) 2274–2286, <http://dx.doi.org/10.1109/TMI.2013.2280380>.
- [11] T. Tikkanen, P. Ruusuvauro, L. Latonen, H. Huttunen, Training based cell detection from bright-field microscope images, in: 2015 9th International Symposium on Image and Signal Processing and Analysis, ISPA, 2015, pp. 160–164, <http://dx.doi.org/10.1109/ISPA.2015.7306051>.
- [12] G. Hinton, T. Sejnowski, *Unsupervised Learning: Foundations of Neural Computation*, in: MIT Press, MIT Press, 1999.
- [13] F. Mualla, S. Schöll, B. Sommerfeldt, A. Maier, S. Steidl, R. Buchholz, J. Hornegger, Unsupervised unstained cell detection by SIFT keypoint clustering and self-labeling algorithm, in: P. Golland, N. Hata, C. Barillot, J. Hornegger, R. Howe (Eds.), *Medical Image Computing and Computer-Assisted Intervention, MICCAI 2014*, in: Lecture Notes in Computer Science, vol. 8675, Springer International Publishing, Cham, 2014, pp. 377–384, http://dx.doi.org/10.1007/978-3-319-10443-0_48.
- [14] R. Girshick, J. Donahue, T. Darrell, J. Malik, Rich feature hierarchies for accurate object detection and semantic segmentation, in: IEEE Conference on Computer Vision and Pattern Recognition, 2014, pp. 580–587, <http://dx.doi.org/10.1109/CVPR.2014.81>.
- [15] Y. Song, L. Zhang, S. Chen, D. Ni, B. Lei, T. Wang, Accurate segmentation of cervical cytoplasm and nuclei based on multiscale convolutional network and graph partitioning, *IEEE Trans. Biomed.* 62 (10) (2016) 2421–2433, <http://dx.doi.org/10.1109/TBME.2015.2430895>.
- [16] E. Shibuya, K. Hotta, Cell image segmentation by using feedback and convolutional LSTM, *Vis. Comput.* (2021) 11, <http://dx.doi.org/10.1007/s00371-021-02221-3>.
- [17] P. Thi Le, T. Pham, Y.-C. Hsu, J.-C. Wang, Convolutional blur attention network for cell nuclei segmentation, *Sensors* 22 (4) (2022) 1586, <http://dx.doi.org/10.3390/s22041586>.
- [18] N. Kumar, R. Verma, D. Anand, A. Sethi, Multi-Organ Nuclei Segmentation Challenge, Retrieved on 05 May 2021 URL <https://monuseg.grandchallenge.org/>.
- [19] J.C. Caicedo, A. Goodman, K.W. Karhohs, B.A. Cimini, J. Ackerman, M. Haghighi, C. Heng, T. Becker, M. Doan, C. McQuin, M. Rohban, S. Singh, A.E. Carpenter, Broad Bioimage Benchmark Collection, Retrieved on 05 May 2021 URL <https://bbbc.broadinstitute.org/BBBC038>.
- [20] F. Xing, Y. Xie, L. Yang, An automatic learning-based framework for robust nucleus segmentation, *IEEE Trans. Med. Imaging* 35 (2) (2016) 550–566, <http://dx.doi.org/10.1109/TMI.2015.2481436>.
- [21] J. Long, E. Shelhamer, T. Darrell, Fully convolutional networks for semantic segmentation, in: IEEE Conference on Computer Vision and Pattern Recognition, 2015, pp. 3431–3440, <http://dx.doi.org/10.1109/CVPR.2015.7298965>.
- [22] A. Ben-Cohen, I. Diamant, E. Klang, M. Amitai, H. Greenspan, Fully convolutional network for liver segmentation and lesions detection in deep learning and data labeling for medical applications, in: G. Carneiro, D. Mateus, L. c Peter (Eds.), *Deep Learning and Data Labeling for Medical Applications DLMIA 2016, LABELS 2016*, in: Lecture Notes in Computer Science, vol. 10008, Springer, Cham, 2016, pp. 77–85, http://dx.doi.org/10.1007/978-3-319-46976-8_9.
- [23] O. Ronneberger, P. Fischer, T. Brox, U-Net: Convolutional networks for biomedical image segmentation, in: N. Navab, J. Hornegger, W. Wells, A. Frangi (Eds.), *Medical Image Computing and Computer-Assisted Intervention, MICCAI 2015*, in: Lecture Notes in Computer Science, vol. 9321, Springer, Cham, 2015, pp. 234–241, http://dx.doi.org/10.1007/978-3-319-24574-4_28.
- [24] F. Long, Microscopy cell nuclei segmentation with enhanced U-Net, *BMC Bioinform.* 21 (8) (2020) <http://dx.doi.org/10.1186/s12859-019-3332-1>.
- [25] S. Bagyaraj, R. Tamilselvi, P.B.M. Gani, D. Sabarinathan, Brain tumour cell segmentation and detection using deep learning networks, *IET Image Process.* 15 (10) (2021) 2363–2371, <http://dx.doi.org/10.1049/ipr.2.12219>.
- [26] W. Liu, A. Rabinovich, A.C. Berg, Parsenet: Looking wider to see better, in: 4th International Conference on Learning Representations, ICLR 2016, San Juan, Puerto Rico, May 2–4, 2016, Conference Track Proceedings, 2016, p. 11.
- [27] I.N. Lyapun, B.G. Andryukov, M.P. Bynina, Hela cell culture: Immortal heritage of henrietta lacks, *Mol. Genet. Microbiol. Virol.* 34 (4) (2019) 195–200, <http://dx.doi.org/10.3103/S0891416819040050>.
- [28] G. Platonova, D. Štys, P. Souček, K. Lonhuz, J. Valenta, R. Rychtáriková, Spectroscopic approach to correction and visualization of bright-field light transmission microscopy biological data, *Photonics* 8 (8) (2021) 333, <http://dx.doi.org/10.3390/photonics8080333>.
- [29] D. Štys, T. Náhlík, P. Macháček, R. Rychtáriková, M. Saberioon, Least information loss (LIL) conversion of digital images and lessons learned for scientific image inspection, in: F. Ortuno, I. Rojas (Eds.), *Bioinformatics and Biomedical Engineering, IWBIO 2016*, in: Lecture Notes in Computer Science, vol. 9656, Springer, Cham, 2016, pp. 527–536, http://dx.doi.org/10.1007/978-3-319-31744-1_47.
- [30] A. Buades, B. Coll, J.-M. Morel, A non-local algorithm for image denoising, in: 2005 IEEE Computer Society Conference on Computer Vision and Pattern Recognition, Vol. 2, CVPR'05, 2005, pp. 60–65, <http://dx.doi.org/10.1109/CVPR.2005.38>.
- [31] A. Ghaznavi, R. Rychtáriková, M. Saberioon, D. Štys, Telecentric bright-field transmitted light microscopic dataset, 2022, <http://dx.doi.org/10.5061/dryad.80gb5mksp>.
- [32] O. Oktay, J. Schlemper, L.L. Folgoc, M. Lee, M. Heinrich, K. Misawa, K. Mori, S. McDonagh, N.Y. Hammerla, B. Kainz, B. Glocker, D. Rueckert, Attention U-Net: Learning where to look for the pancreas, in: 1st Conference on Medical Imaging with Deep Learning, MIDL 2018, 2018.
- [33] A. Vaswani, N. Shazeer, N. Parmar, J. Uszkoreit, L. Jones, A.N. Gomez, Ł. Kaiser, I. Polosukhin, Attention is all you need, in: I. Guyon, U.V. Luxburg, S. Bengio, H. Wallach, R. Fergus, S. Vishwanathan, R. Garnett (Eds.), *Advances in Neural Information Processing Systems*, Vol. 30, Curran Associates, Inc., 2017, pp. 5998–6008, URL <https://proceedings.neurips.cc/paper/2017/file/3f5ee243547dee91fbd053c1c4a845aa-Paper.pdf>.
- [34] M.Z. Alom, C. Yakopcic, T.M. Taha, V.K. Asari, Nuclei segmentation with recurrent residual convolutional neural networks based U-Net (R2U-Net), in: IEEE National Aerospace and Electronics Conference, NAECON 2018, 2018, pp. 228–233, <http://dx.doi.org/10.1109/NAECON.2018.8556686>.
- [35] W. Zhang, D. Jiang, The marker-based watershed segmentation algorithm of ore image, in: 2011 IEEE 3rd International Conference on Communication Software and Networks, 2011, pp. 472–474, <http://dx.doi.org/10.1109/ICCSN.2011.6014611>.
- [36] N. Otsu, A threshold selection method from gray-level histograms, *IEEE Trans. Syst. Man Cybern.* 9 (1) (1979) 62–66, <http://dx.doi.org/10.1109/TSMC.1979.4310076>.
- [37] A. Ghaznavi, Github repository, 2022, URL <https://github.com/Alighaznavi1986/U-Net-Networks-for-Segmentation>.
- [38] M. Abadi, A. Agarwal, P. Barham, E. Brevdo, Z. Chen, C. Citro, TensorFlow: Large-scale machine learning on heterogeneous distributed systems, in: OSDI'16: Proceedings of the 12th USENIX Conference on Operating Systems Design and Implementation, 2016, pp. 265–283.
- [39] Google, System Spec, Retrieved on 12 December 2021 URL <https://research.google.com/colaboratory/faq.html>.
- [40] T. Lin, P. Goyal, R. Girshick, K. He, P. Dollár, Focal loss for dense object detection, *IEEE Trans. Pattern Anal. Mach. Intell.* 42 (2) (2020) 318–327, <http://dx.doi.org/10.1109/TPAMI.2018.2858826>.
- [41] X. Pan, L. Li, H. Yang, Z. Liu, J. Yang, Y. Fan, Accurate segmentation of nuclei in pathological images via sparse reconstruction and deep convolutional networks, *Neurocomputing* 229 (2017) 88–99, <http://dx.doi.org/10.1016/j.neucom.2016.08.103>.
- [42] G. Scurka, D. Larlus, F. Perronnin, What is a good evaluation measure for semantic segmentation? in: Proceedings of the British Machine Vision Conference, BMVA Press, 2013, pp. 32.1–32.11, <http://dx.doi.org/10.5244/C.27.32>.

- [43] B. Vijay, A. Kendall, R. Cipolla, SegNet: A deep convolutional encoder-decoder architecture for image segmentation, *IEEE Trans. Pattern Anal. Mach. Intell.* 39 (12) (2015) 228–233, <http://dx.doi.org/10.1109/TPAMI.2016.2644615>.
- [44] C. Sommer, C. Straehle, U. Köthe, F.A. Hamprecht, Ilastik: Interactive learning and segmentation toolkit, in: 2011 IEEE International Symposium on Biomedical Imaging: From Nano to Macro, 2011, pp. 230–233, <http://dx.doi.org/10.1109/ISBI.2011.5872394>.
- [45] X. Pan, L. Li, D. Yang, Y. He, Z. Liu, H. Yang, An accurate nuclei segmentation algorithm in pathological image based on deep semantic network, *IEEE Access* 7 (2019) 110674–110686, <http://dx.doi.org/10.1109/ACCESS.2019.2934486>.
- [46] Z. Wang, Y. Zou, P.X. Liu, Hybrid dilation and attention residual U-Net for medical image segmentation, *Comput. Biol. Med.* 134 (2021) 104449, <http://dx.doi.org/10.1016/j.compbiomed.2021.104449>.
- [47] G. Patel, H. Tekchandani, S. Verma, Cellular segmentation of bright-field absorbance images using residual U-Net, in: 2019 International Conference on Advances in Computing, Communication and Control, ICAC3, 2019, pp. 1–5, <http://dx.doi.org/10.1109/ICAC347590.2019.9036737>.
- [48] J. Qiangguo, M. Zhaopeng, S. Changming, C. Hui, S. Ran, RA-UNet: A hybrid deep attention-aware network to extract liver and tumor in CT scans, *Front. Bioeng. Biotechnol.* 8 (2020) 1471, <http://dx.doi.org/10.3389/fbioe.2020.605132>.

10 Anotace tří témat pro veřejnou pedagogickou přednášku

Téma 1: Analýza struktury živé buňky s využitím informační entropie

Nejobecnější možný předpoklad o obrázku, a to bez ohledu na jeho původ, je, že je multifraktální. Za účelem popisu mikroskopického digitálního obrazu jsme vyvinuli principiálně novou informační analýzu, jak zkoumat informaci nesenou obrazovým bodem (pixel) v multifraktálním datovém souboru. Výpočet používá pro danou pravděpodobnostní distribuci P jednoparametrovou, α -závislou, Rényiho entropii. Ta je zobecněnou Shannonovou entropií, která je analogií fyzikální Gibbsovy-Boltzmannovy entropie. Takto jsme odvodili veličiny informační příspěvek bodu (PIG_α) [1, 2], divergentní příspěvek bodu (PDG_α) [3] a z nich odvozené kumulativní veličiny entropií a hustot entropií.

Obrazová analýza digitálních mikroskopických snímků metodou PI/DG nám umožnila pochopit jejich strukturu, nově definovat pojmy „3D elektromagnetický centroid“ a redefinovat pojmy „ohnisková rovina“ a „hloubka ostrosti“. To nám usnadnilo interpretaci jevů pozorovaných světelným mikroskopem. K detekci vysoce strukturované ohniskové roviny v mikroskopických snímcích lze využít klastrování kumulativních veličin. Pro měření v dynamických systémech lze k vyjádření časoprostorové změny využít veličinu divergentní příspěvek bodu (PDG_α) a jeho kumulativní veličinu entropii a hustotu této entropie.

Využití výpočtu informačně-entropických metod pro kolokalizaci ohniskových rovin, trojrozměrnou rekonstrukci a vyhodnocování dynamiky bude představeno na různých datových sériích jednotlivých buněk a tkání pocházejících z fluorescenční, transmisní i reflexní světelné mikroskopie.

Literatura:

1. R. Rychtáriková, J. Korbel, P. Macháček, P. Císař, J. Urban a D. Štys. Point Information Gain and multidimensional data analysis. *Entropy* 18(2), 372, 2016.
2. R. Rychtáriková. Clustering of multi-image sets using Rényi information entropy. In: Ortuño a Rojas (Ed.) International Conference on Bioinformatics and Biomedical Engineering (IWBBIO) 2016, Part I, *Lecture Notes in Computer Science 9656*, Springer, Switzerland (2016), pp. 517–526.
3. R. Rychtáriková, J. Korbel, P. Macháček a D. Štys. Point Divergence Gain and multidimensional data analysis. *Entropy* 20(2), 106, 2018.

■ Téma 2: Analýza struktury živé buňky s využitím kvazispektrální analýzy

Studium buněčné struktury je stěží představitelné bez světelné mikroskopie ve světlém poli. Modernizace této metody, především využití digitální kamery a s tím související možnost videozesílení obrazu, činí tuto metodu ještě přínosnější [1]. To vyvolává otázku, jakou maximální informaci lze z digitálních snímků ve světlém poli získat. Za tímto účelem jsme vyvinuli bezmodelovou, fyzikálně podloženou metodu rekonstrukce (kvazi)spekter pro každý pixel surových obrazových dat z digitální kamery jakéhokoliv (transmisního, reflektančního nebo fluorescenčního) světelného mikroskopu [2]. Tato metoda zahrnuje výstupy radiometrické kalibrace [3] a je založena na předpokladu plynulosti změny světelného spektra v prostoru, dokud není detekována hrana jako náhlá změna barvy. Shlukování spekter bez dalších vnesených předpokladů poskytuje objektivně podloženou sémantiku segmentace nezbarvených živých buněk bez jakýchkoliv apriorních znalostí o jejich strukturách. Jinými slovy, (kvazi)spektrální analýza maximálně vytěžuje veškeré znalosti o experimentu, tedy znalost spektra dopadajícího záření, transmisních spekter barevných filtrů, heterogenity zobrazení optickou drahou stanovenou kalibrací, a nakonec samotnou primární datovou sadu – počet fotonů zachycených senzorem v každém bodě jeho plochy.

Znalost kvazispekter lze využít k/ke (1) interpolaci obrazu v 32rozměrném prostoru, přičemž interpolované hodnoty jsou v technickém smyslu správnější než původní hodnoty počítané pro čtveřici pixelů kamerového senzoru; (2) klastrování oblastí obrazu podle spekter, a nikoliv podle intenzit; (3) vizualizaci, která je obráceným postupem výpočtu (kvazi)spekter a je možné ji provádět pro různé světelné zdroje známých spekter a pro jednotlivé vlnové délky. Lze také (4) vizualizovat jednotlivé spektrálních klastry, a tedy fyzikálně chemické vlastností v daném místě objektu.

Využití metody rekonstrukce (kvazi)spekter bude představeno na digitálních světelně mikroskopických snímcích různých typů buněk a tkání.

Literatura:

1. R. Rychtáriková, T. Náhlík, K. Shi, D. Malakhova, P. Macháček, R. Smaha, J. Urban a D. Štys. Super-resolved 3-D imaging of live cells' organelles from bright-field photon transmission micrographs. *Ultramicroscopy* 179, 1–14, 2017.
2. G. Platonova, D. Štys, P. Souček, K. Lonhus, J. Valenta a R. Rychtáriková. Spectroscopic approach to correction and visualisation of bright-field light transmission microscopy biological data. *Photonics* 8, 333, 2021.
3. K. Lonhus, R. Rychtáriková, G. Platonova a D. Štys. Quasi-spectral characterization of intracellular regions in bright-field light microscopy images. *Scientific Reports* 10, 18346, 2020.

■ Téma 3: Analýza buněčné dynamiky neznačené živé buňky

Kvantitativní analýza jedné buňky je výchozím krokem k pochopení komplexních stochastických procesů buněčné signalizace a stavu a dalšího osudu celé buněčné populace, která je ve své podstatě morfologicky i fyziologicky heterogenní [1]. Měřením vnitrobuněčné dynamiky lze potenciálně studovat například účinky toxických látek na buňky a získané poznatky použít k výběru vhodné buněčné populace jako biosenzoru cytotoxických látek. Pro vyhodnocení vnitrobuněčné dynamiky buňky z primárních snímků světelné mikroskopie v jasném poli jsme navrhli dva fyzikálně podložené způsoby: přímé měření trajektorií organel [2] a měření celkového toku vnitrobuněčné hmoty [3].

Algoritmus [2] je založený na trasování těžiště zobrazení velkých silně světlolomných organel. Organely byly v sérii snímků buňky detekovány jako nulové hodnoty informačního příspěvku bodu (PIG) [4] v zeleném obrazovém kanálu. Takto byla datová série převedena na binární obraz. Trasování organel bylo usnadněno zpracováním vysokofrekvenčních dat, kdy binární zobrazení každé jednotlivé organely v následujícím snímku překrývalo její zobrazení v předchozím snímku série. Trajektorie pohybu každé organely byla přepočítána na rychlost pohybu a její horizontální a vertikální složku. Tyto hodnoty vektorů byly vyjádřeny jak v daném časovém okamžiku, tak jako hodnoty kumulativní, a to pro jednotlivé organely i celou buňku.

Algoritmus [3] je ve srovnání s algoritmem [2] obecnější a komplexněji popisuje vnitrobuněčnou dynamiku. Umožňuje odhadnout mikroreologické a mikrofluidní parametry vnitrobuněčného toku hmoty. Výpočet toků hmoty je zjednodušen přepočtem primárního signálu Bayerovy masky kamery světelného mikroskopu na jednokanálový, šedotónový snímek. Prvním krokem je detekce částic a jejich trasování v sekvenci snímků. Jako nejvhodnější metoda se pro tento účel prokázala metoda SURF (Speeded-Up Robust Features). Pomocí simulace náhodné procházky a výpočtu relativní chyby rychlosti jsou trajektorie částic odděleny na ty vykazující přímý pohyb od těch mající pohyb Brownův náhodný. Z přímého pohybu částic je rekonstruováno rychlostní pole toku hmoty a vypočítána mapa vnitrobuněčné (kvazi)viskozity. Z náhodného pohybu je vyjádřena mapa vnitrobuněčné (kvazi)difuze.

Literatura:

1. D. Bakstad, A. Adamson, D. G. Spiller a M. R. H. White. Quantitative measurement of single cell dynamics. *Current Opinion in Biotechnology* 23(1), 103–109, 2012.
2. R. Rychtáriková a D. Štys. Observation of dynamics inside an unlabeled live cell using a bright-field photon microscopy: Evaluation of organelles' trajectories. In: Ortuño a Rojas (Ed.) International Conference on Bioinformatics and Biomedical Engineering (IWBBIO) 2017, Part II, *Lecture Notes in Computer Science* 10209, Springer, Switzerland (2017), pp. 700–711.

3. K. Lonhus, R. Rychtáriková, A. Ghaznavi a D. Štys. Estimation of rheological parameters for unstained living cells. *The European Physical Journal – Special Topics* 230 1105–1112, 2021.
4. R. Rychtáriková, J. Korbek, P. Macháček, P. Císař, J. Urban a D. Štys. Point Information Gain and multidimensional data analysis. *Entropy* 18(2), 372, 2016.